Improving the Reliability of Tidal Turbine Generator Systems

Wani, F.M.

DOI
10.4233/uuid:b5d38e9a-44ab-4bd4-9cf9-15659f7867b8

Publication date
2021

Document Version
Final published version

Citation (APA)
Wani, F. M. (2021). *Improving the Reliability of Tidal Turbine Generator Systems*. [Dissertation (TU Delft), Delft University of Technology]. https://doi.org/10.4233/uuid:b5d38e9a-44ab-4bd4-9cf9-15659f7867b8

Improving the Reliability of Tidal Turbine Generator Systems

Dissertation

for the purpose of obtaining the degree of doctor
at Delft University of Technology
by the authority of the Rector Magnificus, Prof. dr.ir. T.H.J.J. van der Hagen,
chair of the Board for Doctorates
to be defended publicly on
Thursday 08 April 2021 at 15:00 o'clock

by

Faisal Mushtaq WANI

Master of Science in Electrical Engineering, Delft University of Technology, the Netherlands, and
Master of Science in Wind Energy, Norwegian University of Science and Technology (NTNU),
Norway

This dissertation has been approved by the promotors.

Composition of the doctoral committee:

Rector Magnificus,	chairperson
Dr. ir. H. Polinder	Delft University of Technology, promotor
Dr. J. Dong	Delft University of Technology, copromotor

Independent members:

Prof. dr. J. F. Charpentier	French Naval Academy Research Institute / Ecole Navale, France
Prof. dr. J. A. Ferriera	University of Twente
Prof. dr. S. J. Watson	Delft University of Technology
Prof. dr. R. R. Negenborn	Delft University of Technology
Dr. G. Connor	Nova Innovation Limited, UK

The research leading to this thesis was supported by the TiPA project (Tidal turbine Power take-off Accelerator), which received funding from the European Union's Horizon 2020 research and innovation programme under grant agreement No 727793, managed by the Innovation and Networks Executive Agency. This thesis reflects only the authors' view; the Agency is not responsible for any use that may be made of the information the thesis contains.

Cover design: Q. Q. Contractor

Printed by: Ridderprint | www.ridderprint.nl

ISBN/EAN: 978-94-6366-394-6

هَلْ جَزَآءُ ٱلْإِحْسَٰنِ إِلَّا ٱلْإِحْسَٰنُ

hal jazaaa'ul ihsaani illal ihsaan
Is the reward for good [anything] but good?
—The Quran 55:60

For Maa,
Papaji,
Mehak, Aamir
and my grandfather, M. S. Dar.

Contents

Summary

Last few decades have seen a rapid rise in the development and integration of renewable energy sources in the electrical power grid. Major sources of renewable energy—wind and solar—are intermittent and less predictable. The combination of intermittency and unpredictability results in the increase of balancing costs in the grid. Tidal energy, on the other hand, though not as ubiquitous as solar and wind, is predictable over years. Also, unlike wind and solar, tidal turbines are out of view, which fosters their public acceptance.

Among different ways of harnessing tidal energy, tidal stream turbines are gaining popularity over traditional tidal dams. This is owing to the lower capital cost, and potentially lower ecological impact of tidal turbines. However, compared to more developed sources of energy, tidal energy remains expensive, which impedes its large-scale utilization.

Significant reduction in the cost of energy can be achieved by reducing the maintenance expenses and improving the capacity factor. In other words, improving reliability can make tidal energy substantially cheaper. In this context, this thesis investigates a horizontal axis tidal turbine (HATT) power take-off system with a direct-drive generator.

The focus of this thesis is on improving the reliability of the electrical subsystems in the HATT power take-off system. From this perspective, power converter and generator are the two most important components in the drive train. For the converter, the reliability improvement is analyzed from the objective of delaying the thermal cycling failure in the power semiconductor modules beyond the turbine lifetime. Whereas on the generator side, a flooded generator is investigated as a potentially more reliable alternative to conventional airgap generator. A more detailed summary for each component follows below.

Power converter: thermal cycling in passively cooled converters

Though power converters can fail for a host of reasons, failure from thermal cycling in power modules is a major concern. This is especially true where a power module operates over a wide power range and/or is exposed to significant power swings. Wind turbine power converters, which perform essentially the same function as the tidal turbine converters, were until recently believed to fail mainly from thermal cycling. This could be more true for submerged tidal turbine converters, where converters would be placed in a sealed enclosure, and thus failures from other modes—such as moisture—could be avoided.

An obvious way of delaying thermal cycling induced failure is to provide adequate cooling to the power modules. Typically, this is provided by using forced-water (or other fluid) cooled heat sinks, on which the power module is mounted. The main drawback of this system is the breakdown of active components, such as fan or a cooling pump. A simple solution to this problem is to employ a passively cooled system. In tidal turbines, this means mounting the power modules

on the inside walls of a submerged and sealed cabinet. However, mounting must be done via a thermally conductive material to mitigate the thermal spreading resistance.

Results in this thesis indicate that passively cooled converters can offer adequate cooling to last a normal turbine lifetime (> 25 years). Though passive systems have lower cooling efficiency compared to the forced-water cooling systems, they compensate for it by being more reliable. High reliability is a vital factor in submerged tidal turbine converters. The conclusions regarding the passive cooling are valid for both active speed stall-assisted and pitch-controlled tidal turbines.

An important outcome from investigating the thermal cycling failures was that turbulence in the sea and surface waves can significantly reduce the lifetime of the IGBT power modules. Accounting for ambient turbulence and surface waves results in lowering of the estimated lifetime by more than a factor of 3 than without considering these factors.

Generator: direct-drive flooded generator

A HATT system typically employs an airgap generator, which is housed inside a sealed nacelle. In an airgap generator, the space between the stator and the rotor is filled with air. In HATTs, this is achieved by using a rotary mechanical seal installed on the shaft and the nacelle housing. For sustained and adequate protection of the generator, these seals require periodic maintenance. With increasing depth and the size of turbine, maintaining a watertight environment inside the nacelle becomes more challenging.

A flooded generator has been promoted as a potential solution to this problem. In a flooded generator, the stator-rotor gap is filled with sea water, and the generator design is envisaged keeping this in mind. Consequently, this generator has less stringent sealing requirements, and in principle, could reduce the maintenance costs. Practically speaking, a flooded generator differs from a conventional generator in having a stator and a rotor sleeve (or protective shield/can). First and foremost, presence of stator and rotor sleeves, and the sea water, influences the electrical performance of the generator. Therefore, it becomes imperative to understand and quantify the effect of having stator and rotor sleeves on the generator performance. This knowledge is indispensable in the subsequent step of selecting the materials for the sleeves.

This thesis looks at the sleeve material selection only from the electromagnetic and thermal viewpoints. In practice, sleeve material must also be evaluated on other grounds, such as structural integrity, ease of manufacture, and waterproofing. Results from the thesis demonstrate that while corrosion-resistant metallic materials may be used in rotor sleeves, stator sleeve must be made from electrically non-conductive materials. Otherwise, the generator efficiency will be compromised significantly. Furthermore, compared to an equivalent airgap generator, the presence of water in the stator-rotor gap evens out the temperature distribution inside the flooded generator.

Conclusion

In a nutshell, this thesis encourages using passive cooling for the subsea power electronic converter to improve the reliability. In addition to this, electromagnetic and thermal design aspects of a flooded generator were investigated. This was done because a flooded generator could potentially improve the overall reliability of tidal turbines. However, further research, into other aspects (such as reliability of bearing and seals, fouling in the watergap), is necessary to conclude whether a flooded generator design will actually result in the net improvement of the generator system reliability in tidal turbines.

Samenvatting

De ontwikkeling en integratie van hernieuwbare energiebronnen in het elektriciteitsnet is de afgelopen decennia snel toegenomen. De belangrijkste bronnen van hernieuwbare energie - wind en zon - zijn onderbroken en niet goed voorspelbaar. Onvoorspelbaarheid leidt tot hogere balanceringskosten in het net. Getijdenenergie daarentegen, hoewel niet zo alomtegenwoordig als zon en wind, is voorspelbaar over jaren. Bovendien zijn getijdenturbines, in tegenstelling tot wind- en zonne-energie, buiten het zicht, wat de publieke acceptatie ervan bevordert.

Naast verschillende manieren om getijdenenergie te benutten, winnen getijdenstroomturbines aan populariteit ten opzichte van traditionele getijdendammen. Dit komt door de lagere kapitaalkosten en mogelijk lagere ecologische impact van getijdenturbines. In vergelijking met meer ontwikkelde energiebronnen is getijdenenergie echter nog steeds duur, wat een grootschalig gebruik ervan bemoeilijkt.

Aanzienlijke verlaging van de energiekosten kan worden bereikt door de onderhoudskosten te verlagen en de capaciteitsfactor te verbeteren. Met andere woorden, het verbeteren van de betrouwbaarheid kan getijdenenergie aanzienlijk goedkoper maken. In deze context onderzoekt dit proefschrift het power take-off (PTO) -systeem voor horizontale as-getijdenturbines (HATT) met een direct aangedreven generator.

De belangrijkste focus van dit proefschrift is het verbeteren van de betrouwbaarheid van de elektrische subsystemen in het HATT PTO-systeem. Vanuit dit perspectief zijn vermogenselektonische omzetter en generator de twee belangrijkste componenten in de aandrijflijn. Voor de omzetter wordt de betrouwbaarheidsverbetering geanalyseerd vanuit de doelstelling om falen van de vermogenshalfgeleiders ten gevolge van thermische cycli te vertragen tot na de levensduur van de turbine. Terwijl aan de generatorzijde een met water gevulde generator wordt onderzocht als een potentieel betrouwbaarder alternatief voor de conventionele generator met luchtspleet. Hieronder volgt een meer gedetailleerde samenvatting van elk onderdeel.

Vermogenselektronische omzetter: thermische cycli in passief gekoelde omvormers

Hoewel vermogenselektronische omzetters om tal van redenen kunnen falen, is het falen de halfgeleidercomponenten ten gevolge van thermische cycli een groot probleem. Dit geldt met name wanneer de omzetter over een breed vermogensbereik werkt en / of wordt blootgesteld aan aanzienlijke vermogensschommelingen. Omzetters voor windturbines, die in wezen dezelfde functie vervullen als de omzetters van getijdenturbines, werden tot voor kort verondersteld voornamelijk te falen door thermische cycli. Dit zou meer het geval kunnen zijn voor ondergedompelde getijdenturbine-omzetters, waar omzetters in een afgesloten omhulling zouden worden geplaatst en dus andere faalmechanismen—zoals ten gevolge van vocht—zouden kunnen worden vermeden.

Een voor de hand liggende manier om falen ten gevolge van thermische cycli te vertragen, is door te zorgen voor voldoende koeling van de halfgeleidercomponenten. Meestal wordt hiervoor gezorgd door het gebruik van geforceerd water (of andere vloeistof) gekoelde koellichamen, waarop de halfgeleidercomponenten zijn gemonteerd. Het belangrijkste nadeel van dit systeem is het uitvallen van actieve componenten, zoals een ventilator of een koelpomp. Een eenvoudige oplossing voor dit probleem is om een passief gekoeld systeem te gebruiken. Bij getijdenturbines betekent dit dat de halfgeleidercomponenten aan de binnenwanden van een ondergedompelde en afgesloten kast moeten worden gemonteerd. De montage moet echter gebeuren via een warmtegeleidend materiaal om de thermische spreidingsweerstand te verminderen.

De resultaten in dit proefschrift geven aan dat passief gekoelde converters voldoende koeling kunnen bieden om een normale turbine levensduur (> 25 jaar) te halen. Bij passieve koeling is de thermische weerstand van de behuizing naar de omgeving ruwweg 4 keer zo groot als de overeenkomstige waarde voor geforceerde waterkoeling. Echter, wat passieve systemen missen op het gebied van koelefficiëntie in vergelijking met de geforceerde waterkoeling, maken ze goed door betrouwbaarder te zijn. Hoge betrouwbaarheid is een vitale factor bij omzetters voor getijdenturbines onder water. De conclusies met betrekking tot de passieve koeling zijn geldig zowel voor getijdenturbines met als zonder bladhoekverstelling.

Een belangrijk resultaat van het onderzoek naar de thermische cyclische storingen is dat turbulentie in de zee en oppervlaktegolven de levensduur van de IGBT-vermogensmodules aanzienlijk kan verkorten. Door turbulentie en golven in ogenschouw te nemen, wordt de geschatte levensduur met meer dan een factor 3 verkort vergeleken met het geval waarin deze verwaarloosd worden.

Generator: ondergelopen generator met directe aandrijving

Een HATT-systeem maakt doorgaans gebruik van een generator, die is ondergebracht in een luchtdichte gondel. Bij zo'n generator is de ruimte tussen de stator en de rotor gevuld met lucht. Bij HATT's wordt dit bereikt door een roterende mechanische asafdichting te gebruiken die op de as en de gondelbehuizing is geïnstalleerd. Voor een langdurige en adequate bescherming van de generator hebben deze afdichtingen periodiek onderhoud nodig. Met toenemende diepte en grootte van de turbine, wordt het handhaven van een luchtdichte omgeving in de gondel een grotere uitdaging.

Een met water gevulde generator wordt onderzocht als een mogelijke oplossing voor dit probleem. In zo'n generator wordt de stator-rotorspleet gevuld met zeewater en bij het ontwerp van de generator wordt hiermee rekening gehouden. Dit stelt minder strenge eisen aan de afdichting en zou in principe de onderhoudskosten kunnen verminderen. Praktisch gesproken verschilt zo'n generator van een conventionele generator door een stator- en een rotorhuls. Allereerst beïnvloedt de aanwezigheid van stator- en rotorhulzen en het zeewater de elektrische prestatie van de generator. Daarom wordt het noodzakelijk om het effect van deze stator- en rotorhulzen op de generatorprestaties te begrijpen en te kwantificeren. Deze kennis is onmisbaar bij de volgende stap bij het selecteren van de materialen voor de hulzen.

In dit proefschrift wordt alleen gekeken naar de keuze van het hulsmateriaal vanuit elektromag-

netische en thermische gezichtspunten. In de praktijk moet het hulsmateriaal ook op andere gronden worden beoordeeld, zoals het effect op de constructie, de produceerbaarheid en de waterdichtheid. De resultaten van het proefschrift tonen aan dat hoewel corrosiebestendige metaal kan worden gebruikt in rotorhulzen, de statorhuls gemaakt moet zijn van elektrisch niet-geleidende materialen. Anders zal de efficiëntie van de generator aanzienlijk worden aangetast. Verder wordt opgemerkt dat de aanwezigheid van water in de generator de temperatuurverdeling in de generator egaliseert in vergelijking met een generator met lucht in de luchtspleet.

Conclusie

In een notendop, dit proefschrift moedigt het gebruik van passieve koeling aan voor de onderzeese vermogenselektronica om de betrouwbaarheid te verbeteren. Dit proefschrift onderzoekt ook de met water gevulde generator vanuit de elektromagnetische en thermische ontwerpaspecten. Nader onderzoek naar andere aspecten - zoals betrouwbaarheid van lagers en afdichtingen en vervuiling in de watergap - is echter nodig om te concluderen of een met water gevuld generator-ontwerp zal resulteren in een netto verbetering van de betrouwbaarheid van het generatorsysteem in getijdenturbines.

CHAPTER 1

Introduction

1.1 Introduction

Over the last few decades, renewable sources have become a preferable mode of energy generation over fossil fuels. Major sources of renewable energy—such as solar and wind—are less predictable, and intermittent in nature. This lack of predictability is often cited as a major drawback against renewable energy. Grid operators prefer a predictable energy resource as it facilitates economic and reliable grid operation. Predictable energy sources have higher capacity credit[1] over unpredictable sources [1]. An example of how adding a partially predictable resource, such as waves, can reduce the cost of energy by bringing down the balancing costs in a system with high wind energy penetration can be found in [2].

Tidal energy can be a useful addition to our energy generation mix. Energy from tides is predictable over a span of several years, although there can be non-sinusoidal fluctuations about the mean value over the time scales of minutes and hours [3]. However, by and large, mean values of tidal energy remain predictable. Furthermore, tidal energy is influenced little by weather conditions.

There are two main ways of harnessing tidal energy: tidal barrages (or dams) and tidal stream turbines (TSTs). The estimated global potential for tidal power ranges from 200 to 500 GW [4, 5]. Within this, the exploitable energy potential of the tidal streams is about 75-90 GW [6, 7], with approximately 11 GW being concentrated in Europe [6]. Countries with the major share of tidal stream energy are shown in Figure 1.1 [8]. Tidal resources in Europe are mostly located in the United Kingdom, France, Ireland and Norway. Countries like Belgium, the Netherlands and Italy also have certain suitable sites [9].

Recently tidal stream turbines have become the preferable mode of harvesting tidal energy over tidal dams. Multiple reasons could be responsible for this, e.g. low capital cost and lower impact on local ecosystem compared to tidal dams; confidence gained by the commercial success of

[1] Capacity credit is the amount of conventional generation that could be displaced without making the system any less reliable.

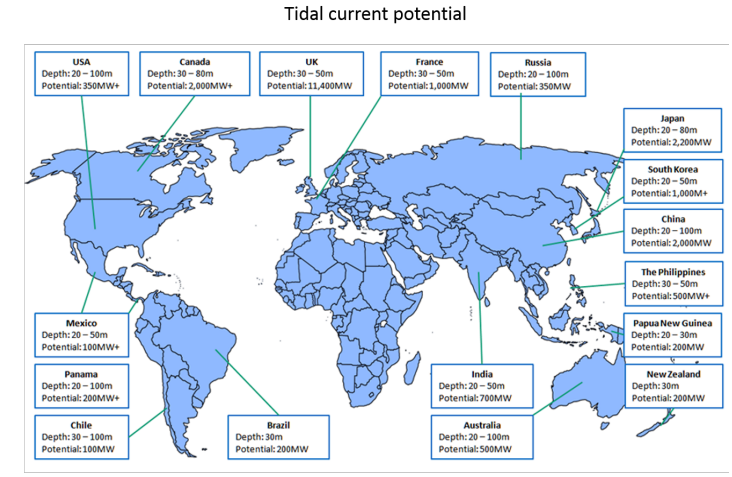

Figure 1.1 Tidal-current-resources worldwide, reproduced from [8].

wind turbines might also have been a contributing factor. Furthermore, the market (economical utilization) for TSTs is expected to be more than the tidal barrage technology [10]. For this reason, this thesis also focuses on TSTs.

A typical tidal stream turbine is shown in Figure 1.2, which is an example of a horizontal axis tidal turbine (HATT). A typical HATT system consists of a turbine, a generator (with or without gearbox), a power electronic converter (placed either onshore or offshore), supporting structures and finally a connection to the grid, as shown in Figure 1.3. A generator converts the mechanical energy from the turbine into electrical energy. Power electronic converters regulate the power capture from the turbine/generator, and convert the generated electricity into a grid compliant form at fixed voltage and frequency.

1.2 Motivation: minimizing the levelized cost of energy

Currently, the levelized cost of energy (LCOE) from TSTs is much higher than the average LCOE from more developed sources of energy [11]. The target set for the tidal energy is about 150 EUR/MWh by the year 2030 [12]. This is an ambitious target considering in 2016 values ranged between 540-710 EUR/MWh [11]. As per the current trends and announced projects, the target is to have around 1 GW installed capacity by 2025 [13]. However, this seems likely only if TSTs driven by innovation result in more reliable devices with higher availability.

In [11], minimizing the operation and maintenance (O&M) expenses, and increasing the capacity

Figure 1.2 Nova M100 tidal turbine [Source: ©Nova Innovation].

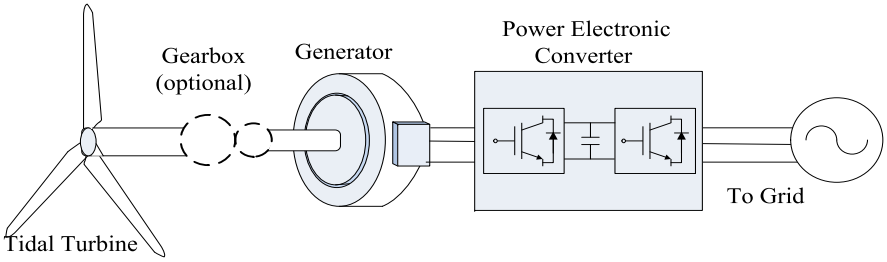

Figure 1.3 A typical HATT drive train. Supporting structure is omitted from this figure, and only the components relevant to power capture are shown.

factor[2] have been identified as important factors in minimizing the LCOE from TSTs. Figure 1.4 shows how much LCOE reduction can be expected by decreasing different cost components. More details on this can be found in Chapter 2.

Increasing the capacity factor and reducing the maintenance expenses are consequences of improving the *reliability* of the system. A major bottleneck in improving the reliability is the lack of credible data which could identify critical components in tidal turbines. Achieving high reliability comes at a cost. Unless these costs are known, we can only speculate that more reliable designs may result in reducing the LCOE. In other words, the *true cost of reliability* or quantifying the correlation between reliability and LCOE remains an arduous task.

[2] Capacity factor is defined as the ratio of the actual electricity production to the maximum possible electricity output over a period of time.

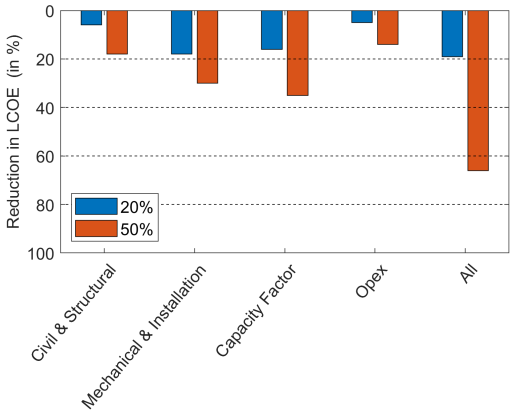

Figure 1.4 Likely reduction in LCOE (in %) for 20% and 50% reduction in the cost of a particular component [Figure is reproduced from [11], and is ambiguous w.r.t. capacity factor. A more clear impact of capacity factor on LCOE is shown in Figure 2.24].

Operating within these limitations, the motivation behind this thesis is to propose the design changes in the state-of-the-art HATT system with the aim of improving the reliability, thereby reducing the LCOE. This thesis aims at achieving this goal by focusing on the reliability of the HATT power take-off system (generator and the power converter).

Power electronic converter is a critical component in the HATT drive train as shown in Figure 1.3. The converter can be placed either onshore, on floating platforms, or they can be seabed-mounted adjacent to the generator. In this thesis we consider the seabed-mounted converter, as this configuration is more suitable for array applications. This configuration minimizes cabling costs [14], involves no hanging cables, and is out of view. However, submerged power converter also means limited access for maintenance, and hence reliability becomes paramount [14]. According to [14], subsea converters for tidal farms will demand a mean time between failures of more than 5 years.

The semiconductor switches (in this case insulated gate bipolar transistor (IGBT) power modules) are perhaps the most important component in the converter. Improving reliability of the power converter, specifically IGBT power modules, is the main problem tackled in this thesis. Although power modules can fail from a variety of reasons, failure from thermal cycling induced stress constitutes one of the main failure modes [15–17], see Figure 1.5. Thermal cycling in the power modules is determined by the loading profile experienced by the converter as well as the system design. This thesis will look into both these aspects of converter reliability in TSTs.

Further reduction of the O&M expenses and improving the capacity factor could be achieved by using a flooded generator rather than a sealed airgap generator [11]. In a flooded generator, the stator-rotor gap is filled with sea water instead of air. As a result, the design of a flooded generator

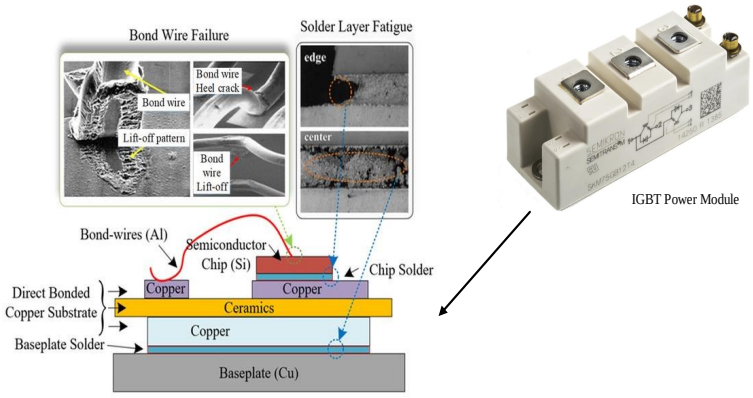

Figure 1.5 Thermal cycling in the power module causes failure mainly from bond-wire lift-off and/or cracks in the solder layer; image adapted from [18].

has to be different from that of an airgap generator. Compared to conventional generator systems, which generally have a technology readiness level (TRL) of around 7-8, direct drive flooded designs have a TRL around 5-6 [19]. However, due to lower criticality of the mechanical seals, flooded designs have a potential of resulting in more reliable systems. Design of flooded generators has not been extensively addressed in literature, and hence this will be the other main exploration in this thesis, in addition to converter reliability.

To summarize, the motivation behind this thesis is to reduce maintenance expenses in HATT power take-off systems by analyzing a submerged power electronic converter and a flooded generator design. A plausible argument could be that reducing the installation and the foundation costs may prove more decisive in reducing the LCOE. This thesis does not refute this argument. However, improvements proposed in this thesis must be seen as supporting measures in this operose task of reducing the LCOE.

1.3 Key definitions

Airgap generator : A generator where the gap between the stator and the rotor is filled with air. In other words, it is a conventional generator.

Flooded generator : A generator where the gap between the stator and the rotor is filled with water, see Figure 1.6.

Passively cooled converter : A converter placed inside a hermetically sealed enclosure, submerged in sea water. The heat generating components inside the converter lose heat via the enclosure walls to the sea. The cooling phenomenon is purely passive and driven by natural convection.

Reliability : Reliability is defined as the probability that the system (or component) performs its specified function for a given time interval under specified operational and environmental conditions [22]. In this thesis, reliability is treated more in qualitative terms: when we say that system A is more reliable than system B, we mean that A is likely to perform its specified function longer than B.

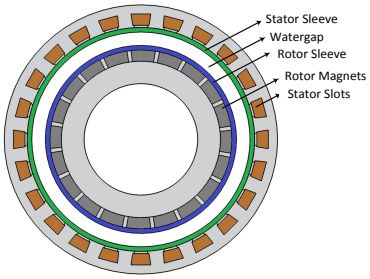

Figure 1.6 A representation of interior view of a flooded generator; inspired from [20, 21]. The figure is not drawn to scale.

1.4 Objectives

1.4.1 Project objective

The main idea behind the research project[3] is to look at various ways to make the HATT power take-off system more reliable so as to minimize the LCOE. The main objective for the research project could thus be put forth as,

'Propose and analyze robust generator and power converter designs to improve the reliability of HATT systems.'

Different topologies exist for the HATT drive train in practice. Unless otherwise specified, the system under consideration in this thesis shall comprise of the following:

- A horizontal axis tidal turbine with fixed-pitch blades and no yawing capabilities;
- A direct-drive permanent magnet generator with surface mounted magnets;
- A hermetically sealed and submerged power electronic converter, which is passively cooled by the ambient sea water.

[3] This research was conducted under the auspices of the TiPA (tidal turbine power take-off accelerator) project. More details about the project can be found on: `https://www.tipa-h2020.eu`.

This system is represented in Figure 1.7. Eliminating the yaw and pitch control will likely improve the overall reliability. However, this may have implications in terms of efficiency, net energy capture, etc. The speed control of the turbine is achieved by active speed stall mechanism[4]. Similarly, using direct-drive generators eliminate losses due to gearbox, and could prove more reliable.

As already mentioned, submerged power converter in the generator vicinity was chosen keeping in mind the array applications in future. Furthermore, we wish to reduce the number of active components in the system; hence, exploring passive cooling system seemed apropos.

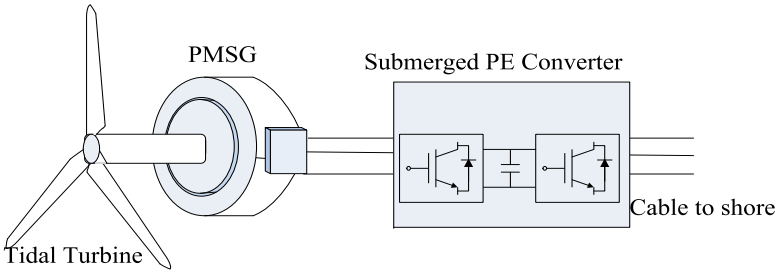

Figure 1.7 Tidal turbine drive train—with a direct-drive permanent magnet synchronous generator (PMSG) and a power electronic (PE) converter—under consideration in this thesis.

1.4.2 Thesis objectives

Passively cooled converter and flooded generator form the two main parts of this thesis. Within the ambit of the research project, the objectives for this thesis are framed as research questions below. The research questions are divided into two categories: for the power converter and the generator.

Power Converter

The extent of thermal cycling, which is a major cause of failure in power converters, depends on the loading conditions as well as the system design. In this context, loading paradigm is defined by the tidal stream velocity profile experienced by the turbine. Turbulence and surface waves can have a significant influence on the tidal stream velocity as seen at the turbine. A natural question then to ask would be:

'How important is the role of turbulence and waves in determining the converter lifetime?'

In terms of system design—turbine, generator and converter specifications—all play a role. In this thesis, we considered an active speed stall-controlled turbine and a passively cooled converter

[4] In active speed stall mechanism, generator torque is increased near and above the rated tidal speed to reduce the turbine speed. This reduces the hydrodynamic efficiency of the turbine at higher tidal speeds limiting the power capture at its rated value. More details will follow in subsequent chapters.

over a pitch-controlled turbine and an actively cooled converter[5]. Consequently, following questions arise:

'How does active speed stall control influence the converter lifetime?'

'Is passive cooling by ambient sea water a feasible option over active cooling in a submerged power converter?'

Generator

Similarly, if a novel flooded generator design is proposed for tidal turbines in lieu of conventional airgap generators, it is pertinent to ask:

'How does the design of flooded generators differ from that of airgap generators?'

Furthermore, given that flooded generator is exposed to sea water, another question arises:

'What materials and winding configurations could be used in flooded generators?'

1.5 Contributions

In the pursuit of answering the aforementioned thesis objectives, following contributions were made in this thesis:

- Developing the thermal models for passively cooled submerged power electronic converter;
- Analyzing the effects of turbulence and sea waves on the converter lifetime in a passively cooled power electronic converter coupled to a TST;
- Comparison of power semiconductor lifetime in submerged power converters for active and passive cooling systems;
- Comparison of power semiconductor lifetime in active speed stall and pitch-controlled turbines;
- Electromagnetic and thermal design of flooded generators, including faster models for rotor eddy current loss calculation; and
- Material selection for stator and rotor sleeves in flooded generators.

1.6 Thesis outline

This thesis comprises of 8 chapters, including this chapter. A brief description of these chapters and the topics they address is given below.

1. **Introduction—** this chapter.

[5] Pitch control and active (usually forced-water) cooling systems are quite common in wind turbines, where lifetime studies on converter have been conducted before.

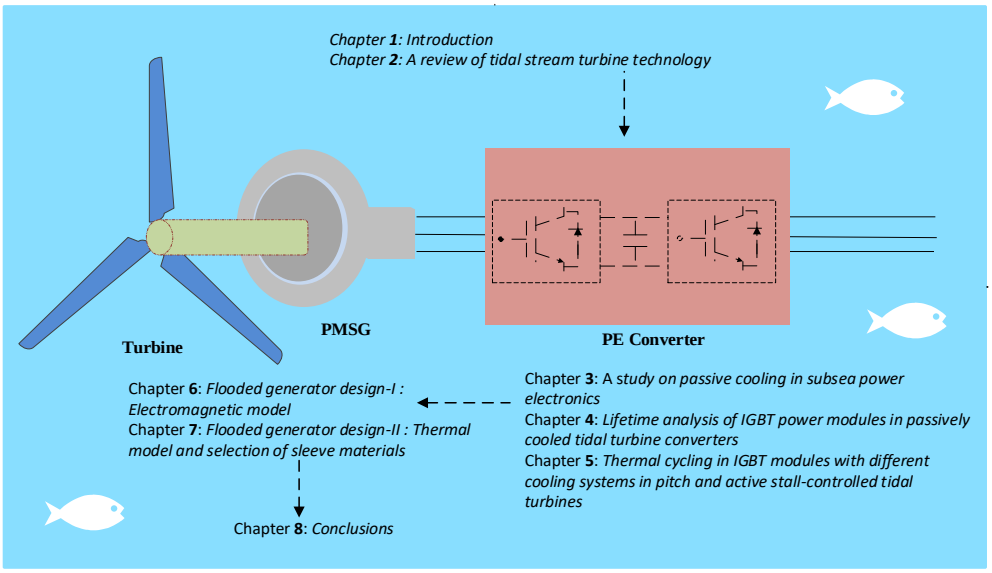

Figure 1.8 Outline of this thesis.

2. **A review of tidal stream turbine technology—** this chapter presents the state-of-the-art tidal turbines, classification of different drive trains, and briefly touches upon some of the futuristic solutions in TST industry.
3. **A study on passive cooling in subsea power electronics—** in this chapter a thermal model for IGBT modules in a passively cooled subsea power electronic converter is presented.
4. **Lifetime analysis of IGBT power modules in passively cooled tidal turbine converters—** this chapter describes the methodology to estimate the useful lifetime of the IGBT modules based on thermal cycling in a subsea converter. It takes into account the effects of turbulence and surface waves on the converter design and the IGBT module lifetime.
5. **Thermal cycling in IGBT modules with different cooling systems in pitch and active stall-controlled tidal turbines—** active and passive cooling systems for IGBT modules are compared in active stall and pitch-controlled TSTs on the basis of lifetime.
6. **Flooded generator design-I: Electromagnetic model—** this chapter highlights the main differences in the design of the flooded generator and the airgap generator. Special attention is placed on additional losses in the rotor sleeve of the flooded generator. Different methods for estimating eddy current losses in the rotor are compared based on their time cost.
7. **Flooded generator design-II: Thermal model and selection of sleeve materials—** this chapter briefly outlines the thermal model of the flooded generator. It uses the electromagnetic and thermal models to give useful insights into what type of materials could be used in sleeves of the flooded generator.

8. **Conclusions and recommendations—** the conclusions and recommendations for future work are highlighted in this chapter.

Each chapter has been written with the intention that it can be read independently from the rest of the thesis. As a drawback, it is possible that some of the information appearing at the beginning of each chapter might seem redundant.

The next chapter presents a state-of-the-art review of the TST technology, and does not contain any scientific contributions. Some readers might want to move directly to Chapter 3.

Bibliography

[1] E. Denny, "The economics of tidal energy," in *Energy Policy*, vol. 37, no. 5, pp. 1914–1924, 2009.

[2] J. Fernandez, J. Kofoed and H. Sørensen, "Predictability and variability of wave and wind: wave and wind forecasting and diversified energy systems in the Danish North Sea," *Aalborg: Department of Civil Engineering*, Aalborg University. DCE Technical reports, no. 156, 2013.

[3] B.'Polagye, J. Epler and J. Thomson, "Limits to the predictability of tidal current energy," in *Proceedings of OCEANS MTS*, Seattle, USA, 2010.

[4] Focal point for marine energy. [Online] https://www.delta.tudelft.nl/article/focal-point-marine-energy [Last accessed: 03 Nov 2019].

[5] S. Waters and G. Aggidis, "Tidal range technologies and state of the art in review," *Renewable and Sustainable Energy Reviews*, vol. 59, pp. 514–529, 2016.

[6] Z. Zhou, F. Scuiller, J. F. Charpentier, M. Benbouzid, and T. Tang, "An up-to-date review of large marine tidal current turbine technologies," in *Power Electronics and Application Conference and Exposition (PEAC),* . IEEE, 2014, pp. 480–484.

[7] Offshore Energy, "Estimate of global potential tidal resources," [Online] https://www.offshore-energy.biz/estimate-of-global-potential-tidal-resources/, [Last accessed: 28-Apr-2020].

[8] P. Evans, "Implications for tidal stream turbine development". Ph.D. Dissertation, Cardiff University, Wales, UK, 2014.

[9] D. Magagna and A. Uihelein, "2014 JRC Ocean Energy Status Report," [Online] https://setis.ec.europa.eu/sites/default/files/reports/2014-JRC-Ocean-Energy-Status-Report.pdf, [Last accessed: 01-Mar-2017].

[10] R. Kempener, and F. Neumann, Tidal Energy Technology Brief. [Online] https://www.irena.org/documentdownloads/publications/tidal_energy_v4_web.pdf [Last accessed: 03 Nov 2019].

[11] D. Magagna, R. Monfardini, A. Uihlein, JRC ocean energy status report 2016 edition. Publications Office of the European Union: Luxembourg. 2016. [Online] Available from: http://www.orizzontenergia.it/download/Appr/ENERGIA%20DAL%20MARE/2017_03_31_Ocean_Energy_Status_Report.pdf [Last accessed: 08 September 2019]

[12] European Commission, SET Plan – Declaration of Intent on Strategic Targets in the context of an Initiative for Global Leadership in Ocean Energy, 2016. [Online] Available from: https://setis.ec.europa.eu/system/files/integrated_set-plan/declaration_of_intent_ocean_0.pdf [Last accessed: 31 January 2020]

[13] D. Magagna, R. Monfardini and A. Uihlein, "Ocean energy in Europe: assessing support instruments and cost-reduction needs," in *International Marine Energy Journal*, vol. 1, no. 1, 2018.

[14] N. Vedachalam, S. Babu, G. Ramadass and M. Atmanand, "Review of maturing multi-megawatt power electronic converter technologies and reliability modeling in the light of subsea applications," *Applied Ocean Research*, vol. 46, pp. 28–39, 2014.

[15] S. Yang, A. Bryant, P. Mawby, D. Xiang, L. Ran, and P. Tavner, "An industry-based survey of reliability in power electronic converters," *IEEE transactions on Industry Applications*, vol. 47, no. 3, pp. 1441–1451, 2011.

[16] C. Qian, A. M. Gheitaghy, J. Fan, H. Tang, B. Sun, H. Ye, and G. Zhang, "Thermal management on igbt power electronic devices and modules," *IEEE Access*, vol. 6, pp. 12 868–12 884, 2018.

[17] M. Andresen, M. Liserre, and G. Buticchi, "Review of active thermal and lifetime control techniques for power electronic modules," in *16th European Conference on Power Electronics and Applications (EPE'14-ECCE Europe), 2014* . IEEE, 2014, pp. 1–10.

[18] W. Liu, D. Zhou, M. Hartmann, F. Iannuzzo and F. Blaabjerg, "Separation of Bond-Wire and Solder Layer Failure Modes in IGBT Power Modules," in *2020 IEEE Energy Conversion Congress and Exposition (ECCE)*, IEEE, 2020, pp. 5289-5295.

[19] D. Magagna, L. Margheritini, A. Alessi, E. Bannon, E. Boelman, D. Bould, V. Coy, E. De Marchi, P. Frigaard, C. Guedes Soares, C. Golightly, J. Hals Todalshaug, M. Heward, M. Hofmann, B. Holmes, C. Johnstone, Y. Kamizuru, T. Lewis, L. Macadre, C. Maisondieu, M. Martini, A. Moro, K. Nielsen, V. Reis, S. Robertson, P. Schild, M. Soede, N. Taylor, I. Viola, N. Wallet, X. Wadbled and B. Yeats, "Workshop on identification of future emerging technologies in the ocean energy sector - 27th March 2018, Ispra, Italy," EUR 29315 EN, European Commission, Luxembourg, 2018, ISBN 978-92-79-92587-0, DOI:10.2760/23207, JRC112635

[20] Ø. Krøvel, R. Nilssen, S. Skaar, E. Løvli, and N. Sandoy, "Design of an integrated 100kw permanent magnet synchronous machine in a prototype thruster for ship propulsion," *CD Rom Proceedings of ICEM*, pp. 117–118, 2004.

[21] N. Baker, S. Cawthorne, E. Hodge, and E. Spooner, "3D Modelling of the generator for OpenHydro's tidal energy system," in *7th IET International Conference on Power Electronics, Machines and Drives (PEMD 2014)* . IET, 2014, pp. 1–6.

[22] I. Bazovsky, "Reliability theory and practice," *Dover Publications*, New York, 2004.

CHAPTER 2

A Review of Tidal Stream Turbine Technology

This chapter presents an overview of the state-of-the-art tidal stream turbine technology, with the focus on the horizontal axis tidal turbines. Various available technologies are classified according to the generator types, location of converters, mounting of the turbines, etc. This overview should give a more clear picture of the recent trends in the industry, and the major challenges on the path to economical exploitation of the tidal energy.

Based on:

- F. Wani and H. Polinder, "A Review of Tidal Current Turbine Technology: Present and Future," in *12th European Wave and Tidal Energy Conference (EWTEC'17)*, Cork, Ireland, 2017, pp. 3707-3712.
- F. Wani, J. Dong and H. Polinder, "Tidal Turbine Generators," in Clean Generators - Advances in Modelling of Hydro and Wind Generators, IntechOpen Books, London, 2020.

2.1 Introduction

Tidal energy can be mainly exploited in two ways: the tidal barrage (or dams) and the tidal stream turbine (TST) technology. The former resembles the hydroelectric generation in that it uses the potential energy of the water, stored at a suitable head. In contrast, the latter is akin to wind turbine technology, as it converts the kinetic energy in the tidal streams into electricity.

A typical tidal barrage system involves storage of water behind a dam during the high tides, and releasing it back during low tides. The possible modes of operation are ebb generation, flood generation or bidirectional generation. Whereas the flood and the ebb modes only generate power during the flood tide and the ebb tides respectively, a bidirectional tidal dam plant can operate during both periods [1]. Turbines used for bidirectional operation are slightly more complex, as they need to be optimized for bidirectional operation. In some cases, pumps are also used to increase the head difference, improving the overall efficiency and capacity factor of the plant [2].

The largest tidal barrage is presently operational at Lake Sihwa in South Korea since 2011, with an operating capacity of 264 MW. Prior to this, La Rance in France was the largest tidal dam rated at 250 MW, operational since 1967 [2]. Figures 2.1 and 2.2 show Lake Sihwa and La Rance tidal range plants respectively.

Though traditionally tidal dam technology was used to harness tidal energy, there are certain drawbacks to it, such as high capital cost and the likely adverse environmental impact. The tidal dam planned across Severn river in England was shelved in 2010 because of these reasons. However, the environmental impact on local flora and fauna due to tidal dams has not been categorically established, with certain studies suggesting that while some species might suffer due to the tidal dams, others might actually flourish [2]. Furthermore, dams built across an estuary or

Figure 2.1 Lake Sihwa tidal range plant, South Korea [Source: G. Aggidis, Lancaster University].

Figure 2.2 La Rance tidal plant, France [Source: G. Aggidis, Lancaster University].

a bay affects the maritime traffic, although they might also act as a bridge for motor traffic [3]. Nonetheless, the drawbacks appear significant enough to impede the growth of tidal dams.

Recently, the concepts of tidal lagoons and tidal reefs, which are adaptations of tidal barrages, are also attracting tidal enthusiasts because of their low impact on marine life and also possibly higher power per unit area enclosed. These technologies are highly expensive at the moment and no commercial scale projects exist as yet [2, 4].

TST technology, presently, is at a lower technology readiness level[1] (TRL), and not as bankable as tidal barrages. However, because of the likelihood of the lower cost of energy, scale flexibility and minimal impact on the local biodiversity, TSTs are more likely the future in tidal industry. Most projects in TST industry came up in early 2000s. This was partly caused by the support of UK's Department of Trade and Industry in 2001, and accordingly the UK has been the world leader in this sector [5].

This review chapter includes both the state-of-the-art designs as well as the designs in the conceptual phase.

2.2 Horizontal and Vertical axis turbines

Similar to the wind turbines, TSTs are also either of the horizontal axis or the vertical axis type. Figures 2.3 and 2.4 show an example of a horizontal axis and a vertical axis tidal turbine respectively. Tidal stream energy can also be harnessed through other topologies such as oscillating hydrofoil, enclosed tip turbine and tidal kites.

Figure 2.3 Horizontal axis tidal stream turbine: NOVA M100 [©Nova Innovation] [6] .

Figure 2.4 Vertical axis tidal stream turbine: Kobold [©LoStrettoNecessario.net] [7] .

[1] Technology Readiness Levels (TRL) are a type of measurement system used to assess the maturity level of a particular technology. `https://www.nasa.gov/directorates/heo/scan/engineering/technology/txt_accordion1.html`

Most of the research and development efforts in exploiting the tidal stream energy have been focused on horizontal axis tidal turbines (HATTs), as shown in Figure 2.5. This is primarily because of their higher TRL as shown in Figure 2.6. HATTs have also proven to be more reliable and survivable in harsher conditions than their vertical axis counterparts [9]. Based on these facts, this chapter shall henceforth only discuss the HATTs.

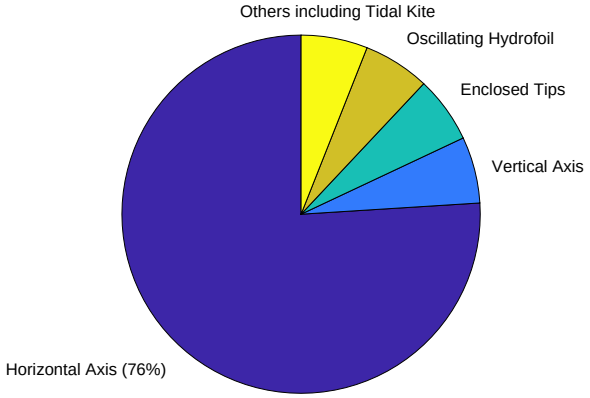

Figure 2.5 Focus of R&D efforts for different tidal stream technologies [Source: [8]]

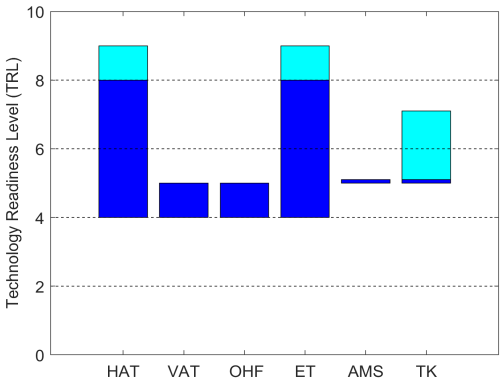

Figure 2.6 Data from 2016. Blue bars indicate the range of TRL levels of various devices, cyan bars indicate testing in 2016. Source: JRC Energy Database [8]. HAT—horizontal axis turbines; VAT—vertical axis turbines; OHF—oscillating hydrofoil; ET—enclosed tips; AMS—archimedes screw; TK—tidal kite.

The power captured by a HATT is given by the same equation as that of a wind turbine. Mathe-

matically, power captured is given by,

$$P = \frac{1}{2} C_p(\lambda, \beta)\ \rho A v^3, \tag{2.1}$$

where C_p is the power coefficient, ρ is the mass density of the water, A is the area swept by the turbine blades and v is the velocity of the tidal stream. The power coefficient, C_p is a function of the tip-speed ratio and the blade pitch angle denoted by λ and β respectively. Tip-speed ratio is the ratio of the blade tip-speed to the incoming velocity of the fluid. A typical $C_p - \lambda$ curve is shown in Figure 2.7.

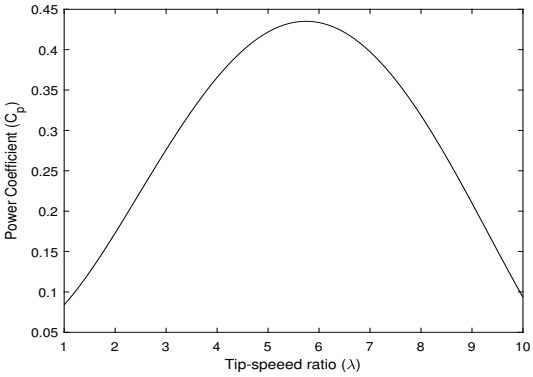

Figure 2.7 A typical $Cp - \lambda$ curve for a typical horizontal axis tidal turbine for constant β; adapted from [10].

2.3 Commercial turbines

Most tidal turbine manufacturers prefer lower power ratings of ≤1 MW to limit the economical risk, and increase the redundancy in case of multiple turbine platforms. However, there are instances where companies have gone upto 2 MW with a single turbine. If the growth in wind sector is any indication, it is likely that in future with more experience, the power level of turbines will increase. However, unlike wind, tidal turbines cannot grow indefinitely in size, and other factors such as protection of marine ecosystem might pose additional constraints. Some of the main tidal energy developers are listed in Table 2.1. Evidently, most of them prefer HATTs.

In the following sections, different technologies used in HATT power take-off systems are presented. The focus is on classifying them based on certain paradigms such as the type of mounting of the turbines, the type of generators, and the placement of converters, etc. This is done to clearly identify the similarities and differences between different manufacturers.

Table 2.1 Some of the main tidal energy developers around the world in 2016, and their device types.

Company Name	Country Base	Device Type	Generator Type	Device Name	Power Rating
Andritz Hydro Hammerfest [11]	Norway	HATT	IG + GB	HS1000	1 MW
Atlantis Resources Limited [12]	UK	HATT	PMSG + GB	AR1500	1.5 MW
Marine Current Turbines [13]	UK	HATT	IG + GB	SeaGen S	1 MW
Nautricity [14]	UK	HATT	PMSG-DD	CoRMaT	0.5 MW
Nova Innovation [15]	UK	HATT	IG + GB	Nova M100	0.1 MW
Schottel Group [16]	Germany	HATT	IG + GB	SIT	0.070 MW
Scotrenewables [17]	UK	HATT	IG + GB	SR2000	2 ×1 MW
Tocardo Tidal Turbines [18]	Netherlands	HATT	PMSG-DD	T200	0.25 MW
Minesto [19]	Sweden/UK	Tidal Kite	-	DG500	0.5 MW
Deepwater Energy BV [20]	Netherlands	VATT	-	Oryon Water-mill	0.25 MW
OpenHydro DCNS* [21, 22]	France (Irish subsidiary)	HATT	PMSG-DD	OpenHydro	2 MW
GE (France)* [23, 24]	France	HATT	-	Oceade	1.4 MW
Voith Hydro* [25]	Germany	VATT	-	Voith hyTide	1 MW

IG: Induction Generator; GB: Gearbox; PMSG: Permanent Magnet Synchronous Generator; DD: Direct Drive.
*no longer develop tidal turbines
The table only lists a single device from the mentioned manufacturers. Devices of other power ratings may also exist.

2.4 Classification based on hydrodynamic components

2.4.1 RIM and POD configurations

Based on the placement of the generator with respect to the turbine, tidal stream turbines are of two types: pod and rim-driven configurations.

In the pod configuration, the generator is located behind the turbine blades on the horizontal axis. This is similar to a conventional horizontal axis wind turbine, and appears to be the most common type of tidal turbine currently in use. Figure 2.3 shown earlier represents an example of a pod type turbine. Among other factors, the external diameter of the generator is constrained to avoid high resistance to the flow across the blades [26]. Some manufacturers which use the pod type turbines are Nova Innovation, Atlantis Resources, Andritz Hydro Hammerfest, Tocardo and Schottel.

In the rim-driven type, the generator is placed in a ring surrounding the turbine blades. Figure 2.8 shows an example of a rim-driven generator. Here the internal radius of the generator is constrained by the rotor diameter of the turbine. Rim-driven turbines can be expected to have higher hydrodynamic efficiency compared to the pod configuration. In pod turbines larger generator diameter may affect the water flow across the turbine compromising efficiency [28]. DCNS-Openhydro's Open Centre turbine seemed to be the only prominent example of the rim-driven turbine, among the major manufacturers of the tidal turbines [21].

Between 1999 and 2005, Tocardo tested and compared a venturi-duct rim-driven generator and a two-bladed direct-drive pod generator. Based on their findings, they concluded that the latter seemed more economical than the former [29].

Figure 2.8 DCNS OpenHydro's rim-driven generator, reproduced from [27]; (Credit: Mike Brookes-Roper).

2.4.2 Number of blades

Most horizontal axis tidal turbines either use a 2-bladed or a 3-bladed configuration. According to [9], more than 50% of the horizontal axis tidal turbines use a 3-bladed turbine, whereas only 25% use a 2-bladed turbine. Other designs using more than 3 blades also exist. The choice of the number of blades may depend on the power rating of the turbine, site conditions, the loading of blades, and most importantly, manufacturing, transport and assembly costs.

Advantages of 2-bladed turbines include low cost, easy installation, and a higher tip-speed ratio. The latter can either reduce the size of the gearbox or the generator (in direct-drive case). Disadvantages of 2-bladed turbines include considerable wake and cavitation problems due to high rotational speed, and relatively higher tower effect compared to a 3-bladed turbine. Tocardo T2 (and T2s—advanced version of T2) turbines, shown in Figure 2.9 are an example of 2-bladed turbines. Five T2 tidal turbines were installed in the Eastern Scheldt storm surge barrier in the Netherlands [30], which showed promising results in earlier stages.

Figure 2.9 Tocardo T2 turbines. Image source [31][©Tocardo Tidal Power].

A 3-bladed turbine—like its wind counterpart—is more popular. Three-bladed turbines are preferred because of the higher hydrodynamic efficiency, less impact due to the tower wake and cavitation. Additionally, such turbines also tend to have a lower cut-in speed. Furthermore, not much is gained by increasing the number of blades beyond three, be it in terms of efficiency or stability [32]. An example of a 3-bladed turbine is the Schottel's Instream turbine, shown in Figure 2.10 [16].

Number of blades also has a significant impact on the $C_p - \lambda$ characteristics of the turbine. Higher blade number is likely to result in a turbine with a sharper C_p curve, and hence better stall performance. On the other hand, two-bladed turbines usually have a flatter C_p curve to allow operation over a wide tip-speed ratio. Furthermore, the blade chord and twist distributions also

influence the $C_p - \lambda$ curve [33].

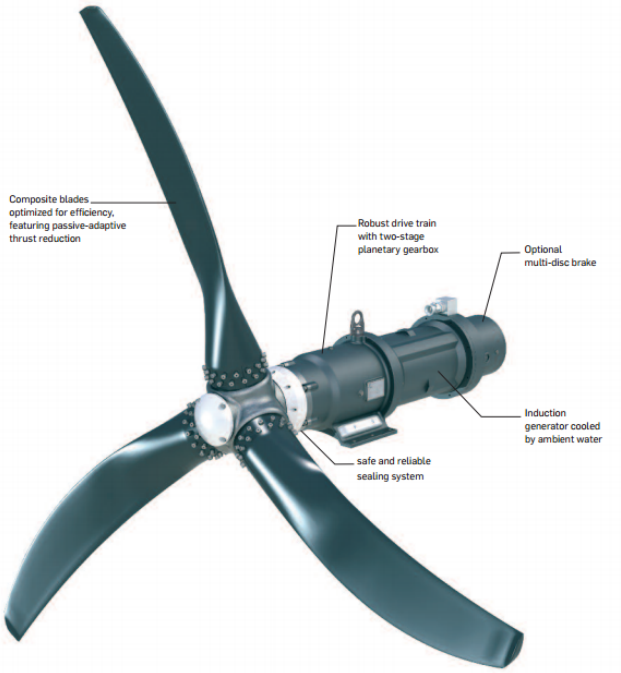

Figure 2.10 Schottel's Instream turbine. Image source [16].

2.4.3 Fixed-pitch and Variable-pitch

The blades of the tidal turbine can either be held fixed or pitched in order to regulate the power output from the turbine. In cases where the blades cannot be pitched, power control is achieved by stall regulation (active or passive). In passive stall, the blade profile is designed to stall beyond the rated tidal speed. However, this may also result in a poorer efficiency below rated speeds. A more recent approach is to use active speed stall-control [34]. Examples of the fixed-pitch system include Schottel's Instream turbine, shown in Figure 2.10 [35], and Nova's M100 shown in Figure 2.3. The representative power, speed and torque curves for an active stall-controlled turbine are shown in Figure 2.11.

On the other hand, a more active and desirable (in terms of energy output) control is achieved by pitching the blades. Obviously, employing the pitch control increases the cost and may compromise reliability. However, some manufacturers prefer it over the fixed-pitch solution, especially with higher power ratings ($\geq$ 1 MW). The representative power, speed and torque curves for a pitch-controlled turbine are shown in Figure 2.12.

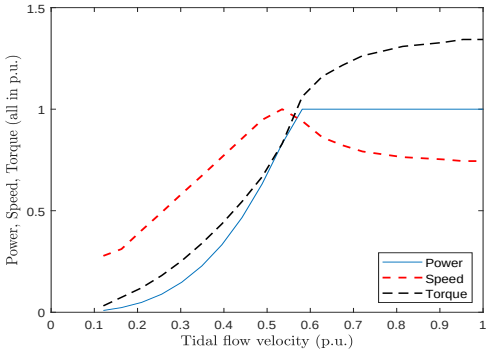

Figure 2.11 Representative curves for an active speed stall-controlled tidal stream turbine.

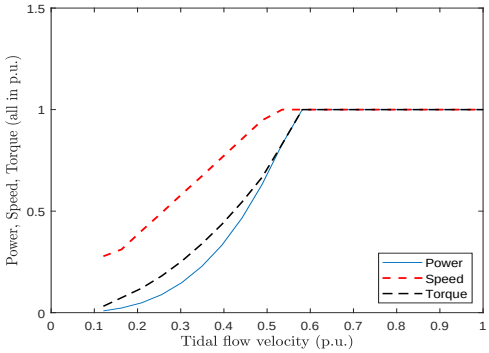

Figure 2.12 Representative curves for a pitch-controlled tidal stream turbine.

Atlantis Resources AR1500 tidal turbine, shown in Figure 2.13, employs a variable pitch control. The pitch control comes into action only above rated speeds to limit the output power from the turbine. A single actuator drives all the three blades together. This reduces the number of components increasing the possibility of adding more redundancy in the system [12]. SeaGen project employed two (1 MW each) turbines from Marine Current Turbines (Siemens) shown in Figure 2.14, which also used a variable pitch control. This is done to further increase the efficiency of the turbine and also limit structural forces, in addition to the maximum power point tracking due to speed control [13]. Yet another example of the pitch-controlled turbine is the Andritz Hydro Hammerfest turbine [11].

An interesting concept of pitching the blades is found in the 2-bladed Tocardo T1 turbine developed and tested around 2012. In this design, both the blades are simultaneously turned by 180°during the slack tides for reverse flow operation [29]. This is more akin to the yaw control than a pitch control.

Figure 2.13 Gravity based seabed mounting of AR1500 [12] [©Atlantis Resources].

Figure 2.14 SeaGen-S turbines [13] [©Marine Current Turbines-A Siemens business].

2.4.4 Yaw control

Yaw control is essentially the orientation control of the turbine main axis. Changing the orientation of the turbine axis, changes the angle of attack with the blades, thereby influencing the power coefficient, C_p. Furthermore, it increases the efficiency and reduces the load on the blades.

To limit the complexity and a potential fault point of the submerged tidal turbine, yaw control in tidal turbines is not omnipresent. Also, the need for yaw control in tidal turbines is not as significant as in wind turbines. But since the tides change direction by about 180°after every 6 hours or 12 hours, some manufacturers do prefer having the yaw control. An example of such a turbine is the Atlantis Resources AR1500, shown in Figure 2.13, where the yaw is fixed during the ebb and flood phases, and is operated only during the slack tides to face the next incoming tide [12]. Another example was General Electric's (GE) Oceade 1.4 MW design, shown in Figure 2.15. Oceade turbine used a thruster at the rear of the nacelle during the slack tide to ensure that the turbine blades face the incoming tide[23]. However, in 2017, GE shelved the development of this device [24].

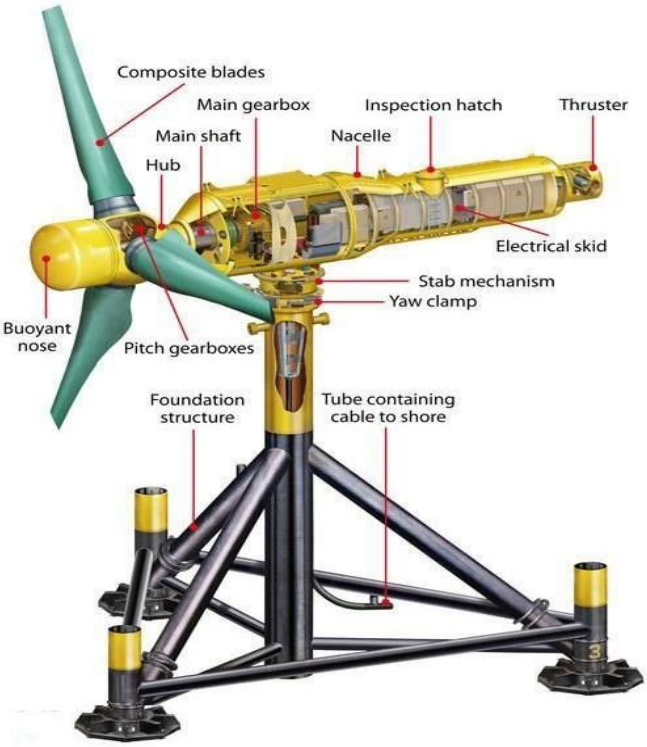

Figure 2.15 General Electric's (formerly Alstom) Oceade tidal turbine with a yaw thruster [36].

A commonly used approach is to design blades with optimal efficiency in both upstream and downstream phases. This compromises the maximum achievable efficiency in either direction. However, this loss in efficiency is likely offset by the overall higher reliability without yaw control.

2.5 Classification based on mounting

Most tidal turbines could be mounted in one of the four topologies described below [37]. Different adaptations of these basic topologies are also implemented as mentioned in [38]. Quite often, a particular turbine can be mounted in different ways, and the choice of mounting is highly dependent on the site conditions.

2.5.1 Floating tethered

Bluewater, in collaboration with various other partners including Tocardo and Schottel, commissioned the BlueTEC floating platform in 2015. The turbine and the generator are submerged and

hanging from the bottom of the platform as shown in Figure 2.16. The floating platform is tethered to the seabed and can be easily moored to the shore for major overhauling of the system. The platform also houses the power electronic converter and other critical equipment for easy and quick access during maintenance. The platform was in use (as of 2017) to test different turbines and was connected to the Dutch grid in Texel, Netherlands [40, 41].

Figure 2.16 Tocardo T1 turbine mounted under floating BlueTEC platform. Image source [39].

Another example of the floating tethered system is the Tocardo's (proposed) universal floating system (UFS) 1.5 MW system, which comprises a floating U-shaped platform with 5 Tocardo T2 turbines [42]. Tocardo's UFS is shown in Figure 2.17. However, as far as the author is aware, this device was never installed in practice.

2.5.2 Submerged tethered

An example of the semi-submerged systems is the Schotell's Triton S platform concept shown in Figure 2.18. The Triton system can have multiple cross arms, each with multiple turbines to allow for redundancy and megawatt level energy capture. Two tether arms hold the Triton to the seabed through a gravity based foundation, besides allowing the Triton to orient itself in the flow direction. Similar to the floating tethered system, vulnerable electronics are housed in the floating spar buoys [16]. As far as the author is aware, no full-scale prototype was ever tested in a real environment, only a scaled model was tested in 2014.

Another possibility is the fully submerged and tethered system, for example, the Sustainable Marine Energy's PLAT-I platform. The platform remains fully submerged most of the times, but can be brought to the surface for maintenance by releasing the mooring lines. The first PLAT-O platform was deployed in the Isle of Wight, England with two 50 kW Schotell Instream turbines [16, 43].

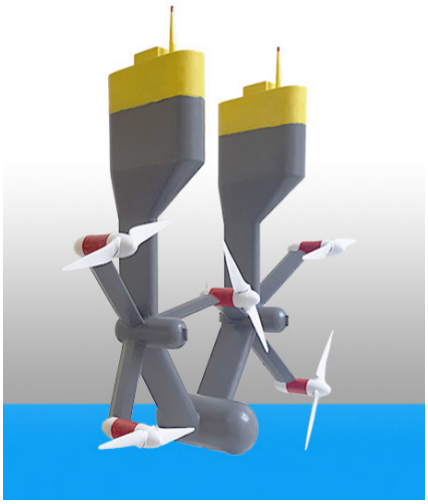

Figure 2.17 Tocardo's UFS, an offshore solution. Image source [42].

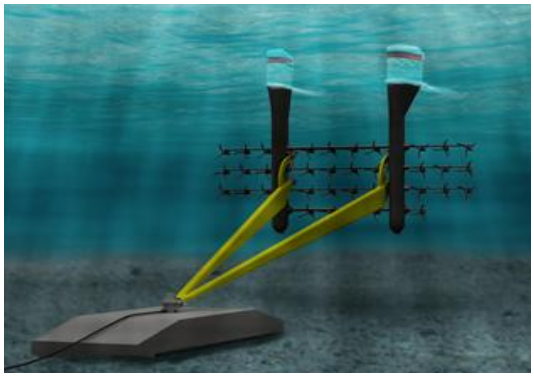

Figure 2.18 Schottel Triton S platform with semi-submerged tethered mounting. Image source [41]

2.5.3 Seabed bottom-mounted

Mounting of turbines near the seabed minimizes the instability due to surface waves and provides more solid foundation compared to the aforementioned mounting topologies. This type of mounting seems to be the most commonly used one. Most seabed bottom-mounted turbines employ gravity based foundations. Figure 2.13 shows the Atlantis Resources AR1500 turbine mounted on the support structure tower held by the gravity based foundation [12]. Other examples include the Openhydro's Open Centre turbine and Nova M100 [21]. This type of mounting does

not penetrate into the seabed, therefore, overturning (tipping) moments need to be carefully considered during the design. To limit the damage to the seabed by occupying less surface and provide more stability, Sabella has proposed the use of cast-iron tripod structure over the traditional concrete based gravity foundations [44].

2.5.4 Seabed pile-mounted

Due to the success of pile foundations in the offshore wind, it was swiftly adopted in the tidal turbines. Major problems associated with the pile foundations are due to the lateral loads by tidal currents which induce fatigue in the structure, and the grout failures between the transition piece and the monopile [44]. However, pile foundations also provide the possibility of holding a platform above the water level to host power electronic converters and other necessary equipments. For example, under the SeaGen project (from Marine Current Turbines-Siemens), twin 1 MW turbines were installed on a cross arm mounted on a monopile foundation, as shown in Figure 2.14. The surface piercing steel tower, which hosts the power electronic converter and the resistive dump load for emergencies, is also supported by this monopile. The cross arm holding turbines could be moved vertically above the water surface for maintenance without the need of a large marine vessel. This flexibility is not possible with gravity based foundations [13].

2.6 Classification based on the power take-off system

2.6.1 Generator type

Given the high costs involved in the maintenance of tidal turbines, manufacturers tend to rely on proven technologies with minimum failure rates. For generators, this means squirrel cage induction machines and permanent magnet (PM) synchronous machines are widely used. PM machines have higher torque density than induction machines, but tend to be more expensive. Other topologies, such as electrically excited synchronous machines and doubly fed induction machines, which are used in wind turbines, are rarely employed in tidal turbines.

In this subsection, we classify generators into two main categories: high-speed generators with a gearbox, and low-speed direct-drive generators. A basic representation of both the geared and the direct-drive topologies are shown in Figures 2.19 and 2.20 respectively.

High-speed and Low-speed (direct-drive) generators

The size of the generator is directly related to its torque rating, which implies for the same power, high-speed machines are smaller. In addition to manufacturing costs, transport and assembly costs are also likely to be lower for high-speed machines. Since tidal turbines rotate at low speeds, a gearbox is necessary between the turbine and the high-speed generator. Within high-speed generators, further classification is possible based on synchronous and induction generators.

Atlantis Resources AR1500 turbine, shown in Figure 2.13, uses a radial flux surface permanent magnet synchronous generator with a 2-stage planetary gearbox [12]. On the other hand, Andritz

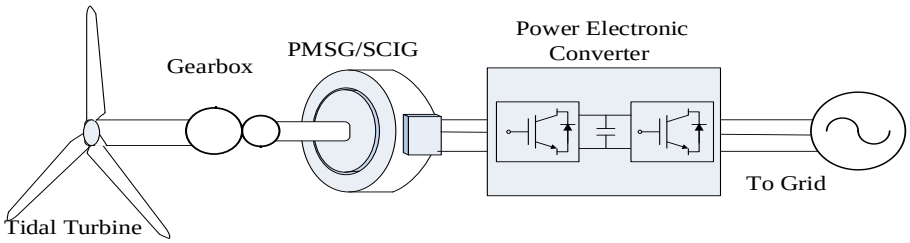

Figure 2.19 Tidal turbine drive train with a gearbox and a generator (PMSG—permanent magnet synchronous generator; SCIG—squirrel cage induction generator). Image adapted from [45].

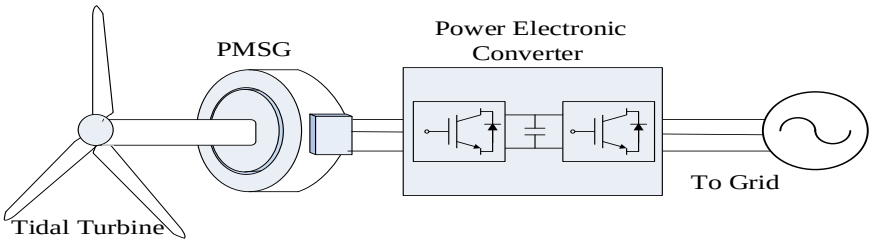

Figure 2.20 Tidal turbine drive train with a direct-drive synchronous generator. Image adapted from [45].

Hydro Hammerfest HS1000 and Schottel's Instream turbine comprise induction generators with a 3-stage and a 2-stage planetary gearboxes respectively [9, 35].

Another possibility within high-speed generators is the doubly-fed induction generator (DFIG) drive train shown in Figure 2.21, which is widely used in the wind industry. Whereas both PM and induction generators require a power electronic converter of the full kVA rating, DFIGs require a partially rated converter. However, they are not preferred as yet in the tidal industry primarily because the slip-rings and brushes in a DFIG require frequent maintenance. Furthermore, it is expected that the PMSG based systems will be more efficient compared to DFIG based systems, over the operational speed range [46]. On the other hand, low-speed direct-drive generators can be directly coupled to the turbine without the need for a gearbox. This topology significantly improves the overall reliability and efficiency of the turbine-generator system, by eliminating the gearbox failure modes and losses.

To avoid thick stator and rotor back iron, direct-drive generators usually have high pole numbers, and thus smaller pole-pitch. This makes PM machines suitable for direct-drive applications because induction machines with high pole numbers result in an inefficient design due to lower power factor [47]. DCNS-Openhydro and Tocardo T2 turbines, shown in Figures 2.8 and 2.9 respectively, use a direct-drive PM generator.

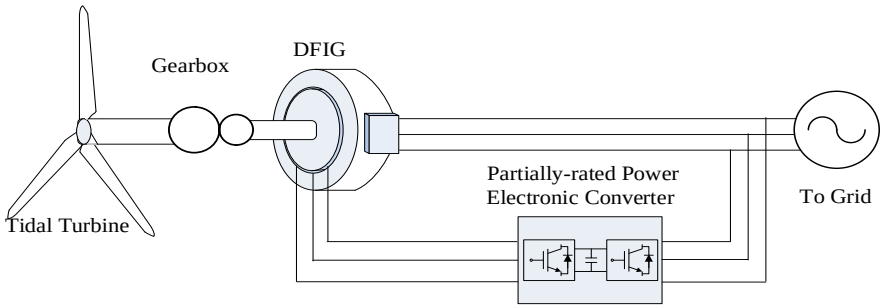

Figure 2.21 DFIG based drive train. Image adapted from [45].

Radial and Axial flux generators

Generators are sometimes also classified based on the direction of the magnetic flux lines from rotor-to-stator with respect to the generator axis. Two main types of generators according to this classification are: radial flux and axial flux machines. In radial flux machines, magnetic flux lines are perpendicular to the rotational axis of the generator, whereas in axial flux machines, flux lines are parallel to the rotational axis. Figure 2.22 illustrates these two configurations. Although transverse flux generators also exist, no example of such a generator type was found to exist in tidal turbines [49].

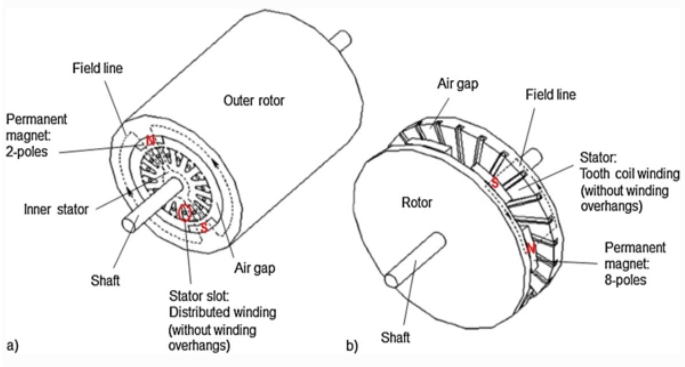

Figure 2.22 Structures of (a) radial flux surface mounted PM machine, and (b) axial flux surface mounted PM machine. Image reproduced from [48].

Tidal stream turbines with radial flux as well as axial flux generators exist in the field. Atlantis Resources' AR1500 is an example of a TST with a radial flux PM generator [12]. An example of axial flux PM generator can be found in Nautricity's contra-rotating Cormat turbine [50].

2.6.2 Location of converters

With respect to the placement of the converters, mainly three possibilities exist. They are as follows.

- **Onshore converters:** Experience from the offshore wind industry suggests that the failure rate among converters is much higher than the generators [51]. This has prompted most tidal turbine manufacturers to place converters onshore, giving easy access for frequent maintenance. An example of this is the Andritz Hydro Hammerfest (AH1000 MK1) and Atlantis Resources (AR1500) turbines used in the MeyGen project [52].
- **Housed in the nacelle:** Clearly, onshore placement of converters for each turbine in a tidal array will result in huge cabling costs for arrays. Therefore, the placement of converters close to the generator is desirable. A simple way to achieve this is by placing the converters in the sealed nacelle alongside the generator. GE's (formerly Alstom) Oceade turbine was an example of this configration [23]. In an array, the power from multiple converters (or generators) is fed into a common DC or AC bus, where the voltage is stepped up for transmission to shore.
- **Offshore platform mounting:** To provide easy and quick access for the converter repairs, a floating or a pile-mounted surface-piercing platform is also used. An example of each case is the Bluewater's BlueTEC platform and the SeaGen project, shown in Figures 2.16 and 2.14 respectively.

2.7 Challenges and path forward

As mentioned in the previous chapter, LCOE target set for tidal energy in the year 2030 is 150 EUR/MWh [53], whereas in 2016 values ranged between 540-710 EUR/MWh [8]. This vast range in LCOE was partly because of the uncertainty in the capital costs, which varied from 4400 EUR/kW to 12400 EUR/kW [54]. Furthermore, capacity factors for different devices ranged between 19% and 40% (2018 values) [54].

About 12 MW of TSTs remained installed by 2018 [55, 56]. Since 2010 about 27 MW was installed, out of which roughly 15 MW was decommissioned [56]. As per the current trends and announced projects, target is to have around 1 GW installed capacity by 2025 [54]. However, this seems likely only if TSTs driven by innovation result in more reliable devices with higher availability. This will boost investor confidence, leading to more deployment of TSTs. As more and more devices are deployed, LCOE can further reduce as shown by the forecast in Figure 2.23. Economies of scale and reducing of interest rate[2] can aid in bringing the cost down somewhat along the lines of wind turbines. Higher availability also means increase in the capacity factor, which again will result in reducing the LCOE as depicted in Figure 2.24.

In addition to technological challenges of operating in harsh marine environment, TST industry faces other challenges too. Locations suitable for economic exploitation of the tidal energy are

[2] Higher uncertainty about the return implies higher borrowing interest rate.

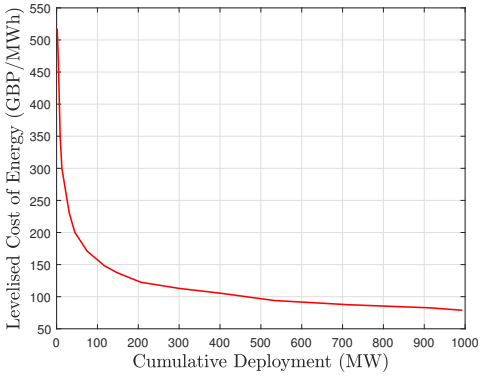

Figure 2.23 Projected LCOE with respect to cumulative deployment; this analysis was carried out by Offshore Renewable Energy Catapult (OREC) [57].

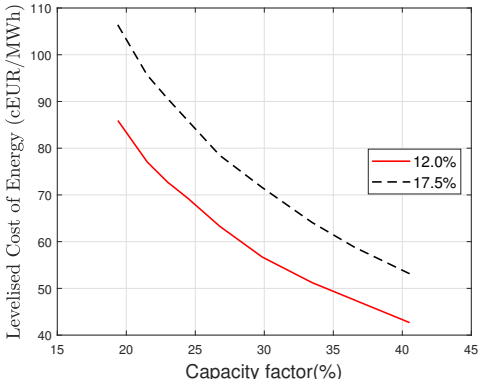

Figure 2.24 Decrease in LCOE as a function of capacity factor at different interest rates; data taken from 2016 [54].

often far from the grid network. In most cases, the local grid almost invariably needs to be upgraded to accommodate power input from the turbines. The costs involved in the expansion of the grid or its upgrade at the desired location sometimes forms a significant bottleneck in setting up a tidal farm [9].

A few tidal turbines are unlikely to inflict significant damage on the local biodiversity; this has been concluded by several studies [29]. Even so, it would be too simplistic to draw the same conclusions, without credible research, for a tidal farm with several tidal turbines. Some projects have undertaken an extensive environmental impact assessment at various stages during the project to assess the impact on the local marine life, MeyGen project is a case in point [58]. However, unlike the wind turbines, tidal turbines face less resistance from the local population because of its near-zero visual impact.

From the economic viewpoint, it is difficult to predict the future of the tidal turbine technology. The success of the prototypes, currently under design and testing, on site is indispensable for encouraging future investments before economies of scale can take over bringing down the cost of energy. The next section presents some possible future trends in the TST power take-off system design, which might prove crucial in lowering the LCOE.

2.8 Possible future trends in power take-off design

Clearly, other futuristic design solutions exist, but we only consider the ones analyzed in this thesis. First, a flooded generator concept is presented, followed by the concept of submerged power electronic converter.

2.8.1 Flooded generator

Most tidal turbine manufacturers, such as the one shown in Figure 2.13, use a conventional airgap generator. In an airgap generator, the stator-rotor gap inside the generator is occupied by air. For tidal turbines, the airgap generator has to be enclosed in a water-tight nacelle. The inner nacelle space is isolated from the sea water using a high-pressure rotary seal on the rotating shaft of the turbine, as shown in Figure 2.25. Sealing the nacelle protects against the corrosion and/or electrical breakdown of critical components, such as the generator coils, magnets, and bearings.

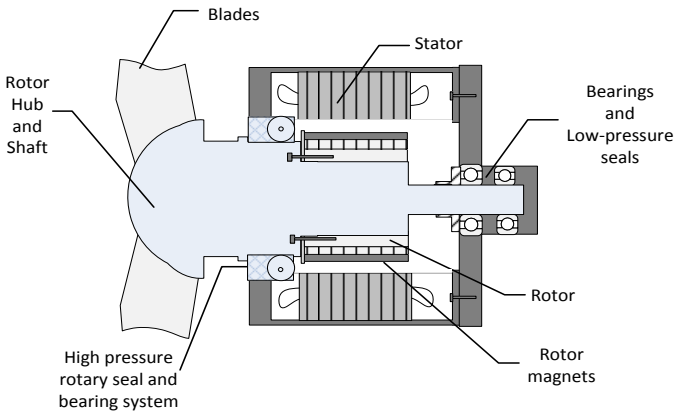

Figure 2.25 A sealed airgap direct-drive generator; only necessary details for discussion are shown here.

The drawback with this topology is that it makes the power take-off (PTO) system vulnerable to water ingression in the nacelle, mostly via the leakage through the seals [8, 59]. Water-tight rotary seals on the shaft are also susceptible to wear, and generate losses due to friction. Besides

decreasing efficiency, these losses may end up heating the bearings and compromising its lifetime [59]. To avoid high friction losses, small leakage of the fluid is allowed, which acts as a lubrication film between the seal faces. Whereas, a thicker fluid film decreases wear, it will also increase leakage. Normally in ships or submarines this leakage water accumulated over time is drained using a bilge pump. Having a bilge pump in a tidal turbine will add to the cost, and add another potential failure mode. Nonetheless, large tidal turbines ($\geq$ 1 MW) do use bilge pumping systems alongside dehumidifiers. In addition to wear, seals usually fail when subjected to unforeseen or abnormal operating conditions [60]. This includes foreign material intrusion, such as sediments in the sealing faces, imperfect shaft alignment, corrosion, sticking and clogging.

To prevent seal breakdown regular maintenance of the seals is necessary. Performing preventive maintenance can also increase the O&M expenditure if the maintenance cycle is frequent or poorly timed. LCOE studies for tidal energy systems suggest that for competing with other renewable energy sources, tidal turbines must survive for about 20 years, with a service interval of 5 years [61]. Unfortunately, not much data is publicly available about the reliability of seals in tidal turbines, still it is possible to have a reasonable estimate about seal reliability from other applications. For instance, the failure rate of seals in marine propellers [62], or canned motor pumps [63], can provide a rough guide about the seal failure rates in tidal turbines. From the failure rate of seals in propellers and canned motor pumps, it appears challenging to completely rely on high-pressure seals for the aforementioned maintenance interval without any failure or leakage. This has led to a discussion about the possible use of flooded generators in tidal turbines [61, 64].

A flooded generator—also known as wetgap generator—is where the stator-rotor gap of the generator is filled with sea water. The interior view of a typical flooded generator is shown in Figure 2.26. Among early tidal turbine developers, DCNS-Openhydro (shown in Figure 2.8) and Voith tried to use this topology. More recently, Nautricity's Cormat and Nova Innovation's TiPA are two examples of tidal turbines where flooded generators were used.

Envisaging the use of flooded generators in tidal energy generation has been a recent development. On the other hand, their motor counterparts—commonly known as canned motors—have been around for quite some time [66].

Inside a flooded generator, not only electromagnetic parts but also other components, such as bearings, are susceptible to corrosion; same is true for the canned motors. Normally canned motors are used in pump applications [63]. This means there is usually a high-pressure fluid available which can be used as a lubricant in either a hydrostatic or a hydrodynamic bearing. It is obvious that non-corrosive materials with good resistance to abrasion must be used in these bearings.

In an ideal scenario, flooded generators would also be equipped with sea water-lubricated hydrodynamic bearings. But there are obvious problems to this solution. First, the tidal turbines usually run at low speeds (<40 rpm); and second, the sea water has very low viscosity. Both of these would mean too thin a fluid film thickness for good hydrodynamic lubrication [59]. Hydrostatic water-lubricated bearings would require an external motor-driven pump, which not

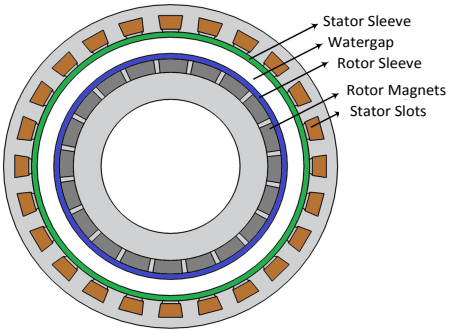

Figure 2.26 A representation of interior view of a flooded generator; inspired from [28, 65]. The figure is not drawn to scale.

only adds to the cost but also creates another potential fault point. Therefore, most tidal turbine manufacturers prefer commonly used roller bearings with some oil/grease lubrication. In this direction, biodegradable oil lubrication is an excellent way forward.

The drawback with using roller bearings is that they are susceptible to corrosion, silt penetration and fatigue due to cyclic stresses. In such a case, a high pressure seal is still required, but it is better protected from debris and marine growth, and can often be smaller than in the sealed airgap design. Also, in a flooded generator, it is also possible to fill the space inside the generator with fresh water at a slightly higher pressure than the ambient pressure. Filling the generator with clean/fresh water might increase the life of hydrodynamic bearings inside the generator.

To avoid fouling or clogging of organic material in the flooded gap, it is likely that a debris seal will be used in tidal turbines, thereby preventing the free water circulation in the watergap [67]. These seals are in addition to the bearing seals, as illustrated in Figure 2.27. However, debris seals are not required to provide high-pressure sealing—but only block large particles including marine life from entering the generator—which means they are cheaper and require less maintenance.

To this point, a general structural design of the flooded generators was presented here. In this thesis we take up the electromagnetic and thermal design of the flooded generators again in Chapter 6.

2.8.2 Power electronics

In section 2.6.2 we discussed that for array applications it is preferable to have power converters housed in the nacelle. However, a drawback of this arrangement is limited access to the converters in case of the converter breakdown. Consequently, reliability of converters assumes high priority.

In the Introduction chapter we talked about thermal cycling in IGBT power modules being one of

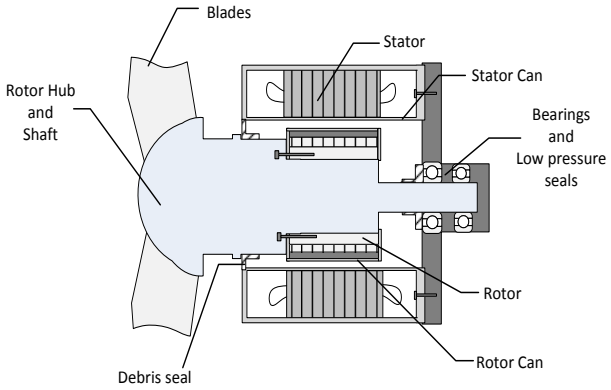

Figure 2.27 A representative figure of a Flooded generator; only necessary details for discussion are shown here.

the most prominent failure modes in power electronic converters. This problem can be mitigated by adequately cooling the power modules. Normally power modules are cooled by mounting them on heat sinks which are cooled either by fan or by liquid coolant flow through the heatsink. The drawback of these systems is the possible breakdown of active mechanical components—fan or pumps [51].

A possible solution to addressing this problem is to use a passively cooled system, which does not use any moving/rotating device. In the following three chapters we discuss the lifetime of power modules for submerged converters. We begin by explaining the thermal model in Chapter 3, before moving on to estimate the power module lifetime in TST converters in Chapters 4 and 5.

2.9 Conclusion

Despite the maturity of the tidal barrage technology, the capital cost and the environmental impact involved with tidal dams has almost entirely shifted the focus towards the tidal stream turbines. Because of the subsea operation and the challenges associated with it, tidal turbines are currently at a lower TRL than would be expected for economic exploitation.

Frequent maintenance of gearboxes, resulting in high O&M costs, has prompted a trend towards direct-drive generators. The design and costs for the direct-drive generators should be carefully investigated as larger diameter of the generator could impede the water flow, reducing the efficiency. Moreover, the cooling properties of the sea water should be exploited as much as possible to reduce the cost of the drive train and increase its lifetime. Flooded generators could prove to be a promising alternative in TSTs. Not only are they inherently designed to have fewer failure modes, but can also utilize sea water for more efficient cooling.

For large scale tidal turbine farms, onshore converters are impractical. Therefore, power electronic converters housed in a subsea nacelle, or mounted on floating platforms or surface piercing foundations are suitable alternatives. Because of the high failure rates in converters, it is imperative to investigate and design converter topologies which result in longer expected lifetimes. This can be achieved by overrating of components, using passive cooling systems or using converter topologies and control systems which reduce stress on converter components preventing their premature failure.

Bibliography

[1] S. Waters and G. Aggidis, "Electricity generation by the tidal barrages," *Energy Procedia*, vol. 12, pp. 928–935, 2011.

[2] S. Waters and G. Aggidis, "Tidal range technologies and state of the art in review," *Renewable and Sustainable Energy Reviews*, vol. 59, pp. 514–529, 2016.

[3] F. O. Rourke, F. Boyle, and A. Reynolds, "Tidal energy update 2009," *Applied Energy*, vol. 87, no. 2, pp. 398–409, 2010.

[4] The Economist, "Swansea tidal power project launches 11th-hour £1m fundraising drive". [Online] https://www.theguardian.com/business/2019/dec/04/swansea-tidal-power-project-launches-11th-hour-1m-fundraising-drive, [Last accessed: 02 May 2020].

[5] P. Fraenkel, "Marine current turbines: pioneering the development of marine kinetic energy converters," *Proceedings of the Institution of Mechanical Engineers, Part A: Journal of Power and Energy*, vol. 221, no. 2, pp. 159–169, 2007.

[6] M. Harris, "Nova, ELSA tidal unit begins generation at Shetland array". [Online] https://setis.ec.europa.eu/sites/default/files/reports/2014-JRC-Ocean-Energy-Status-Report.pdf, [Last accessed: 29 Mar 2017].

[7] L. S. Necessario, "Kobold Turbine". [Online] http://www.lostrettonecessario.net/Kobold.html, [Last accessed: 29 Mar 2017].

[8] D. Magagna, R. Monfardini, and A. Uihlein. JRC ocean energy status report 2016 edition. Publications Office of the European Union: Luxembourg. 2016. [Online] http://www.orizzontenergia.it/download/Appr/ENERGIA%20DAL%20MARE/2017_03_31_Ocean_Energy_Status_Report.pdf [Last accessed: 08 Sep 2019]

[9] D. Magagna and A. Uihelein, "2014 JRC Ocean Energy Status Report". [Online] https://setis.ec.europa.eu/sites/default/files/reports/2014-JRC-Ocean-Energy-Status-Report.pdf, [Last accessed: 01 Mar 2017].

[10] Zhou, Z.; Scuiller, F.; Charpentier, J. F.; El, M.; Benbouzid, H.; Tang, T. Power control of a non-pitchable PMSG-based marine current turbine at overrated current speed with flux-weakening strategy. *IEEE Journal of Oceanic Engineering*, 2015, 40, 536–545.

[11] Andritz Hydro Hammerfest, "Tidal Turbines". [Online] https://www.andritz.com/resource/blob/61614/cf15d27bc23fd59db125229506ec87c7/hy-hammerfest--1--data.pdf, [Last accessed: 03 Apr 2020].

[12] Atlantis Resources, "AR1500 Tidal Turbine". https://www.atlantisresourcesltd.com/wp/wp-content/uploads/2016/08/AR1500-Brochure-Final-1.pdf, [Last accessed: 20 Feb 2017].

[13] Marine Current Turbines, "SEAGEN-S 2 MW". [Online] https://www.atlantisresourcesltd.com/wp/wp-content/uploads/2016/08/SeaGen-Brochure.pdf, [Last accessed: 20 Feb 2017].

[14] NAUTRICITY, "How CoRMaT works". [Online] https://www.nautricity.com/cormat/cormat-power/, [Last accessed: 20 Feb 2017].

[15] Nova Innovation, "NOVA M100". [Online] https://www.novainnovation.com/nova-m100, [Last accessed: 20-Feb-2017].

[16] Schottel Hydro, "Cost Effective Power From Currents". [Online] https://www.schottel.de/fileadmin/data/pdf/SCHOTTEL_HYDRO/SCHOTTEL_HYDRO_Instream_Energy.pdf, [Last accessed: 28 Apr 2020].

[17] Scotrenewables Tidal Power Ltd, "SR2000". [Online] http://www.scotrenewables.com/technology-development/sr2000, [Last accessed: 08 Apr 2017].

[18] TOCARDO, "Tocardo T-2 Tidal Turbines". [Online] https://www.tocardo.com/tocardo-t2/, [Last accessed: 08 Apr 2020].

[19] Minesto, "The future of renewable energy". [Online] https://minesto.com/our-technology, [Last accessed: 08 Apr 2020].

[20] Deepwater Energy BV, "Oryon Watermill". [Online] https://www.oryonwatermill.com/, [Last accessed: 08 Apr 2020].

[21] Openhydro, a DCNS energies company, "Open Centre Turbine". [Online] http://www.openhydro.com/Technology/Open-Centre-Turbine, [Last accessed: 21 Feb 2017].

[22] EMEC, "Open Hydro". [Online] http://www.emec.org.uk/about-us/our-tidal-clients/open-hydro/, [Last accessed: 20 Sep 2020].

[23] GE Renewable Energy, "Oceade Tidal Turbine". [Online] https://www.gerenewableenergy.com/innovative-solutions/tidal-energy/oceade-tidal-turbine-platform.html, [Last accessed: 03 Apr 2017].

[24] Renewable Energy News, "GE throws in tidal towel". [Online] http://renews.biz/105467/ge-throws-in-tidal-towel/, [Last accessed: 03 Apr 2017].

[25] EMEC, "Voith Hydro". [Online] http://www.emec.org.uk/about-us/our-tidal-clients/voith-hydro/, [Last accessed: 03 Apr 2020].

[26] S. Djebarri, J. F. Charpentier, F. Scuiller, and M. Benbouzid, "Comparison of direct-drive pm generators for tidal turbines," in *2014 International Power Electronics and Application Conference and Exposition*. IEEE, 2014, pp. 474–479.

[27] EMEC, "Open Hydro". [Online] http://www.emec.org.uk/about-us/our-tidal-clients/open-hydro/, [Last accessed: 28 Sep 2020].

[28] Ø. Krøvel, R. Nilssen, S. Skaar, E. Løvli, and N. Sandoy, "Design of an integrated 100kw permanent magnet synchronous machine in a prototype thruster for ship propulsion," *CD Rom Proceedings of ICEM*, pp. 117–118, 2004.

[29] Tocardo Tidal Power, "History of Tocardo". [Online] http://www.tocardo.com/about/history/, [Last accessed: 03 May 2020].

[30] TOCARDO Tidal Power, "DNV GL issues Statement of Feasibility to Tocardo T2s turbine". [Online] http://www.tocardo.com/dnv/, [Last accessed: 22 Feb 2017].

[31] The European Marine Energy Centre Ltd., "TOCARDO". [Online] http://www.emec.org.uk/about-us/our-tidal-clients/tocardo/, [Last accessed: 02 Apr 2017].

[32] C. hee Jo, J. young Yim, K. hee Lee, and Y. ho Rho, "Performance of horizontal axis tidal current turbine by blade configuration," *Renewable Energy*, vol. 42, pp. 195–206, 2012.

[33] Z. Zhou, F. Scuiller, J. F. Charpentier, M. E. H. Benbouzid, and T. Tang, "Power control of a nonpitchable pmsg-based marine current turbine at overrated current speed with flux-weakening strategy," *IEEE Journal of Oceanic Engineering*, vol. 40, no. 3, pp. 536–545, 2015.

[34] B. Whitby and C. E. Ugalde-Loo, "Performance of pitch and stall regulated tidal stream turbines," *IEEE Transactions on Sustainable Energy*, vol. 5, no. 1, pp. 64–72, 2014.

[35] Schottel Hydro, "SIT Instream Turbine". [Online] https://www.schottel.de/fr/schottel-hydro/sit-instream-turbine/, [Last accessed: 22 Feb 2017].

[36] ALSTOM, “Alstom intends to acquire Tidal Generation Ltd from Rolls-Royce”. [Online] http://www.alstom.com/press-centre/2012/10/alstom-intends-to-acquire-tidal-generation-ltd-from-rolls-royce/, [Last accessed: 03 Apr 2017].

[37] T. Delorm, D. Zappala, and P. Tavner, “Tidal stream device reliability comparison models,” *Proceedings of the Institution of Mechanical Engineers, Part O: Journal of Risk and Reliability*, vol. 226, no. 1, pp. 6–17, 2012.

[38] R. J. Wood, A. S. Bahaj, S. R. Turnock, L. Wang, and M. Evans, “Tribological design constraints of marine renewable energy systems,” *Philosophical Transactions of the Royal Society of London A: Mathematical, Physical and Engineering Sciences*, vol. 368, no. 1929, pp. 4807–4827, 2010.

[39] P. Scheijgrond, “TKI Wind op Zee, Dutch Wave & Tidal energy sector, Status, challenges and roadmap”. [Online] http://www.tki-windopzee.nl/files/2015-10/20150911-rap-dutch.wave.and.tidal.energy.sector-met-f.pdf, [Last accessed: 08 Apr 2017].

[40] Bluewater, “ Texel: BlueTEC Modular Demo”. [Online] http://www.bluewater.com/new-energy/texel-project/, [Last accessed: 10 Feb 2020].

[41] Schottel Hydro, “ BlueTEC platform with SIT.” [Online] https://www.schottel.de/fr/schottel-hydro/sit-instream-turbine/references/, [Last accessed: 10 Feb 2020].

[42] Tocardo International BV, “TOCARDO Tidal Power”. [Online] http://www.tocardo.com/solutions/offshore/, [Last accessed: 22 Apr2020].

[43] Sustainable Marine Energy Ltd, “ Tidal Energy Turbine Platform Technology”. [Online] http://sustainablemarine.com/technology, [Last accessed: 08 Apr 2017].

[44] Farinia Group, “Cast Iron Ballast for Gravity-Based Tripod Foundations”. [Online] http://www.farinia.com/energy/tidal-turbine-counterweights/cast-iron-ballast-for-gravity-foundations, [Last accessed: 08 Apr 2017].

[45] H. Polinder, “Overview of and trends in wind turbine generator systems,” in *Power and Energy Society General Meeting, 2011 IEEE*. IEEE, 2011, pp. 1–8.

[46] S. Benelghali, M. Benbouzid, and J. F. Charpentier, “Comparison of pmsg and dfig for marine current turbine applications,” in *Electrical Machines (ICEM), 2010 XIX International Conference on*. IEEE, 2010, pp. 1–6.

[47] M. Dubois, H. Polinder, and J. Ferreira, “Comparison of generator topologies for direct-drive wind turbines,” *Proceedings of the 2000 NORPIE*, pp. 22–26, 2000.

[48] M. Lehr, K. Reis and A. Binder, “Comparison of axial flux and radial flux machines for the use in wheel hub drives,” *e & i Elektrotechnik und Informationstechnik*, pp. 22–26, 2000. *e & i Elektrotechnik und Informationstechnik*, vol. 132, no. 1, pp. 25–32, 2015.

@phdthesiszhang2015optimization, title=Optimization design and control strategies of a double stator permanent magnet generator for tidal current energy application, author=Zhang, Jian, year=2015

[49] J. Zhang, “Optimization design and control strategies of a double stator permanent magnet generator for tidal current energy application,“ *Ph.D. Dissertation*, Ecole Polytechnique de l’Universit´e de Nantes, Laboratory IREENA, France, 2015.

[50] S. Djebarri, J. F. Charpentier, F. Scuiller, and M. Benbouzid, “Reliability comparison of wind turbines with dfig and pmg drive trains,” *IEEE Transactions on Energy Conversion*, vol. 41, no. 1, pp. 50–66, 2015.

[51] J. Carroll, A. McDonald, and D. McMillan, “Reliability comparison of wind turbines with dfig and pmg drive trains,” *IEEE Transactions on Energy Conversion*, vol. 30, no. 2, pp. 663–670, 2015.

[52] Atlantis Resources, “Meygen project deveopment & operation”. [Online] http://www.atlantisresourcesltd.com/projects/meygen/, [Last accessed: 11 Jan 2017].

[53] European Commission, SET Plan – Declaration of Intent on Strategic Targets in the context of an Initiative for Global Leadership in Ocean Energy, 2016. [Online] https://setis.ec.europa.eu/system/files/integrated_set-plan/declaration_of_intent_ocean_0.pdf [Last accessed: 31 Jan 2020]

[54] D. Magagna, R. Monfardini and A. Uihlein, “Ocean energy in Europe: assessing support instruments and cost-reduction needs,” in *International Marine Energy Journal*, vol. 1, no. 1, 2018.

[55] D. Magagna, L. Margheritini, A. Alessi, E. Bannon, E. Boelman, D. Bould, V. Coy, E. De Marchi, P. Frigaard, C. Guedes Soares, C. Golightly, J. Hals Todalshaug, M. Heward, M. Hofmann, B. Holmes, C. Johnstone, Y. Kamizuru, T. Lewis, L. Macadre, C. Maisondieu, M. Martini, A. Moro, K. Nielsen, V. Reis, S. Robertson, P. Schild, M. Soede, N. Taylor, I. Viola, N. Wallet, X. Wadbled and B. Yeats, “Workshop on identification of future emerging technologies in the ocean energy sector - 27th March 2018, Ispra, Italy,” EUR 29315 EN, European Commission, Luxembourg, 2018, ISBN 978-92-79-92587-0, DOI:10.2760/23207, JRC112635

[56] Ocean Energy: Key trends and statistics 2018 . [Online]. https://www.oceanenergy-europe.eu/wp-content/uploads/2019/04/Ocean-Energy-Europe-Key-trends-and-statistics-2018_web.pdf [Last accessed: 03 Feb 2020].

[57] D. Coles, T. Walsh, “Mechanisms for reducing the cost of tidal stream energy,” in *Proceedings of the 13th European wave and tidal energy conference (EWTEC)*, Napoli, Italy, 2019.

[58] MEYGEN, “The Project-Environmental Impact Assessment”. [Online] http://www.meygen.com/the-project/, [Last accessed: 08 Apr 2017].

[59] A. Harnoy. Bearing design in machinery: engineering tribology and lubrication. CRC press; 2002.

[60] H. Towsyfyan, F. Gu and A. Ball. A review of mechanical seals tribology and condition monitoring. University of Huddersfield. [Online] http://eprints.hud.ac.uk/id/eprint/19391/2/towsyfyan.pdf [Last accessed: 05 Sep 2019].

[61] S. Djebarri, J. F. Charpentier, F. Scuiller, M. Benbouzid and S. Guemard, "Rough Design of a Double-Stator Axial Flux Permanent Magnet Generator for a Rim-driven Marine Current Turbine", in *2012 IEEE International Symposium on Industrial Electronics*, IEEE, 2012 (pp. 1450-1455).

[62] J. S. Carlton, "Podded Propulsors: Some Results of Recent Research and Full Scale Experience", in *Journal of Marine Engineering & Technology*, vol. 7, no. 1, 2008, pp. 1-4.

[63] C. Scott. Considerations for a Canned Motor Pump. World Pumps. 2004 Dec 1;2004(459):22-5.[Online] https://www.sciencedirect.com/science/article/pii/S0262176204004195 [Last accessed: 23 May 2019].

[64] L. Drouen, J. F. Charpentier, E. Semail, S. Clenet. Study of an Innovative Electrical Machine Fitted to Marine Current Turbines. In OCEANS 2007-Europe 2007 Jun 18 (pp. 1-6). IEEE.

[65] N. Baker, S. Cawthorne, E. Hodge, and E. Spooner, “3D Modelling of the generator for OpenHydro’s tidal energy system,” in *7th IET International Conference on Power Electronics, Machines and Drives (PEMD 2014)*. IET, 2014, pp. 1–6.

[66] B. R. Lipe, C. R. Webb, inventors; Allis-Chalmers Corp, assignee. Canned motor. United States patent US 2,958,292. 1960.

[67] B. Holstein, N. Perner, inventors; Voith Patent GmbH, assignee. Submersible power generating plant, driven by a water flow. United States patent US 8,410,626. 2013.

CHAPTER 3

A Study on Passive Cooling in Subsea Power Electronics

In the previous chapters reliability of power electronic converter was highlighted as critical in terms of reducing the levelized cost of energy in tidal turbines. Thermal cycling has been identified as one of the main failure modes in power converters. This chapter is the first of the series of three chapters to deal with thermal cycling in tidal turbine converters. In this chapter a thermal model for semiconductor power modules in submerged power electronic converter is presented. The converter is cooled passively (i.e. by natural convection) by ambient sea water.

Also published as:
F. Wani, U. Shipurkar, J. Dong and H. Polinder, "A Study on Passive Cooling in Subsea Power Electronics," in *IEEE Access*, vol. 6, pp. 67543–67554, 2018.

Abstract

This chapter proposes a simplified approach to model the thermal behavior of the insulated gate bipolar transistors (IGBTs) in a subsea power electronic converter. The models are based on empirical relations for natural convection in water and the IGBT datasheet values. The proposed model can be used in the design of subsea converters and in the reliability analysis of their IGBTs. Experimental results are provided to validate the proposed thermal model. Suggestions are made to minimize the net thermal resistance by introducing a high conductivity thermal material as a mounting plate between the IGBT and the cabinet walls. Impact of the mounting plate dimensions, and material properties on the junction temperature of the IGBTs is studied. A case study analysis is made on a 100 kVA converter. Results indicate that the thermal spreading resistances in the mounting plate and the cabinet walls contribute significantly to the overall thermal resistance. Spreading resistances can be mitigated by appropriate design measures. Furthermore, it was observed that the passive cooling in water is not as effective as the forced water cooling. However, low cost, simple design and higher reliability of passive cooling systems might make them a favorable choice for subsea systems.

3.1 Introduction

A major cause of failure in power electronic converters is the thermally induced stress on semiconductor switches or insulated gate bipolar transistors (IGBTs) [1–3]. These failure mechanisms can be mitigated by minimizing the mean junction temperature and the temperature cycling in IGBTs [1–5]. An easy way of doing this is to use forced air or liquid-cooled systems. However, any failure in the cooling system—such as fan/pump malfunction or leakage of the coolant—contribute to the premature failure of the IGBTs [6]. Therefore, periodic maintenance of the cooling system is necessary to minimize downtime and maintenance expenses. As a result, easy access to power electronic systems is favored.

Subsea power electronic converters are required in many applications, such as in oil and gas industry and ocean renewables. For example, a tidal turbine drive train, shown in Figure 3.1, normally uses a simple two-level back-to-back voltage source converter (VSC) with IGBTs to control the generator speed (or torque) and maintain the active and/or reactive power balance with the grid. For submerged converters, unforeseen maintenance exercises can be expensive and result in long downtimes. Furthermore, sea water is conductive as well as corrosive; and deployment at significant depths also imposes pressure restrictions. These factors usually increase the failure rates and, consequently, equipment design and ensuring reliability is more challenging [7]. Accordingly, most offshore players prefer placing converters onshore, on floating platforms on sea surface or seabed-mounted platforms above the sea surface [8, 9]. Such topologies allow easy access to converters; albeit this comes with increased costs and complexity related to cabling, mooring and platforms, etc.

On the other hand, subsea or seabed-mounted converters do not require long and complicated

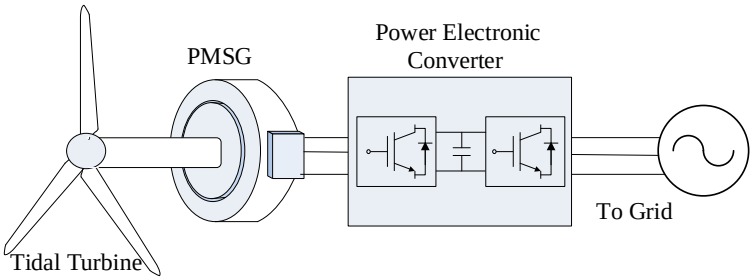

Figure 3.1 Tidal turbine drive train with a direct-drive permanent magnet synchronous generator (PMSG) and a power electronic (PE) converter.

cabling or mooring systems, and are also out of view. Besides it potentially makes the control of drives an easier task [10–12]. Moreover, sea water provides a heat sink of practically infinite heat capacity. With proper design, passive cooling may prove a more reliable and an inexpensive cooling solution [13]. A simple passive cooling topology for the subsea converter is shown in Figure 3.2. Here, the IGBT module is mounted on a plate bolted to the enclosure wall.

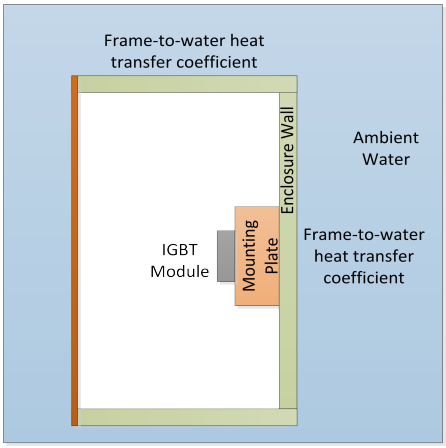

Figure 3.2 A representation of an IGBT module mounted inside a submerged enclosure.

The objective of this chapter is to develop a thermal model capable of predicting the dynamic junction temperature of the IGBTs inside a hermetically sealed subsea enclosure. The cooling effect is assumed to be entirely due to the buoyancy-driven flow outside the enclosure. Furthermore, we identify the critical parameters that influence the passive cooling characteristics, and suggest measures to improve cooling. The developed model is then applied to predict the junction temperature cycling in a 100 kVA tidal turbine power converter. However, for model validation purpose only a small-scale experimental setup was designed.

In this thesis we have neglected the additional potential cooling effect of the tidal stream flow around the converter cabinet. This was done because the flow around the converter cabinet would significantly depend on the placement of the converter cabinet with respect to the turbine, and hence the additional cooling due to water flow is difficult to quantify. Therefore, as a worst case scenario, we assumed that the ambient water is stationary, and only 'buoyancy-driven flows' were considered.

Therefore, the primary contribution of this chapter is the development of a fast analytical thermal model for subsea power electronics and the use of this model in the analysis of passive cooling in subsea power converterss; this is not a widely studied problem in literature. A secondary contribution is the investigation of the parameters that influence the passive cooling. This serves as a good starting point for the design of subsea converters.

The next section revisits the relevant literature on the cooling of power electronics. Section 3.3 illustrates the thermal modeling of the IGBTs and the mounting plate in the subsea converter. Section 3.4 explains the calculation of the external heat transfer coefficient using empirical relations. Section 3.5 highlights the utility of stationary computational fluid dynamics (CFD) simulations in calculating the heat transfer coefficient. Experimental validation of the thermal models on the scaled-down system is demonstrated in Section 3.6. In Section 3.7, the thermal models are extended to a 100 kVA converter, where a detailed analysis follows on the critical parameters and other aspects of passive cooling. Section 3.8 summarizes the conclusions drawn from this study, and provides suggestions for future work.

3.2 Literature review

Thermal models are necessary for appropriate selection of IGBTs and the design of their cooling systems. They are also vital for pre and post-manufacturing reliability studies of IGBTs [4, 14, 15]. Forced liquid cooling systems in power electronic converters have been thoroughly investigated in the literature [4, 16–20], and are in common use in many industries. However, passive cooling of the submerged power electronics is not as thoroughly investigated. This is primarily due to fewer subsea applications, and the aforementioned reasons to avoid subsea placement of power electronics.

In a passively cooled subsea system shown in Figure 3.2, mainly two modes of heat transfer occur from the IGBT to the enclosure walls: (1) the fluid inside the enclosure undergoes convection (natural or forced) transferring heat to the walls; and (2) direct conduction between the heat source and the enclosure walls. In case the IGBT (or heat source) is mounted on a thermally conductive material attached to the wall and the internal medium is air, the bulk of the heat transfer is via the latter mode. The final heat transfer from the enclosure wall to the sea water is by natural convection.

Estimating the flow properties of naturally convecting fluid inside a sealed enclosure is a difficult task. Unlike forced air or liquid-cooled systems, the coolant does not perpetually enter the system at a constant temperature. As a result numerical techniques such as CFD are used. For instance,

Zhang et al. [21] analyzed and experimentally verified the temperature distribution inside a high power density sealed flyback adapter using the Flotherm (a commercial CFD package) software. Although computationally expensive, this is by far the most reliable method of estimating the temperature distribution inside a sealed enclosure, whenever internal convection dominates.

Analytical models too have been developed for thermal modeling of electronics inside a sealed enclosure. However, these models make various simplifying assumptions, which may not hold true in many cases. For example, Teertstra et al. [22] modeled the natural convection inside a enclosure with isothermal walls, enclosing a vertical isothermal plate. In this thesis, we neglect the heat transfer inside the box by natural convection.

In [23], a cold plate based sea water cooling of power electronics in leisure vessels is proposed. The model considers using filtered sea water as a coolant, whose flow rate in the heat sink channels is determined by the velocity of the vessel. In [24, 25], sea water is pumped and used as a secondary coolant to cool the fresh water used in central cooling systems of ships. All these systems use sea water in a forced cooling mechanism either directly or indirectly. These models do not analyze cooling systems dependent on natural convection.

Vu Xuan et al. [26] consider the cold plate based natural cooling and forced water cooling in maritime generators. They conclude that generators cooled passively should be under-rated by almost 40-50% compared to forced cooled generators. This highlights the constraints of relying on natural convection alone.

Kang [27] and Schulz-Harder [28] reviewed the advanced and highly integrated cooling solutions for power electronic devices in their work. The focus is mainly on forced air and liquid cooling systems. Two-phase cooling and air cooled loop thermosiphon techniques have also been mentioned. However, passive cooling in water is hardly discussed.

Natural convection in vertical channels with asymmetrical heating is addressed in [29]. The authors studied the effect of placing an auxiliary adiabatic plate in the channel on the mass flow rate and heat transfer coefficient. However, only laminar flow regime was investigated and the solution is computed by CFD. Bhowmik and Tou [13] made an experimental analysis on transient natural convection of electronic chips, cooled by water in a vertical up-flow channel driven by buoyancy. In their study, they analyzed the local Nusselt numbers and heat transfer coefficients, and found that the experimental results closely agreed with the available literature on similar geometries. However, they did not consider the impact of spreading resistance in the wall or model the chip temperature.

From above discussion it is clear that passive cooling in submerged electronics is a little investigated problem. Moreover, localized heat sources and thermal spreading resistances in power electronics pose additional complexities in the models. Besides, most of the relevant work seems to rely extensively on CFD simulations. This chapter addresses these issues by proposing an approximate (and fast) analytical thermal model.

3.3 Thermal models for IGBT modules and mounting plate

The power converter in Figure 3.1 is placed inside a hermetically sealed enclosure. This enclosure could mean a nacelle enclosing a generator as well or a stand-alone enclosure dedicated to the power converter and other electronic systems. The enclosure must be made of a non-corrosive and thermally conductive material such as stainless steel.

Referring to Figure 3.2, all the heat from the IGBT module is assumed to transfer to the enclosure walls via the mounting plate. Better cooling maybe provided by installing a fan inside the enclosure; however, we do not consider that here. The bulk of the heat transfer in either case is expected to be via the mounting plate to the walls.

Three main thermal barriers exist between the IGBT junction and the ambient water. These are: IGBT junction-to-case, case-to-external wall (including mounting plate and enclosure wall), and wall-to-ambient water thermal resistances. A lumped element thermal network for such a system is shown in Figure 3.3. Between these elements, a thin layer of the thermal paste is also usually present, which must be included in the thermal model.

3.3.1 Cauer and Foster network models for IGBT

In Figure 3.3, the IGBT module is represented by a 1-layer Cauer network [30, 31]. Normally, datasheets of IGBT provide the junction-to-case thermal characteristics in the form of multilayer (usually 4) Foster network. However, Foster networks cannot be directly coupled to the mounting plate or heatsink Foster/Cauer networks. On the other hand, using a multilayer Cauer network results in over-filtering of the temperature fluctuations, and thus inaccurate junction temperature estimation [30]. For this reason, we use the two-part combined Foster-Cauer thermal network model as adopted in [4, 30, 31].

3.3.2 Mounting plate

The IGBT shall normally be placed on a mounting plate made of a thermally conductive material to facilitate the heat transfer to the enclosure wall. The dimensions of the mounting plate and the material has an influence on the thermal resistance; this will be shown later in the chapter.

The spreading resistance is a crucial component of the total thermal impedance. IGBT acts as a localized heat source on a wider mounting plate. The thermal spreading resistance in the mounting plate also needs to be calculated, in addition to the conventional one-dimensional thermal resistance.

Muzychka et al. [32] provide a good description of the thermal spreading resistance in rectangular channels. For the system shown in Figure 3.4 and Figure 3.5, the spreading resistance is given by

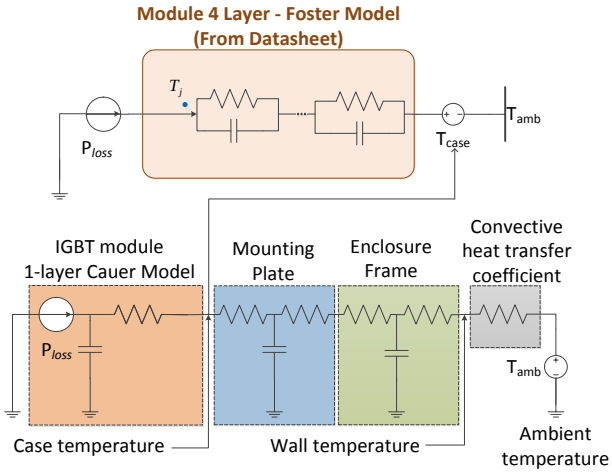

Figure 3.3 Lumped element thermal network model for the system shown in Figure 3.2.

[32][1]:

$$R_s = \frac{1}{2a^2cdk_1}\sum_{m=1}^{\infty}\frac{sin^2(a\delta_m)}{\delta_m^3}\phi(\delta_m) + \frac{1}{2b^2cdk_1}\sum_{n=1}^{\infty}\frac{sin^2(b\lambda_n)}{\lambda_n^3}\phi(\lambda_n) + \frac{1}{a^2b^2cdk_1}\sum_{m=1}^{\infty}\sum_{n=1}^{\infty}\frac{sin^2(a\delta_m)sin^2(b\lambda_n)}{\delta_m^2\lambda_n^2\beta_{m,n}}\phi(\beta_{m,n}), \tag{3.1}$$

where parameters a, b, c and d are defined in Figure 3.4; k_1 is the thermal conductivity of the mounting plate.
And,

$$\begin{aligned}\delta_m &= \frac{m\pi}{c}\\ \lambda_n &= \frac{n\pi}{d} \quad \text{, and}\\ \beta_{m,n} &= \sqrt{\delta_m^2+\lambda_n^2}\end{aligned} \tag{3.2}$$

$$\phi(\zeta) = \frac{(e^{2\zeta t}+1)\zeta - (1-e^{2\zeta t})h/k_1}{(e^{2\zeta t}-1)\zeta + (1+e^{2\zeta t})h/k_1}, \tag{3.3}$$

where h is the heat transfer coefficient at the outer edge of the mounting plate. The lateral faces of the mounting plate are assumed to be adiabatic.

[1] The analytical results used from this paper were verified with finite element simulations before being used here. This verification is not demonstrated here.

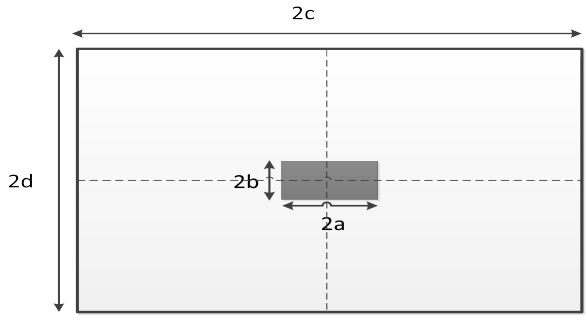

Figure 3.4 Top view of the IGBT mounted on a thermally conducting mounting plate. Image is adapted from [32]

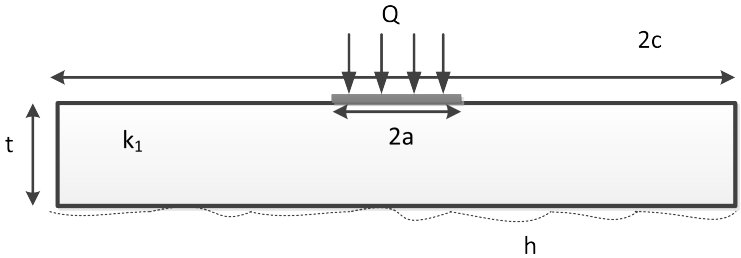

Figure 3.5 Side view of the IGBT mounted on a thermally conducting mounting plate. Image is adapted from [32].

For two layers of the base plate material, as shown in Figure 3.6, the spreading resistance is calculated using the same formulae, however with the following modification [32][2]:

$$\phi(\zeta) = \frac{(\alpha e^{4\zeta t_1} + e^{2\zeta t_1}) + \varrho(e^{2\zeta(2t_1+t_2)} + \alpha e^{2\zeta(t_1+t_2)})}{(\alpha e^{4\zeta t_1} - e^{2\zeta t_1}) + \varrho(e^{2\zeta(2t_1+t_2)} - \alpha e^{2\zeta(t_1+t_2)})} \tag{3.4}$$

where,

$$\begin{aligned} \varrho &= \frac{\zeta + h/k_2}{\zeta - h/k_2} \\ \alpha &= \frac{1 - k_2/k_1}{1 + k_2/k_1} \ . \end{aligned} \tag{3.5}$$

To account for the thermal resistance of the wall, the parameter, h in (3) and (5) is calculated as follows:

$$\frac{1}{h} = A_{mp}\Big(\frac{1}{h_{ext}\ A_{wall}} + \frac{t_{wall}}{k_{wall}\ A_{wall}} + R_{spread,wall} + \frac{t_{tp}}{k_{tp}\ A_{mp}}\Big). \tag{3.6}$$

[2]The parameterized values for the spreading resistance can also be obtained for multiple (and non-centrally placed) sources mounted on the same mounting plate using the same methodology as described in [32].

Here, A_{mp} and A_{wall} denote the areas of the mounting plate and external wall exposed to the sea water. t_{wall} and t_{tp} represent the thickness of the enclosure wall and the thermal paste respectively; whereas, k_{wall} and k_{tp} denote their respective thermal conductivity. $R_{spread,wall}$ denotes the thermal spreading resistance in the wall, and h_{ext} is the external heat transfer coefficient.

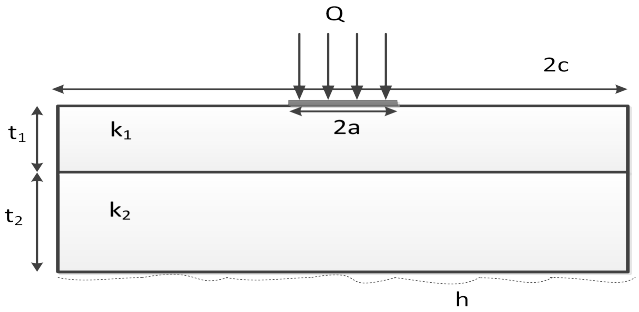

Figure 3.6 IGBT mounted on a thermally conducting base plate made of 2 different layers and/or materials. Image is partially adapted from [32].

The additional thermal spreading resistance in the wall can also be obtained from expressions (3.1) - (3.3), with appropriate modifications, as explained in [32]. However, in this case the heat does not spread to the entire wall and careful estimation of the spreading area needs to be made. This point is further explained in the next sections, where the calculation of heat transfer coefficient is explained.

3.4 Estimating heat transfer coefficient to ambient sea water

The heat transfer from the enclosure walls to the ambient water in this case is assumed to be entirely by natural convection. The thermal resistance due to convection is given by,

$$R_{th,conv} = \frac{1}{h_{ext} A_s}, \tag{3.7}$$

where h_{ext} is the averaged heat transfer coefficient for the surface area of A_s.

An easy way to estimate the heat transfer coefficient from enclosure wall to the surrounding sea water is by using the empirical relations found in literature [33–35]. For modeling the heat transfer due to natural convection, a set of important dimensionless numbers determining the fluid flow regime need to be calculated. These include Grashof number (Gr), Prandtl number (Pr), Rayleigh number (Ra_L) and the Nusselt number (Nu).

For a vertical wall at a temperature T_s, in an ambient fluid of temperature T_∞ at a remote distance

from the wall, we have [33]:

$$\begin{aligned} Gr &= \frac{g\beta(T_s - T_\infty)L^3}{\nu^2} \\ Pr &= \frac{\mu c_p}{k} \\ Ra_L &= Gr\,Pr, \end{aligned} \tag{3.8}$$

$$Nu_{T_s} = \left\{0.825 + \frac{0.387 Ra_L^{1/6}}{[1 + (0.492/Pr)^{9/16}]^{8/27}}\right\}^2, \tag{3.9}$$

$$h_m = \frac{Nu\,k}{L}, \tag{3.10}$$

where g is the acceleration due to gravity (m/s^2), L is the vertical length of the wall (m), ν is the kinematic viscosity of water (m^2/s), μ is the dynamic viscosity of water (N·s/m^2), c_p is the specific heat capacity of water (J/kg·K) and k is the thermal conductivity of water (W/m·K).

In our case, T_s is treated as the mid-point temperature of the wall, and h_m as the mid-point heat transfer coefficient.

The caveat with using the above equations is that the wall temperature T_s must be known a priori. However, we can only know the loss from the IGBT, and not the enclosure wall temperature beforehand; see Figure 3.7. To circumvent this problem the following approach is adopted here, as suggested in [33] :

1. Assume a certain T_s, and calculate Nu_{T_s} using (3.8) and (3.9).
2. For a known value of $\dot{q}_s$, calculate the Nu_{q_s} using the relation,

$$Nu_{q_s} = \frac{\dot{q}_s L}{k[T_s - T_\infty]}\ . \tag{3.11}$$

3. Iterate T_s value over the previous two steps until $Nu_{T_s} = Nu_{q_s}$.
4. Use (3.10) to calculate h_m from the converged value of Nu.

The averaged heat transfer coefficient at the vertical edges of the mounting plate can be assumed to be zero, if the heat flux at those edges is taken to be zero. Then the following relation can be assumed:

$$h_{ext} = \frac{h_m}{2}\left(\frac{b_{mp} + b_{hs}}{b_{mp}}\right), \tag{3.12}$$

where b_{mp} and b_{hs} denote the horizontal widths of the mounting plate and the heat source respectively. This value of h is used in (3.6) and (3.7).

However, there is another problem with the above formulation: the equivalent wall length, L is unknown. Since the heat source is concentrated on the inside of the wall, using the full enclosure wall height as L in (3.8) and (3.10) does not seem to be a reasonable approximation. Furthermore, heat from the mounting plate will also not spread equally in vertical direction due to upward flow near the wall. Therefore, determining L becomes critical to the thermal model. Preemptive calculation of L can be done by using CFD, as illustrated in the next section.

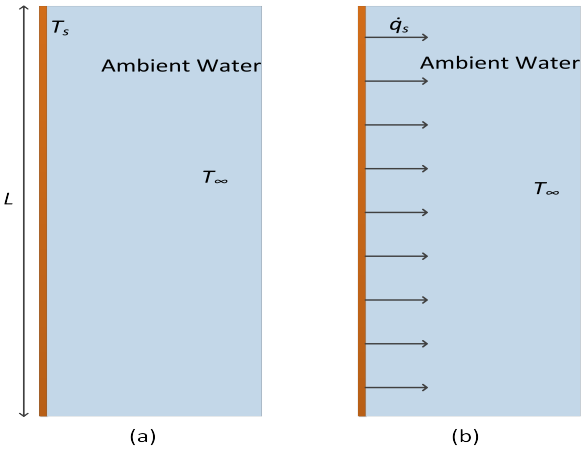

Figure 3.7 A vertical plate exposed to a fluid (a) plate is isothermal; (b) constant heat flux from plate.

3.5 Obtaining equivalent wall length from CFD

Strictly speaking, heat transfer from the IGBT to the sea water is a 3D conjugate heat transfer problem. CFD simulations can be used to estimate the junction temperature in IGBT modules inside a submerged converter enclosure. However, such models can be extremely time and resource consuming, and are thus avoided as much as possible.

In this thesis, CFD simulations are merely used to estimate the equivalent wall length for heat transfer calculations. Using this information, analytical models based on empirical relations can be used for thermal modeling purposes.

The assumptions and the governing equations for the CFD model of this system are given below.

3.5.1 Assumptions

– Boussinesq approximation: In the governing Navier-Stokes equations, mass density is assumed to be constant except in the buoyancy term. Continuity equation is thus used in its incompressible form. The Boussinesq approximation can be applied under the following condition [36]:

$$\beta(T - T_0) \ll 1, \tag{3.13}$$

where β is the thermal expansion coefficient (1/K) , T is the fluid temperature (K), and T_0 is the reference or the operating temperature (K).
A detailed and mathematically rigorous inspection of whether or not the Boussinesq approximation is valid under certain conditions is given in [36, 37].

– No additional heat loss to the sea by radiation has been assumed.

Table 3.1 Constants and Material Parameters

Parameter	Value
Thermal conductivity of Al	170 W/m·K
Thermal conductivity of Cu	400 W/m·K
Thermal conductivity of Stainless steel 304L	15 W/m·K
Thermal conductivity of water	0.6 W/m·K
Thermal conductivity of thermal paste	0.67 W/m·K
Density of water	998 kg/m^3
Density of Al	2700 kg/m^3
Density of Cu	8960 kg/m^3
Density of Stainless steel 304L	7850 kg/m^3
Specific heat capacity of Al	870 J/kg·K
Specific heat capacity of Cu	385 J/kg·K
Specific heat capacity 304L	475 J/kg·K

– The vertical variation of the heat transfer coefficient derived from 2D CFD modeling is assumed to have similar variation throughout the width of the mounting plate in the horizontal direction. This assumption was made to avoid 3D simulations.

3.5.2 Governing equations and boundary conditions

The governing differential equations are presented below after applying the Boussinesq approximation.

$$\nabla \cdot \mathbf{U} = 0 \tag{3.14}$$

$$(\mathbf{U} \cdot \nabla)\mathbf{U} = \nu \nabla^2 \mathbf{U} - \frac{1}{\rho}\nabla P - g\alpha \Delta T \tag{3.15}$$

$$\mathbf{U} \cdot \nabla T = \kappa \nabla^2 T\,, \tag{3.16}$$

where, $\mathbf{U}$ is the velocity vector, ν is the kinematic viscosity of water, ρ is the density, P is the pressure, α is the thermal expansion coefficient, T is the temperature, and κ is the thermal diffusivity. Other constants and the material parameters used in the CFD modeling are listed in Table 3.1.

In addition to the above conservation equations, a turbulence model is required to obtain a solution to the heat transfer problem. In this thesis we use the $k-\epsilon$ model, which is common in such type of problems [38]. The boundary conditions used at far distance from the box in the sea are the pressure inlet and outlet conditions, at ambient temperatures. ANSYS Fluent was used for CFD simulations, with default parameters for $k-\epsilon$ model.

3.5.3 CFD results

From Figure 3.8, it is clear that the heat loss mainly happens only along a part of the vertical wall, and not along the entire wall. The wall length across which the bulk heat transfer can be obtained as shown in Figure 3.9. This wall length is used in equations (3.8) - (3.11).

However, 2D CFD calculations will only give the spreading area in vertical direction. In horizontal direction, the spread can be assumed to be limited to the base plate area owing to the vertical nature of buoyancy-driven flows. The spread of the heat flux may also be assumed to be similar in the horizontal direction as in the vertical direction.

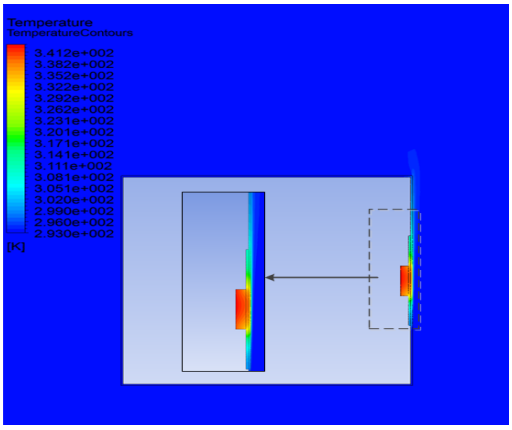

Figure 3.8 Temperature distribution inside the power electronic enclosure.

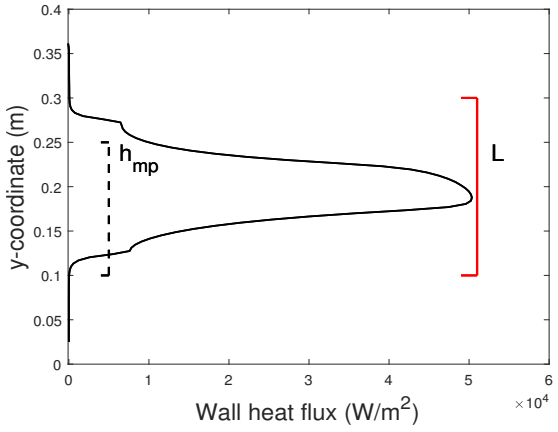

Figure 3.9 Wall heat flux from the vertical wall of the box. Equivalent wall length can be obtained from this figure. h_{mp} denotes the vertical length of the mounting plate.

3.6 Experimental validation

Validating the thermal models for the IGBTs rated near the 100 kW level was infeasible in the available laboratory setup. Therefore, a scaled-down experimental setup was installed to validate the aforementioned thermal model. In the experiments, normal tap water was used instead of the sea water. Although the models were validated only at low power levels, it is expected that they will be applicable even at higher power levels and larger system dimensions. The power density in the experimental setup was chosen to be around the same value as for the 100 kVA converter.

There is a general consensus on thermal modeling of IGBTs, as mentioned in Section 3.3. The main challenge for submerged power electronics is to estimate the case temperature. For this reason, case or mounting plate temperature is the main focus of the experimental validation.

3.6.1 Experimental setup

For constant loss in the IGBT, the IGBT can be replaced by any appropriate heat source. A 4.7 Ω resistor was used for this purpose. This was done to generate significant loss on the mounting plate. Commercial IGBTs do not generate such level of loss at low currents and voltages. On the other hand, a simple resistor can easily generate losses upto 60 W from currents less than 4 A, which requires a smaller power supply. The resistor was mounted on an aluminum plate which was then bolted on the enclosure wall. The contact resistance was minimized by applying a thermal paste. The dimensions of the materials used in the experimental setup are listed in Table 3.2.

To see the effect of the spreading resistance, an additional Cu plate was inserted between the Al plate and the enclosure wall, and the temperature measurements were repeated. The sensor is placed just above the Al plate by making a small groove, as shown in Figure 3.10.

Table 3.2 Physical Dimensions of the Experimental Setup

Parameter	**Value**
Enclosure wall thickness	0.002 m
Enclosure height	0.350 m
Enclosure width	0.350 m
Enclosure length	0.350 m
Al/Cu Base plate dimensions	0.105 m x 0.150 m
Al Base plate thickness	0.0025 m
Cu Base plate thickness	0.010 m

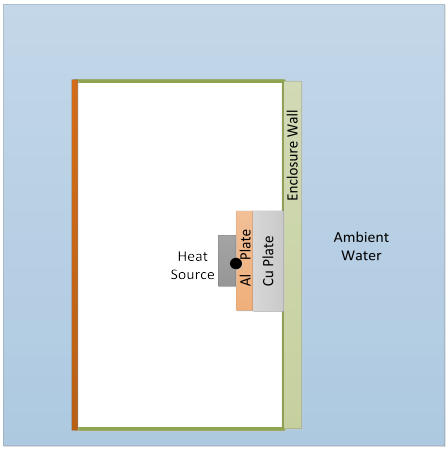

Figure 3.10 Two layers of base plate for mounting of IGBTs. Solid circle represents the thermocouple (temperature sensor) location.

3.6.2 Results

The following results correspond to an ambient temperature of 24 °C. In the first case, the mounting plate is made only of Al; whereas in the second case, a combination of Al and Cu plate is used.

Al mounting plate

Figure 3.11 shows the temperature measured at different points on the wall of the box for different values of losses in the resistor. The thermal heat spread is shown in Figure 3.12. This image also validates the choice of L in (3.10), and shown in Figure 3.9. As seen in Figure 3.11, the temperature on the wall sides barely increases indicating that the bulk heat remains concentrated within the width of the mounting plate, mostly flowing vertically upwards in the direction of the buoyancy-driven water flow. The mid-point wall temperature on the water side also increases as expected with the power loss, indicating isothermal boundary condition on the wall is not a suitable approximation to make under these circumstances.

Figure 3.13 shows the comparison between the temperature calculated from the model and measured from the setup, at the mid-point just below the heat source.

The errors in the calculated value and the measured value ranged between 5-15%, as calculated from the ambient temperature. These errors can arise from:

- tolerance of sensors;
- placement of sensors (not exactly on top of the Al plate, rather in a trough created on its surface);

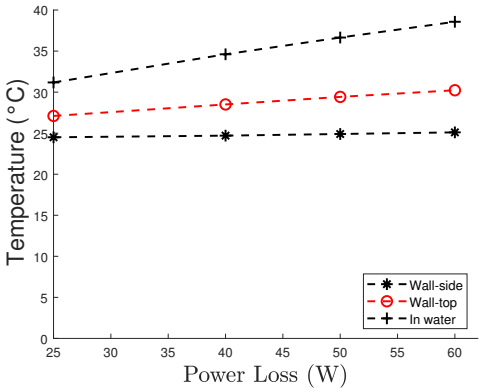

Figure 3.11 Temperatures measured at different points on the wall. 'Wall-side' and 'Wall-top' denote the temperatures at positions shown in Figure 3.12. 'On water side' denotes the temperature on the water side of the wall directly below the heat source.

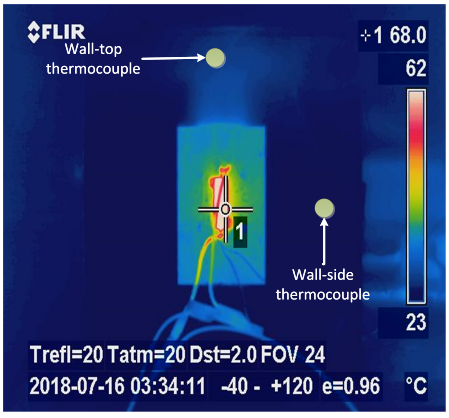

Figure 3.12 Thermal image showing heat spread in aluminum plate and the stainless steel wall. Temperature sensor placement on the walls is also shown by green circles.

– sensor placing also alters the thermal path and hence, affects the thermal resistances; and
– finally, the assumptions made in the modeling, such as neglecting radiation, and less than perfect nature of empirical relations.

Mounting plate made of Al and Cu

The thermal model predicted that the inclusion of the copper layer—in between the enclosure wall and the aluminum plate—should result in the drop of the temperature at Al plate. This was validated by the experimental results, as shown in Figure 3.14. The system is similar to that shown

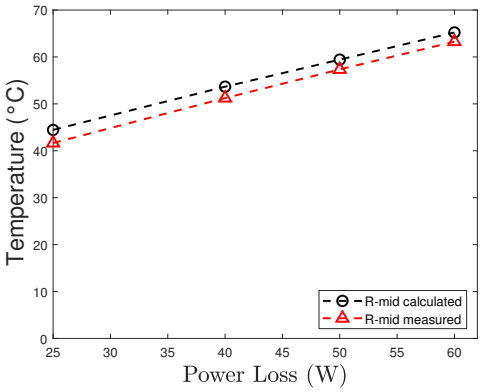

Figure 3.13 Comparison of temperatures between analytical models and measurements below the heat source on the aluminum mounting plate.

in Figure 3.10.

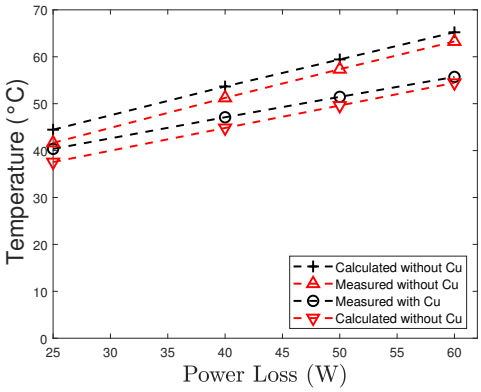

Figure 3.14 Comparison of temperatures between analytical models and measurements below the heat source on the aluminum mounting plate with and without Cu layer.

The effect of Cu layer thickness on the resistor temperature is shown in Figure 3.15, as calculated from the model. The marginal utility of increasing the copper layer thickness decreases with increase in thickness. After a certain optimum thickness (in this case around 25 mm), the drop in the spreading resistance by increasing the thickness is overcome by the increase in resistance due to length (also called 1D resistance).

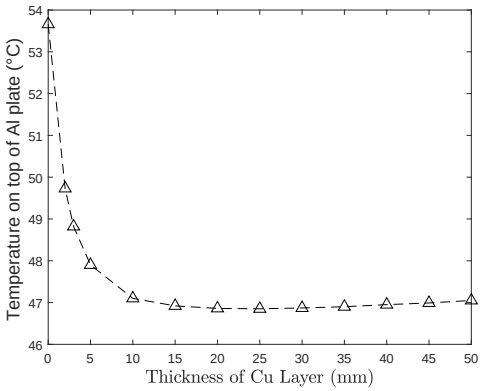

Figure 3.15 Variation of mounting plate temperature with thickness of Cu layer on Al+Cu mounting plate. The loss in the heat source was 40 W.

3.7 Case study: Analysis of a 100 kVA tidal turbine converter

In this section, we extend the thermal model to the passively cooled IGBT for a 100 kVA power electronic converter. The converter is assumed to be a two-level back-to-back VSC, with an efficiency of about 97%. The objective is to analyze the characteristics of passive cooling at a larger scale. And consequently, study the contributions of different thermal resistances to the total thermal resistance seen by the IGBT.

3.7.1 Assumptions

The analysis in this section is based on the following assumptions:

- The individual IGBT modules are mounted on separate but closely placed mounting plates in a horizontal array. Since the heat spreads vertically, each IGBT module can be analyzed individually.
- The loss inside a single IGBT has been modeled as a trapezoidal pulsed waveform. For a 100 kVA turbine, the mean power loss in a phase leg of the converter was roughly assumed to be 600 W.
- The thermal parameters of IGBT module are assumed to be independent of temperature.
- The aspect ratio of the mounting plate is kept same as that of the IGBT. This is by no means necessary or requirement of the model; it is merely adopted to simplify the calculations, and provide an easily imaginable picture.
- The outer walls of the enclosure are flat, and no biofouling/corrosion layer is considered.
- Ambient temperature of the sea water is 20 °C.

Table 3.3 100 kVA Converter Parameters

Parameter	Value
IGBT dimensions	0.057m x 0.110 m
IGBT (junction-to-case) R_{th}	[3.8 31.2 0.1 2.0] K/kW
IGBT (junction-to-case) τ_{th}	[0.0007 0.0247 0.050 3.485] s
Enclosure wall thickness	0.005 m
Enclosure height	1.5 m
Enclosure width	0.5 m
Enclosure length	1.5 m
Cu mounting plate dimensions	0.171 m x 0.330 m
Cu plate thickness	0.010 m
Thermal paste thickness	0.0001 m

The IGBT (Infineon's FF600R12ME4_B11) used for the analysis is rated at 1200 V and 600 A. The 4-layer Foster network thermal impedance parameters for the IGBT are listed in Table 3.3, along with the mounting plate and enclosure dimensions.

As mentioned already, we have assumed a constant power loss in the IGBT for our analysis. Usually, we only know the voltage across and the current in the IGBT. In that case, the IGBT temperature must be used in a feedback loop to calculate the losses.

3.7.2 Results

Figure 3.16 shows the contribution of each thermal resistance component to the overall thermal resistance from the IGBT junction to the ambient sea water. Clearly, the contribution of the spreading resistance to the case-to-ambient thermal resistances is significant.

Suppose that the IGBT is mounted on the copper mounting plate, which is bolted to the enclosure wall. Then for the mounting plate area given in Table 3.3, the effect of the mounting plate thickness on the IGBT junction temperature is shown in Figure 3.17.

Figure 3.18 shows the influence of the area of the mounting plate area and thickness on the mean junction temperature of the IGBT. The factor, d_{mf} in Figure 3.18, denotes the length multiplying factor of the mounting plate w.r.t the IGBT dimensions. For example, if the IGBT module plate area is 0.057 m x 0.110 m, then d_{mf} of 3 implies the mounting plate dimensions are 0.171 m x 0.330 m (i.e. times 3). The plot shows the same trend as in Figure 3.15, although the optimum thickness varies slightly for different values of d_{mf}.

Interestingly, for very small thickness of the mounting plate, increasing the area has opposite effect than at larger thicknesses. A major contributing reason is that the heat transfer coefficient

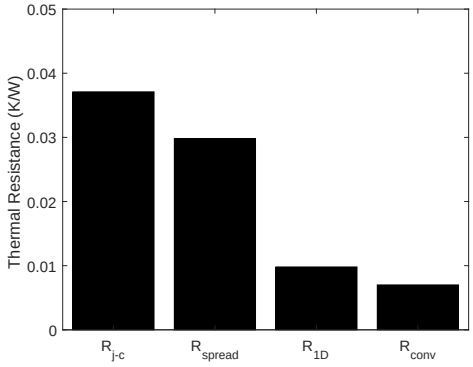

Figure 3.16 Thermal resistance contributions for mean power loss of 300 W in each IGBT on generator side of the converter. Mounting plate is made of Cu and is 30 mm thick.

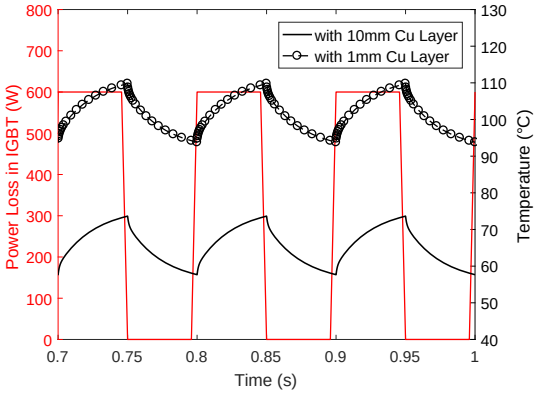

Figure 3.17 IGBT loss and junction temperature (for 100 kVA converter) when mounted on the Cu plate (one switch of a phase-leg).

is higher for lower values of d_{mf} ($h_{d_{mf}=2} > h_{d_{mf}=3} > h_{d_{mf}=4}$ ...). For very small thicknesses, this results in an overall decrease of the spreading resistance, and hence lower mean temperatures.

In Figure 3.19, mean junction temperatures are compared for two different mounting plate materials, namely, copper and aluminum. Clearly, the material with higher thermal conductivity has lower spreading resistance, and hence, lower temperature.

3.7.3 Discussion

From the above results, we can conclude the following for the design of the 100 kVA converter:

– Mounting plates made of materials with higher thermal conductivity contribute to the

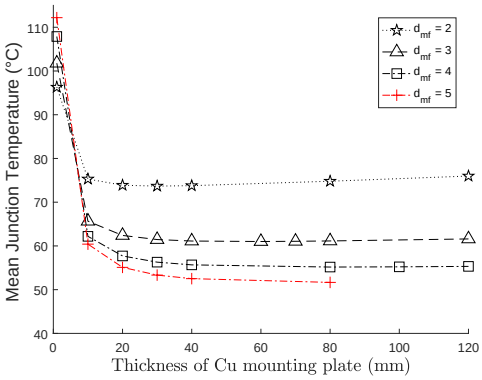

Figure 3.18 Variation of the IGBT mean junction temperature with respect to mounting plate dimensions.

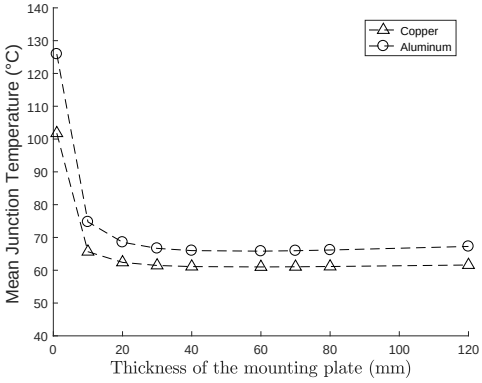

Figure 3.19 Comparison of the IGBT mean junction temperatures based on the mounting plate material; $d_{mf} = 3$.

lowering of the junction temperature. However, other factors such as coefficient of thermal expansion must also be taken into account while selecting the mounting plate material.

- The marginal utility decreases with increase in the mounting plate thickness.
- Marginal utility of increasing the d_{mf} also decreases with increase in the value of d_{mf}.
- The optimum mounting plate thickness increases with the increase in d_{mf}.
- Maximum value of d_{mf} in a practical converter will depend on the available space and placement of other devices in the enclosure.
- For the space available in the converter considered here, mounting plate thickness of about 30 mm, and d_{mf} of 3 seems a reasonable choice.

Furthermore, commercial forced water cooling systems usually have a heat sink-to-ambient thermal resistance in the range of 0.005-0.020 W/m·K, whereas forced air cooling systems have this value around 0.1 W/m·K. This implies that cooling efficiency of passively cooled systems in water (in this case, roughly 0.05W/m·K) can be designed to fall between two forced cooling mechanisms. The benefit of the passive cooling system lies in its low cost, simplicity and reliability.

This study considered a flat outer surface of the enclosure. Normally, finned surfaces are known to improve cooling. In the submerged case, especially in the sea, using a finned surface could result in clogging/fouling, and hence overcome the benefits of the increase in surface area. More importantly, thermal resistance due to convection at the surface is only a small component of the total thermal resistance, as shown in Figure 3.16. However, finned surfaces devoid of clogging could aid cooling due to the chimney effect [39]. Whether that improvement is significant or not requires a detailed study. For very deep subsea applications, a pressure compensating fluid inside the power electronic enclosure may also be present. Its impact on the cooling of the electronics would be another interesting study to undertake.

3.8 Conclusion

This chapter proposed a thermal model to estimate the junction temperature in an IGBT module cooled by natural convection in water. The model can be used to design the heat sink for the submerged power converters, and in their reliability analysis. The model was experimentally validated on a small scale set up. Assuming that the scale effects do not significantly alter the model, the model was extended to a 100 kVA converter.

Results indicated that the case-to-ambient thermal resistance—especially the spreading resistances in mounting plate and enclosure wall—significantly contributes to the total thermal resistance. However, this will depend on the size of the system, power rating and the IGBT thermal parameters. Mounting plates made of materials with high thermal conductivity (e.g. Cu) can lower the junction temperatures significantly. Also, it was observed that the passive cooling in water is less efficient than the commercially available forced water-cooling systems. But passive systems are likely to be low cost, simple and more reliable.

The appropriate choice of the cooling system in submerged converters is more complicated. Besides the cost and reliability, the designer should also consider the lifetime models of the IGBTs, and the mission profile to which the IGBT is subjected to, etc. This is addressed in the subsequent chapters. Another natural extension of this work could be to develop models for multiple heat sources inside a sealed enclosure, which includes other heat sources than IGBTs.

Bibliography

[1] S. Yang, A. Bryant, P. Mawby, D. Xiang, L. Ran, and P. Tavner, "An industry-based survey of reliability in power electronic converters," *IEEE transactions on Industry Applications*, vol. 47, no. 3, pp. 1441–1451, 2011.

[2] C. Qian, A. M. Gheitaghy, J. Fan, H. Tang, B. Sun, H. Ye, and G. Zhang, "Thermal management on igbt power electronic devices and modules," *IEEE Access*, vol. 6, pp. 12 868–12 884, 2018.

[3] M. Andresen, M. Liserre, and G. Buticchi, "Review of active thermal and lifetime control techniques for power electronic modules," in *Power Electronics and Applications (EPE'14-ECCE Europe), 2014 16th European Conference on*. IEEE, 2014, pp. 1–10.

[4] U. Shipurkar, E. Lyrakis, K. Ma, H. Polinder, and J. Ferreira, "Lifetime comparison of power semiconductors in three-level converters for 10mw wind turbine systems," *IEEE Journal of Emerging and Selected Topics in Power Electronics*, vol. 6, no. 3, pp. 1366–1377, 2018.

[5] H. Wang, K. Ma, and F. Blaabjerg, "Design for reliability of power electronic systems," in *IECON 2012-38th Annual Conference on IEEE Industrial Electronics Society*. IEEE, 2012, pp. 33–44.

[6] J. Carroll, A. McDonald, and D. McMillan, "Reliability comparison of wind turbines with dfig and pmg drive trains," *IEEE Transactions on Energy Conversion*, vol. 30, no. 2, pp. 663–670, 2015.

[7] T. Hazel, H. H. Baerd, J. J. Legeay, and J. J. Bremnes, "Taking power distribution under the sea: design, manufacture, and assembly of a subsea electrical distribution system," *IEEE Industry Applications Magazine*, vol. 19, no. 5, pp. 58–67, 2013.

[8] F. Wani and H. Polinder, "A Review of Tidal Current Turbine Technology: Present and Future," in *Proceedings of the 12th European Wave and Tidal Energy Conference (EWTEC),* 2017.

[9] K. Rajashekara and H. Krishnamoorthy, "Power Electronics for Subsea Systems: Challenges and Opportunities," in *12th International Conference on Power Electronics and Drive Systems (PEDS),*. IEEE, 2017, pp. 986–991.

[10] M. Sousounis, J. Shek, and M. Mueller, "Modelling and control of tidal energy conversion systems with long distance converters," in *7th IET International Conference on Power Electronics, Machines and Drives (PEMD 2014),* IET, 2014, pp. 1–6.

[11] X. Liang, S. O. Faried, and O. Ilochonwu, "Subsea cable applications in electrical submersible pump systems," *IEEE Transactions on Industry Applications*, vol. 46, no. 2, pp. 575–583, 2010.

[12] A. Von Jouanne, D. A. Rendusara, P. N. Enjeti, and J. W. Gray, "Filtering techniques to minimize the effect of long motor leads on pwm inverter-fed ac motor drive systems," *IEEE Transactions on Industry Applications*, vol. 32, no. 4, pp. 919–926, 1996.

[13] H. Bhowmik and K. Tou, "Experimental study of transient natural convection heat transfer from simulated electronic chips," *Experimental Thermal and Fluid Science*, vol. 29, no. 4, pp. 485–492, 2005.

[14] M. Musallam, C. M. Johnson, C. Yin, H. Lu, and C. Bailey, "Real-time life expectancy estimation in power modules," in *2008 2nd Electronics System-Integration Technology Conference,* IEEE, 2008, pp. 231–236.

[15] S. Yang, D. Xiang, A. Bryant, P. Mawby, L. Ran, and P. Tavner, "Condition monitoring for device reliability in power electronic converters: A review," *IEEE Transactions on Power Electronics*, vol. 25, no. 11, pp. 2734–2752, 2010.

[16] O. S. Senturk, S. Munk-Nielsen, R. Teodorescu, L. Helle, and P. Rodriguez, "Electro-thermal modeling for junction temperature cycling-based lifetime prediction of a press-pack IGBT 3L-NPC-VSC applied to large wind turbines," *IEEE Energy Conversion Congress and Exposition: Energy Conversion Innovation for a Clean Energy Future, ECCE 2011, Proceedings*, pp. 568–575, 2011.

[17] R. J. McGlen, R. Jachuck, and S. Lin, "Integrated thermal management techniques for high power electronic devices," *Applied thermal engineering*, vol. 24, no. 8-9, pp. 1143–1156, 2004.

[18] T. Frey, A. Stuck, and R. Zehringer, "Liquid cooling device for a high-power semiconductor module," 1999, US Patent 5,978,220.

[19] T. Zywiak and L. J. Bruno, "Cabin air conditioning system with liquid cooling for power electronics," 2008, US Patent 7,334,422.

[20] S. B. Memory, F. E. Ganaway, C. J. Rogers, A. C. DeVuono, A. Phillips, and Z. Zuo, "Modular cooling system and thermal bus for high power electronics cabinets," 2004, US Patent 6,828,675.

[21] M. Zhang, M. Jovanovic, and F. Lee, "Design and analysis of thermal management for high-power-density converters in sealed enclosures," *Proceedings of APEC 97 - Applied Power Electronics Conference*, vol. 1, pp. 405–412, 1997. [Online] http://ieeexplore.ieee.org/lpdocs/epic03/wrapper.htm?arnumber=581482

[22] P. M. Teertstra, M. M. Yovanovich, and J. R. Culham, "Modeling of Natural Convection in Electronic Enclosures," *Journal of Electronic Packaging*, vol. 128, no. 2, p. 157, 2006. [Online] http://electronicpackaging.asmedigitalcollection.asme.org/article.aspx?articleid=1408321

[23] J. M. Gutierrez-Alcaraz, S. W. H. De Haan, and J. A. Ferreira, "Seawater based cold plate for power electronics," *2010 IEEE Energy Conversion Congress and Exposition, ECCE 2010 - Proceedings*, pp. 2985–2992, 2010.

[24] C.-L. Su, W.-L. Chung, and K.-T. Yu, "An energy-savings evaluation method for variable-frequency-drive applications on ship central cooling systems," *IEEE transactions on industry applications*, vol. 50, no. 2, pp. 1286–1294, 2014.

[25] A. B. Sanfiorenzo, "Cooling system design tool for rapid development and analysis of chilled water systems aboard us navy surface ships," Ph.D. dissertation, Cambridge, Massachussetts, Massachussetts Institute of Technology, 2013.

[26] H. V. Xuan, D. Lahaye, S. Ani, H. Polinder, and J. Ferreira, "Electrical generators for maritime application," in *2011 International Conference on Electrical Machines and Systems (ICEMS),* IEEE, 2011, pp. 1–6.

[27] S. S. Kang, "Advanced cooling for power electronics," in *7th International Conference on Integrated Power Electronics Systems (CIPS),* IEEE, 2012, pp. 1–8.

[28] J. Schulz-Harder, "Review on highly integrated solutions for power electronic devices," in *5th International Conference on Integrated Power Systems (CIPS),* VDE, 2008, pp. 1–7.

[29] S. Taieb, L. A. Hatem, and J. Balti, "Natural convection in an asymmetrically heated vertical channel with an adiabatic auxiliary plate," *International Journal of Thermal Sciences*, vol. 74, pp. 24–36, 2013.

[30] K. Ma, "Electro-thermal model of power semiconductors dedicated for both case and junction temperature estimation," in *Power Electronics for the Next Generation Wind Turbine System.* Springer, 2015, pp. 139–143.

[31] K. Ma, Y. Yang, and F. Blaabjerg, "Transient modelling of loss and thermal dynamics in power semiconductor devices," in *Energy Conversion Congress and Exposition (ECCE), 2014 IEEE.* IEEE, 2014, pp. 5495–5501.

[32] Y. Muzychka, J. Culham, and M. Yovanovich, "Thermal spreading resistance of eccentric heat sources on rectangular flux channels," *Journal of Electronic packaging*, vol. 125, no. 2, pp. 178–185, 2003.

[33] Y. A. Cengel and A. J. Ghajar, *Heat and Mass Transfer, Fundamentals & Application, Fifth Edition in SI Units*, 2015, vol. 5th.

[34] A. Bejan, *Convection heat transfer*. John wiley & sons, 2013.

[35] S. W. Churchill and H. H. Chu, "Correlating equations for laminar and turbulent free convection from a vertical plate," *International journal of heat and mass transfer*, vol. 18, no. 11, pp. 1323–1329, 1975.

[36] A. Demuren and H. Grotjans, "Buoyancy-driven flows—beyond the boussinesq approximation," *Numerical Heat Transfer, Part B: Fundamentals*, vol. 56, no. 1, pp. 1–22, 2009.

[37] D. D. Gray and A. Giorgini, "The validity of the boussinesq approximation for liquids and gases," *International Journal of Heat and Mass Transfer*, vol. 19, no. 5, pp. 545–551, 1976.

[38] W. To and J. Humphrey, "Numerical simulation of buoyant, turbulent flow—i. free convection along a heated, vertical, flat plate," *International journal of heat and mass transfer*, vol. 29, no. 4, pp. 573–592, 1986.

[39] Y. A. Cengel and T. H. Ngai, "Cooling of vertical shrouded-fin arrays of rectangular profile by natural convection: an experimental study," *Heat transfer engineering*, vol. 12, no. 4, pp. 27–39, 1991.

CHAPTER 4

Lifetime Analysis of IGBT Power Modules in Passively Cooled Tidal Turbine Converters

This chapter is the second in the series of three chapters on reliability of submerged power electronic converters for tidal turbines. In the previous chapter a thermal model for the passively cooled power converter was presented. In this chapter we use that model to estimate the useful lifetime of IGBT modules in a passively cooled submerged tidal turbine converter.

Also published (with minor modifications) as:
F. Wani, U. Shipurkar, J. Dong, H. Polinder, A. Jarquin-Laguna, K. Mostafa and G. Lavidas, "Lifetime Analysis of IGBT Power Modules in Passively Cooled Tidal Turbine Converters," in *Energies*, 13 (8), 2020.

Abstract

Thermal cycling is one of the major reasons of failure in power electronic converters. For submerged tidal turbine converters investigating this failure mode is critical in improving the reliability and minimizing the cost of energy from tidal turbines. This thesis considers a submerged tidal turbine converter which is passively cooled by sea water, and where the turbine has fixed-pitch blades. In this respect, this study is different from similar studies on wind turbine converters, which are mostly cooled by active methods, and where turbines are mostly pitch-controlled. The main goal is to quantify the impact of surface waves and turbulence in tidal stream velocity on the lifetime of the converter IGBT (insulated gate bipolar transistor) modules. The lifetime model of the IGBT modules is based on the accumulation of fatigue due to thermal cycling. Results indicate that turbulence and surface waves can have a significant impact on the lifetime of the IGBT modules. Furthermore, to accelerate the speed of the lifetime calculation, this chapter uses a modified approach by dividing the thermal models into low and high frequency models. The final calculated lifetime values suggest that relying on passive cooling could be adequate for the tidal converters as far as thermal cycling is concerned.

4.1 Introduction

Power electronic converters in tidal turbine drive trains regulate the power capture from the turbine, and convert the generated electricity into a grid compliant form at fixed voltage and frequency. The converter can be placed either onshore, on floating platforms, or they can be seabed-mounted adjacent to the generator. As mentioned before, this thesis considers a submerged seabed-mounted converter as shown in Figure 4.1. Submerged power converter also means limited access for maintenance, and hence reliability is paramount [1]. Improving reliability, and thus capacity factor, could be a major contributor to lowering the levelized cost of energy (LCOE) from tidal turbines [2]. According to [1], subsea converters for tidal farms will demand more than 5-year mean period between failures.

Due to similar operating principle, it is reasonable to assume that many modes of failures in tidal turbines would be similar to wind turbines (WTs). However, the frequency of occurrences of these expected failure modes may differ in each case. Multiple studies have identified converters as one of the most frequently failing subsystem in WTs [3, 4]. Among converter components, phase modules (IGBTs, gate-drive circuits, capacitors) were found to be more critical in terms of failure frequency [3, 5, 6].

Thermal cycling has been identified as one of the main reasons for failure in IGBT power modules [3, 7–10]. Premature failures from thermal cycling stresses can be prevented by adequately cooling power modules [3, 9, 10]. This cooling can be provided either by active methods, such as forced-water cooling, or by passive cooling. By passive cooling we mean a system where no active devices, such as pumps or fans, are used to cool the power modules. A simple possible example is to use a sealed enclosure inside which the power electronics module is bolted or welded to its walls, as

shown in Figure 4.2 [11, 12]. In this case the heat is conducted from the power module base plate to the walls of the enclosure, and finally dumped in the ambient sea water by natural convection.

The main objective of this chapter is to analyze whether passive cooling is a feasible option for a subsea converter from the reliability viewpoint. The reliability analysis is based on estimating the lifetime of the IGBT power modules in a tidal turbine converter, considering thermal cycling as the main failure mode. In this regard, the effect of turbulence in the tidal stream velocity and surface waves on the converter lifetime is analyzed.

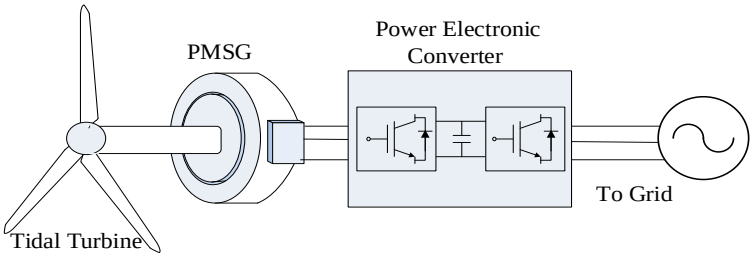

Figure 4.1 Tidal turbine drive train with a direct-drive permanent magnet synchronous generator (PMSG) and a power electronic (PE) converter. Figure is repeated here from previous chapter for better readability.

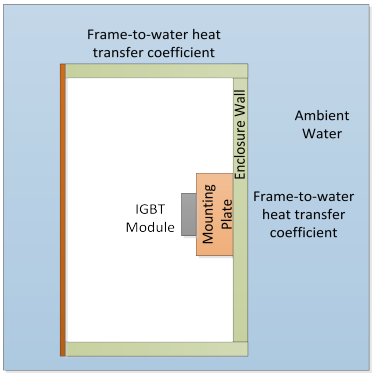

Figure 4.2 Power electronic module in a submerged and hermetically-sealed power converter [11].Figure is repeated here from previous chapter for better readability.

Liu et al. [13] studied the reliability of the power converter in a doubly-fed induction generator based tidal turbine. They show the impact of probability distribution of tidal velocity on the converter reliability. Ren et al. [14] used a sequential Monte-Carlo simulation-based method to quantify the effects of wake on tidal generator systems reliability in a tidal current farm. However, these studies do not specifically target the lifetime damage from thermal cycling in

power converters, nor do they incorporate the effects of turbulence or surface waves on the converter lifetime.

Extensive research has been carried out to study the lifetime models of power modules based on thermal cycling [15–18]. Nowadays, a priori estimation of lifetime is considered a logical step in designing reliable power electronic systems [9, 19, 20].

Shipurkar et al. [6] compared different three-level converter topologies for WT converters based on thermal lifetime models. Reliability of WT converters ranging from the influence of mission profiles to that of reactive power on the lifetime of IGBT modules, and comparison of multilevel converter topologies, etc. [19, 21–23] is also widely studied. Active control of cooling systems, switching frequency and modulation strategies, and power loss redistribution (in case of parallel converters) are some of the commonly used techniques to improve the lifetime in WT converters [24–26]. Adding redundancy is another way of improving the overall reliability in WT converters and subsea applications [1, 27].

Most of the aforementioned WT lifetime studies cover multi-MW pitch-controlled turbines with three-level medium voltage drives cooled by active methods (either water or air-cooled). This is the most common topology in modern WTs. However, active cooling mechanism usually suffer from drawbacks, such as pump failure and leakage of the coolant, which compromises the reliability to a certain degree.

The power converter under study in this thesis is different from a WT converter for the following reasons. Firstly, this study considers a passively cooled submerged converter to minimize potential fault points. For tidal turbines with submerged converter, an active cooling method is unsuitable due to high maintenance costs, and limited opportunities for maintenance. Secondly, modern WTs usually employ pitch control, which makes the converter design different from a tidal turbine converter with active speed stall-control investigated here. Thirdly, effects of site parameters, such as turbulence and waves on sea surface, is likely to have more impact on tidal turbine converters than on WT converters because of the higher speed oscillations in relatively smaller tidal turbines. Finally, an exhaustive lifetime analysis on the tidal turbine converters is missing in the literature.

Thermal cycling is not the only failure mechanism in IGBT modules. Fischer et al. [5] identified ambient humidity and moisture as the dominant failure mechanism in WT converters. However, in their study majority of the converters were liquid-cooled. On the other hand, hermetically sealed converters are less likely to fail due to moisture, which is the case with subsea power converters analysed in this study. Other failure mechanisms include corrosion, dielectric breakdown, etc [27]. These failure mechanisms are, however, extraneous to this study. For deep subsea applications (> 100 m) power converters are enclosed in pressurized enclosures [28, 29]. Tidal turbines are rarely deployed at this depth, hence, we do not consider pressurized power converters in this study.

The IGBT power packs considered in this study are packed in the form of power modules rather than discs. Despite low potential for cooling, modules are preferred because of better assembly,

integrated packaging, and good electrical isolation between the chip and the heat sink, and most importantly for low cost compared to other packaging methods [30].

The main contributions from this chapter, therefore, are:

- to assess the effect of turbulence and surface waves on the lifetime of semiconductor components for a passively cooled power converter coupled to a tidal turbine;
- to demonstrate the effect of active speed stall-control and lower inertia of tidal turbines on the generator side converter lifetime; and
- to propose a methodology for faster lifetime calculation in a passively cooled converter.

To the best of our knowledge, these factors are for the first time being addressed in the literature.

The following section defines the parameters adopted for characterizing the site conditions of a typical tidal site. In Section 4.3, the description of the tidal turbine energy conversion system used for analysis is given. Section 4.4 describes the methodology adopted for the calculation of lifetime in the passively cooled power converter. Section 4.5 briefly explains the thermal model of a sea water based passive cooling system. Section 4.6 gives the results of a case study carried out on a 110 kW tidal turbine system. Conclusions from the chapter are given in Section 4.7.

4.2 Site conditions

For a submerged power converter, the thermal loading on the power module is determined by the ambient sea conditions, and the design of the power take-off (PTO) system. In this section, we look at the parameters used to characterize a typical tidal site for this study. The values presented here are later used for analysis in Section 4.6.

The main characteristics of a tidal site pertinent for lifetime analysis are the mean tidal velocity, turbulence in the tidal stream velocity and surface waves. The main reason behind defining these parameters is to obtain a realistic instantaneous tidal stream velocity time series. This is achieved by the superimposition of turbulence ($\Delta v_{turbulence}$) and surface wave induced oscillations (Δv_{waves}) on the mean tidal stream velocity (v_{mean}) as,

$$v_{tide}(t) = v_{mean} + \Delta v_{turbulence} + \Delta v_{waves} \ . \tag{4.1}$$

Each component on the right hand side of the equation is described below. Again, the idea behind including the fluctuations in tidal stream velocity is to investigate whether they will influence the lifetime of the IGBT modules.

Please note that only ambient turbulence is considered in this thesis, the stall-related turbulence that might occur when the turbine operates in the stall condition is not accounted for. It is likely that accounting for stall-related turbulence would increase the speed oscillations of the generator/turbine, and could also affect the IGBT lifetime. This requires further investigation.

4.2.1 Mean tidal velocity

A tidal site with the frequency of occurrence as a function of tidal stream velocity is shown in Figure 4.3. This distribution profile is similar to that of the European Marine Energy Centre test facility in Orkney, Scotland [31].

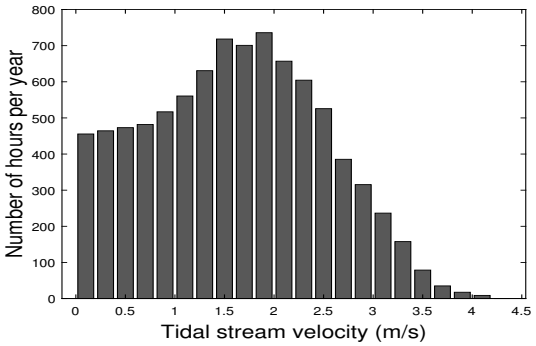

Figure 4.3 Tidal velocity distribution at EMEC site, Orkney [31].

Depending upon the location, a site may experience two flood and ebb tides roughly every 25 hours. Besides, most tidal sites also experience spring and neap tides roughly every 14 days, as shown in Figure 4.4. This information is relevant to investigate if the history of tidal velocity is also important for lifetime calculations, in addition to the instantaneous values.

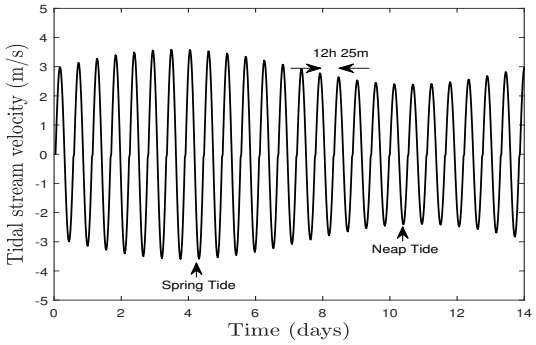

Figure 4.4 Tidal stream velocity profile at a typical tidal site experiencing semi-diurnal tides.

4.2.2 Turbulence in the tidal stream velocity

Turbulence induced velocity oscillations are likely to influence the current flowing through the IGBT modules, and hence play a critical role in determining the lifetime of the IGBT modules.

Figure 4.5 shows typical oscillations of the tidal velocity about its mean value. Some of these oscillations are attributed to the turbulence, usually characterized by the turbulence intensity (TI) values at the site. The turbulence intensity value is defined as [32],

$$TI = \frac{u'}{\bar{u}} \tag{4.2}$$

where, u' and $\bar{u}$ denote the rms value of the velocity fluctuations and mean velocity respectively.

Multiple factors are responsible for turbulence, and accurate prediction of turbulence is too complex task to be undertaken in this analysis. Therefore in this thesis, we use a stochastic flow field simulator called *Turbsim* to generate a realistic tidal stream flow data. For tidal flows, Turbsim uses a modified version of the SMOOTH spectral model based on turbulent kinetic energy and shear. The tool has been developed at National Renewable Energy Laboratories, US [33].

Typically turbulence values differ with mean tidal velocity and vertical position of the turbine with respect to the seabed. Also, different TI values are expected for flood and ebb tides [32]. For the tidal site under consideration, TI values used are listed in Table 4.1[1]. TI values have been divided into two categories, in accordance with [32].

Table 4.1 Turbulence intensity values used to generate time series of tidal stream velocity

Mean velocity range (m/s)	**Mean TI values(%)**
Ebb tide	
$0.5 \leq \bar{u} \leq 1.1$	13.9
$1.3 \leq \bar{u} \leq 3.5$	11.7
Flood tide	
$0.5 \leq \bar{u} \leq 1.1$	14.5
$1.3 \leq \bar{u} \leq 3.5$	12.0

4.2.3 Effect of surface waves

Waves on the sea surface may also cause oscillations in the velocity at the rotor hub. Zhou et al. studied the impact of these wave induced oscillations on the speed control of the tidal turbines [34]. The fluctuations about the mean tidal stream velocity at the rotor hub due to surface waves are calculated independently assuming the linear wave theory from the following equation [34]:

$$\Delta v_{waves}(t) = \sum_i \frac{2\pi a_i}{T_i} \frac{cosh(2\pi \frac{z+d}{L_i})}{sinh(2\pi \frac{z+d}{L_i})} \quad cos2\pi(\frac{t}{T_i} - \frac{x}{L_i} + \phi_i), \tag{4.3}$$

where a_i, L_i and T_i denote the amplitude, length and the period of the wave component respectively. z is the depth of the rotor hub, and d is the depth of the sea from the surface. The necessary

[1] This analysis only uses average value of TI for each mean tidal velocity; in reality, different values of TI are possible for the same tidal velocity.

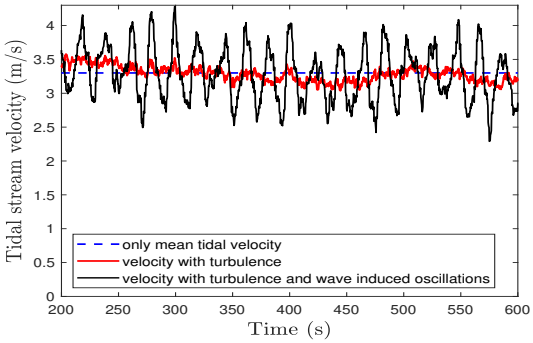

Figure 4.5 Fluctuations in tidal stream velocity about its mean value (here taken as 3.3 m/s) as a consequence of turbulence and wave induced oscillations.

parameters are listed in Table 4.2. Further details on the above equation are given in Appendix at the end of this chapter. For more information on this please see [35].

In this thesis, JONSWAP spectrum is chosen as the wave spectrum for not fully developed waves [36]. In other words, wave spectra is more dependent on local winds rather than the swell phenomenon [37]. Peak enhancement factor value for the spectrum is chosen as 3.3, which is the mean value for North Sea [38].

In Figure 4.5 the effect of turbulence (TI of 13%) and a surface wave (significant wave height, Hs = 5.75 m, and peak period, Tp = 11 s) on the mean tidal velocity (3.3 m/s) is shown. The extreme wave case is chosen here to make the effects of waves more visible.

Table 4.2 Turbine Rotor Parameters

Parameter	**Value**
Hub depth from surface	20 m
Rotor Diameter	6.5 m
Seabed depth from surface	30 m

A tidal site experiences different wave conditions throughout the year, and quantifying the impact of each wave condition on the lifetime of the IGBTs is a cumbersome task. Therefore, we limit ourselves to only analysing the impact of a representative summer and a winter month. We further assume that 6 such summer and winter months occur in a year. The total impact from all the waves in a year is calculated by estimating the impact from each wave condition, and then multiplying it with its probability of occurence. Probability density matrices for a representative summer and a winter month are shown in Tables 4.3 and 4.4 [39].

Table 4.3 Probability density (%) of waves according to significant wave heights and time periods for May 2009 at Orkney.

Tp(s), Hs(m)	0.25	0.75	1.25	1.75	2.25	2.75	3.25	3.75	4.25	4.75	5.25	5.75	6.25
3	6.92	2.82	2.35	0	0	0	0	0	0	0	0	0	0
5	4.97	0.27	0.87	0.47	0	0	0	0	0	0	0	0	0
7	3.96	0	0.07	1.75	1.01	0	0.74	0	0	0	0	0	0
9	5.98	0	1.81	0.34	0.2	0	0.94	0.87	0.40	0	0	0	0
11	2.48	3.76	4.77	6.72	6.18	3.96	2.08	0.07	1.61	0.27	0.27	0.13	0
13	0.47	1.07	2.89	4.91	2.22	2.01	4.57	4.30	0.27	0	0	0.13	0.20
15	0.47	0.67	0.13	0.34	0	0.20	0.13	2.55	0.87	0.40	0.20	0.34	0
17	0	0	0	0	0	0	0.13	0.26	1.14	0	0	0	0

Table 4.4 Probability density (%) of waves according to significant wave heights and time periods for November 2009 at Orkney.

Tp(s), Hs(m)	0.25	0.75	1.25	1.75	2.25	2.75	3.25	3.75	4.25	4.75	5.25	5.75	6.25
3	0	0.27	2.22	0	0	0	0	0	0	0	0	0	0
5	0	0.69	6.11	1.04	1.32	0.07	0	0	0	0	0	0	0
7	0	0	0.55	1.25	1.87	3.61	2.22	0.42	0	0	0	0	0
9	0	0	0.83	0	0.35	0.76	1.53	1.11	0	0	0	0	0
11	0	2.64	3.40	7.22	7.29	0.35	0	0	0	0	0	0	0
13	0	2.15	2.29	4.30	13.95	10.07	2.78	0.69	0	0	0	0	0
15	0	0	1.46	0.63	1.18	7.5	1.87	1.39	0	0	0	0	0
17	0	0	0.21	0	0	0.35	2.01	0	0	0	0	0	0

4.2.4 Sea temperature

The junction temperature of the IGBT also depends on the ambient temperature. In case of passive cooling, the ambient temperature also affects the external heat transfer coefficient, and thus the enclosure wall-to-ambient thermal resistance. For the tidal site near Orkney (UK), the annual sea temperature variation is shown in Figure 4.6.

4.3 System description

The PTO in this study broadly comprises a turbine (rotor), a generator and a power electronic converter. The turbine is rated at 110 kW with a rated speed of 30 rpm. The power rating is similar to the power rating of actual NOVA Innovation's M100 tidal turbine installed in Shetland, Orkney (UK). The necessary specifications for each of these components are as follows.

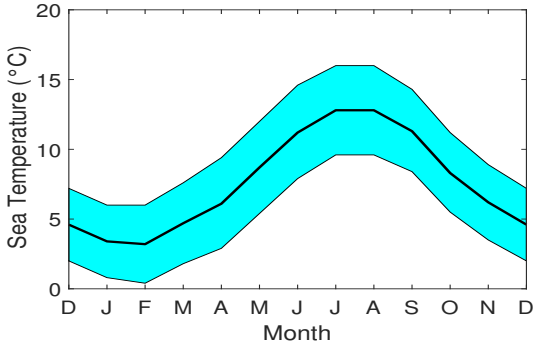

Figure 4.6 Annual sea temperature ranges at Kirkwall near Orkney, UK. The black curve in the middle of the shaded area represents the average temperature. Data source: [40].

4.3.1 Turbine rotor hydrodynamic characteristics

A fixed-pitch tidal turbine was selected for this study, with a $C_p - \lambda$ curve shown in Figure 4.7. Here, C_p and λ are the power coefficient and tip-speed ratio of the turbine, respectively. The cut-in and cut-out speeds are 0.5 m/s and 3.3 m/s respectively. The turbine power and speed variations with the mean tide speed are shown in Figures 4.8 and 4.9 respectively.

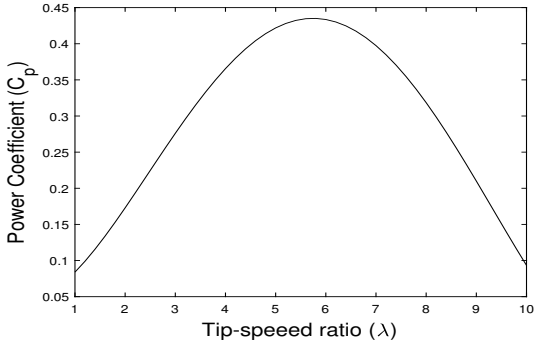

Figure 4.7 $C_p - \lambda$ curve for the tidal turbine; adapted from [45].

The speed is controlled by using the active speed stall-control instead of the pitch control [41], [42], [44]. Whereas, pitch control is common for turbines with larger power ratings (≥1 MW), for low power tidal turbines (≤300 kW) it is more common having fixed-pitch blades or operating pitch control only when the tides change direction. Furthermore, having no pitch control could potentially improve the overall reliability of the system.

The turbine dynamics are governed by the following equations:

$$P = \frac{1}{2} C_p(\lambda) \rho A v_{tide}^3(t), \tag{4.4}$$

$$J_m \frac{d\omega_m}{dt} = T_m - T_e, \tag{4.5}$$

where P is the power developed by the turbine blades, A is the area swept by the turbine blades and ρ is the mass density of the water. J_m, ω_m, T_m and T_e denote the total rotational moment of inertia of the turbine system, rotational velocity of the turbine, mechanical torque and electromagnetic torque (developed by generator) respectively.

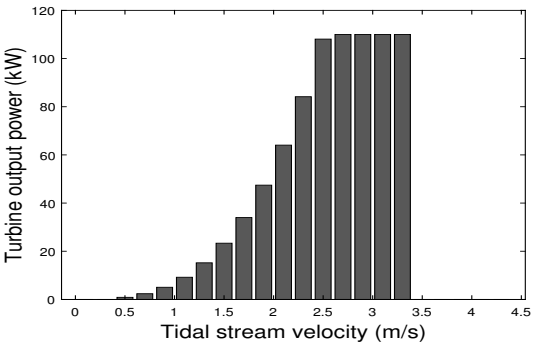

Figure 4.8 Power curve of the fixed-pitch tidal turbine as a function of the tidal stream velocity.

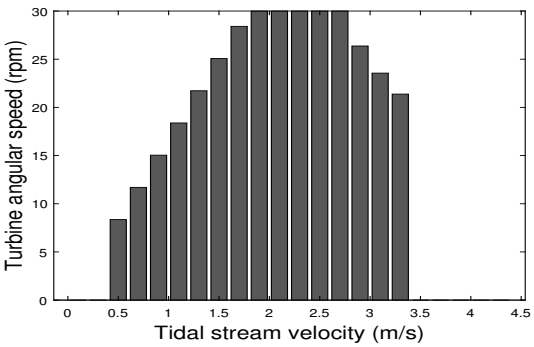

Figure 4.9 Speed curve of the fixed-pitch tidal turbine as a function of the tidal stream velocity.

4.3.2 Generator speed control

In this analysis the generator is assumed to be a direct-drive permanent magnet (PM) generator with surface mounted magnets. The electrical parameters of the generator are listed in Table 4.5.

The speed of the generator is controlled by employing the classical PI-control in dq-axes.

Using power invariant transform, the q-axis current is calculated from the reference torque value T_e^* (obtained from the external speed control loop) as,

$$i_q = \frac{T_e^*}{p\lambda_m} \tag{4.6}$$

where, p is the number of pole pairs of the generator, and λ_m is the magnetic flux linkage due to PM. On the other hand, flux weakening strategy is utilized if $i_d = 0$ results in a higher terminal voltage than can be delivered by the converter [45].

The d-axis current i_d, is obtained as follows,

$$\begin{aligned} i_d &= 0 \qquad (\text{if} \quad v_{d(i_d=0)}^2 + v_{q(i_d=0)}^2 \leq V_{max}^2) \\ \text{else,} \quad i_d &= \frac{-\lambda_m}{L_s} + \sqrt{\left(\frac{V_{max}}{\omega_e L_s}\right)^2 - i_q^2} \quad , \end{aligned} \tag{4.7}$$

where v_d is the d-axis terminal voltage, v_q is the q-axis terminal voltage, ω_e is the electrical frequency and V_{max} is the maximum output voltage of the converter. The d and q axes voltages, and the torque developed by the generator are computed by the following equations:

$$v_d = R_s i_d - p\omega_m L_q i_q, \tag{4.8}$$

$$v_q = R_s i_q + p\omega_m (L_d i_d + \lambda_m), \tag{4.9}$$

$$T_e = 1.5p[\lambda_m i_q - (L_d - L_q) i_d i_q], \tag{4.10}$$

where, i_d, v_d, L_d are the direct axis components of the stator quantities. Similarly i_q, v_q, L_q are the quadrature axis quantities. Also, p is the number of pole-pairs of the generator, R_s is the resistance per phase and λ_m is the flux linkage contributed from magnets (can be derived from no-load voltage). The electrical parameters for the machine are listed in Table 4.5.

Table 4.5 Generator Parameters

Parameter	**Value**
Rated Power	110 kW
Rated speed	30 rpm
Pole pairs	40
No-load emf at 30 rpm	188 V
Resistance per phase	0.04 Ω
Synchronous inductance per phase	4 mH
Mass Moment of Inertia	6100 kg.m^2

4.3.3 Converter specifications

The converter under investigation is a back-to-back two-level voltage source converter (2L-VSC), represented in Figure 4.10. 2L-VSCs are widely used in low voltage applications because of their simplicity [28]. Whereas the generator side converter controls the speed(or torque) of the generator, the grid side converter controls the real and/or reactive power flow to the grid at grid voltage and frequency. Both the converters are connected by an intermediate DC-link capacitance.

The DC-link voltage of the converter is calculated based on the line voltage of the grid side, according to the following equation [27]:

$$V_{dc} = x\frac{2\sqrt{2}}{\sqrt{3}}\frac{1}{m} \quad V_{ll} \tag{4.11}$$

where, x is the overvoltage factor (here limited to 1.15); m is the modulation index (again, limited to 1.15) for space vector modulation; and V_{ll} is the line-to-line rms voltage. The DC-link capacitor value is calculated similar to [27].

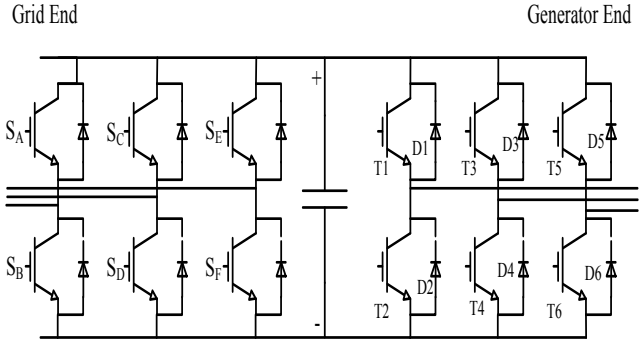

Figure 4.10 Representative diagram of a 2L-VSC.

The voltage rating of the IGBT is selected based on the dc-link voltage. The current rating is then determined by the desired kVA rating of the converter. For the turbine controlled by active speed stall strategy, an overrated converter is required [42]. In this analysis, the cut-out speed of the turbine is 3.3 m/s. The current rating of the converter is then determined by assuming a sudden surge of 0.9 m/s above the cut-off speed, to prevent the turbine from going into the braking/parking mode. The maximum rms value of the current during this surge is 580 A. Furthermore, should an unaccounted surge in velocity occur, we assume that the emergency braking systems in the turbine will take over bypassing the converter control. This could be done, for instance, by using a resistive braking system.

Based on the above discussion, Infineon's IGBT power module with part number FF600R12ME4 (1200 V, 600 A) was selected for the 2L-VSC. If the surge current capacity is not considered, even

a 400 A switch will suffice. However, in the next chapter we shall show that opting for a 600 A switch proves useful from the lifetime perspective as well. The 4-layer Foster network thermal parameters for FF600R12ME4 power module pack are listed in Table 4.6 [43].

Inside the converter enclosure each power module is mounted on a copper mounting plate, which is attached to the enclosure wall. The thickness of the copper plate is chosen as 20 mm, as the marginal utility in terms of reducing the thermal spreading resistance decreases beyond this thickness. More details on design of mounting plate thickness are given in Chapter 3.

Table 4.6 Converter Parameters

Parameter	**Value**
DC-link voltage	600 V
Switching Frequency	2 kHz
DC-link capacitance	102 mF
IGBT part number	**FF600R12ME4**
Voltage and Current Rating (rms)	1200 V, 600 A
Module Dimensions	0.057m x 0.110 m
IGBT $R_{th,j-c}$	[0.0038 0.0312 0.0001 0.0020] K/W
IGBT $\tau_{th,j-c}$	[0.0007 0.0247 0.050 3.485] s
Diode $R_{th,j-c}$	[0.0008 0.0489 0.002 0.0057] K/W
Diode $\tau_{th,j-c}$	[0.0006 0.0245 0.0733 0.9951] s
Enclosure wall thickness	0.010 m
Enclosure height	1.5 m
Enclosure width	0.5 m
Enclosure length	1.5 m
Cu mounting plate dimensions	0.171 m x 0.330 m
Cu mounting plate thickness	0.020 m
Thermal paste thickness	0.001 m

4.4 Lifetime modeling of power modules: Methodology

Lifetime analyses for wind energy converters based on active water cooling systems have been vastly studied [6, 18, 19]. Because the passive cooling system is considered here, this means that the lifetime calculation has to be done in a slightly modified manner to speed-up the calculations. This is due to the longer time constant of the passive cooling system. The main methodology is shown in Figure 4.11. The calculations are performed in time domain. The temperature cycles are then calculated using the rainflow counting algorithm [18, 46].

The high thermal capacitance of the enclosure wall makes the thermal models relatively slow in terms of computation time. For the short-term cycling, these computations are accelerated in this thesis by assuming that the enclosure wall is at a constant temperature as long as the mean tidal velocity remains constant. The idea is to obtain the wall temperature from the model taking

only mean tidal velocity variation into account. This wall temperature information is then used as a boundary condition in the fast converter thermal model to estimate the junction temperature cycling near the power frequency. This is illustrated in Figure 4.11.

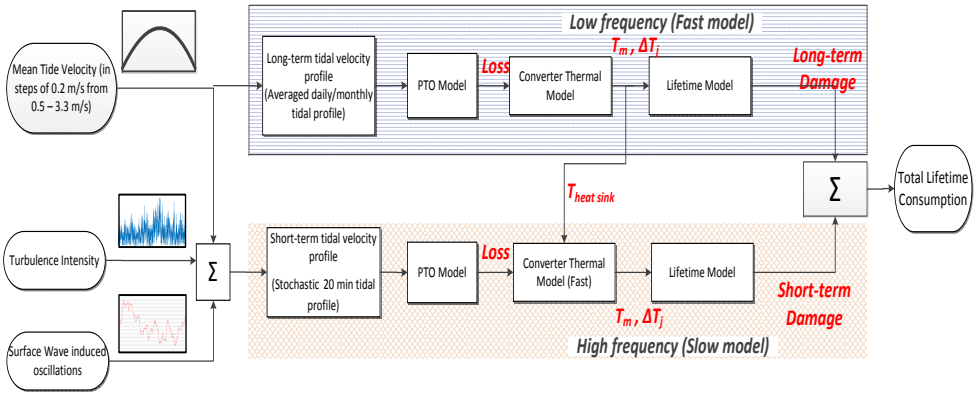

Figure 4.11 Methodology for lifetime calculations. Finer details of the PTO model are shown in Figure 4.12.

Thermal cycling can be divided into two main categories: long-term and short-term. By long term cycling we mean cycles due to variation in tidal current speeds over 12-hourly cycles, and variations due to the spring and neap tide cycles, as shown in Figure 4.4. Although monthly and/or yearly variations in the tides can also be included, these have been neglected in this analysis, as their impact is expected to be negligible. Short-term cycling mainly refers to power-frequency thermal cycling and other oscillations due to turbulence and surface waves in the mean tidal stream velocity.

The lifetime estimation in this work has been based on the models presented in [6, 15]. These models give the number of thermal cycles to failure as a function of various parameters, with emphasis on junction temperature cycling and its mean value as per the following equation:

$$N_f = A \cdot \Delta T_j^{\beta_1} \cdot e^{\frac{\beta_2}{T_{j,m}+273}} \cdot t_{on}^{\beta_3} \cdot I^{\beta_4} \cdot V^{\beta_5} \cdot D^{\beta_6} \tag{4.12}$$

N_f is the number of cycles to failure , $T_{j,m}$ is the mean junction temperature , and t_{on} is the on-pulse duration, I current per wire, V is the chip blocking voltage and D is the bonding wire diameter. The constants, A, β_1 to β_6 are obtained from [30], and take the following values: $A = 9.34\times10^{14}$ for IGBT4 modules, $[\beta_1,...,\beta_6]$ = [-4.416, 1.285×10^3, -0.463, -0.716, -0.761, -0.5].

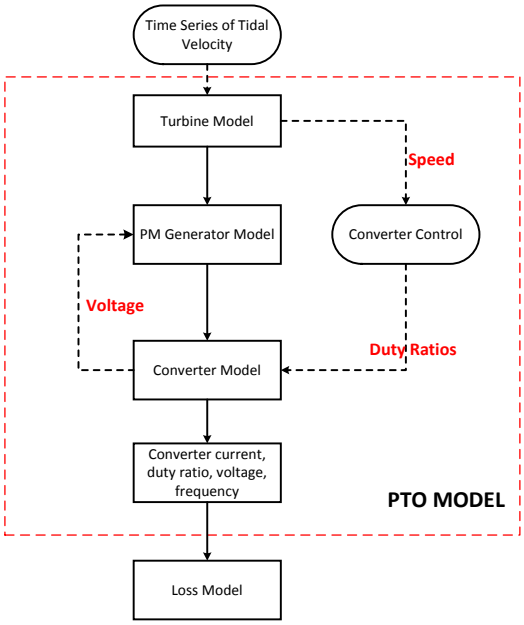

Figure 4.12 Internal structure of the PTO model.

The lifetime calculation is based on the junction temperature of the IGBT and the diode. These values are calculated from the thermal model of the converter explained in the next section. After the calculation of thermal cycles, the number of cycles to failure are calculated based on the Miner's rule [19]. That is,

$$\sum_i \frac{n_i}{N_i} = 1 \tag{4.13}$$

where, n_i is the number of cycles to failure at the temperature cycle ΔT_i, and N_i is the number of cycles to failures for the same amplitude and same stress type. The number of cycles for each thermal cycling amplitude are obtained from (4.12). Figure 4.13 shows how N_f typically varies with ΔT_j for constant $T_{j,m}$.

Following assumptions have been made in this analysis to reduce the calculation time:

- A constant sea water temperature of 15°C was assumed, neglecting variation in annual temperature.
- A constant turbulence value has been used for each mean tidal velocity, as already mentioned in Section 4.2.

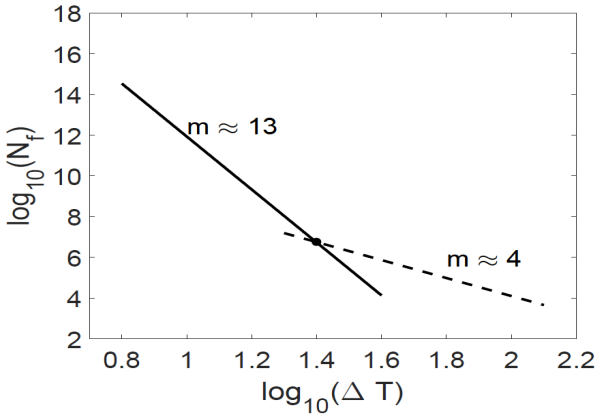

Figure 4.13 Number of cycles to failure are presented as a function of temperature cycling for a constant mean junction temperature.

– The turbine under consideration is an active speed stall-controlled one, with no yawing capabilities. It is assumed that the performance of the turbine drops negligibly between the flood and ebb tides. Hence, as far as turbine characteristics are concerned, no distinction is made between the flood and ebb tides.

– At the beginning of each flood and ebb tide cycle, the junction temperature of the IGBT module is same as the ambient temperature.

– A constant power factor of operation (0.9) is assumed on the grid-side converter. In other words, effects of varying reactive power on thermal cycling have been neglected [27].

4.5 Estimation of junction temperatures

The mean junction temperature and its amplitude about the mean value are obtained from the thermal models of the passively cooled converter [11]. The losses inside the IGBT and diode comprise of the conduction and the switching losses given by the following equations [27]:

$$\begin{aligned} P_{cond,IGBT} &= u_{CE}(i,T_j)\, i\, d_{IGBT}, \\ P_{cond,Diode} &= u_F(i,T_j)\, i\, d_{Diode}, \\ P_{sw,IGBT} &= \Big(E_{on,IGBT}(T_j) + E_{off,IGBT}(T_j)\Big) f_s, \quad \text{and} \\ P_{sw,Diode} &= \Big(E_{on,Diode}(T_j) + E_{off,Diode}(T_j)\Big) f_s \end{aligned} \tag{4.14}$$

where, $P_{cond,k}$ and $P_{sw,k}$ denote the conduction and switching losses respectively in the device 'k'. u_{CE} and u_F represent the forward voltage drops in the IGBT and diode respectively, whereas i is

the component current. d_k is the duty ratio of the switch 'k'. And, $E_{on,k}$ and $E_{off,k}$ is the on and off switching energy of the device 'k'; and f_s is the switching frequency. Parameters for the loss calculations can be found in datasheets for IGBT modules in [47]. Details on loss calculation in the IGBT and diodes can be found in multiple references such as [6, 19, 27]. Equation (4.14) can be expressed as a flowchart as shown in Figure 4.14.

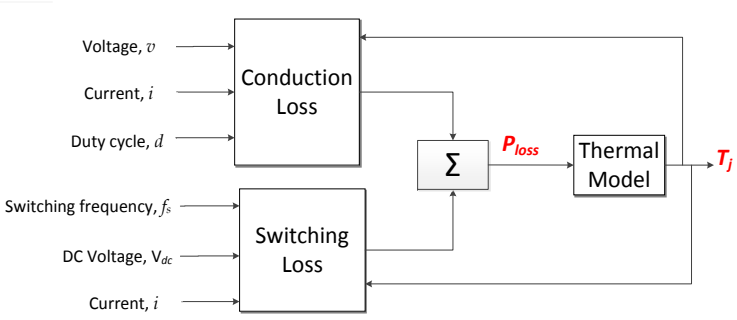

Figure 4.14 Loss calculation in IGBT and diode. The diagram shows that losses also depend on the junction temperature T_j, hence, the feedback loop from the thermal model.

The RC-thermal network of the submerged power converter with IGBT mounted on a Cu mounting plate (see Figure 4.2) inside the sealed enclosure is shown in Figure 4.15 [11]. Calculation of the case-to-ambient thermal resistances shown in Figure 4.15 have been explained in the previous chapter (and also [11]). However, a qualitative description of the thermal model is again given below to help the reader recall important details.

Heat transfer from the IGBT junction to the ambient sea water encounters three main thermal resistances (or impedances): IGBT junction-to-case, case-to-external wall, external wall-to-ambient water. The junction-to-case thermal network is represented typically by a 4-layer Foster network given in the datasheet of the IGBT module [47]. However, Foster models cannot be directly connected to the RC-ladder network of the rest of the thermal network. Therefore, a slightly modified approach using a 1-layer equivalent network, as explained in [11,48] is adopted as shown in Figure 4.15.

The mounting plate and the enclosure wall thermal impedances include the case-to-external wall impedances. These can be represented by one-dimensional thermal resistance together with the spreading resistances in the mounting plate and the enclosure wall [11, 49]. These spreading resistances form the bulk of the thermal resistance in case of the passively cooled submerged power converters. Proper selection of the mounting plate material and dimensions can significantly reduce the spreading resistance, as discussed in [11]. The thermal capacitance calculations of the mounting plate and the wall are simply calculated using the heat capacity of these blocks.

And finally, the wall-to-ambient sea water thermal resistance is calculated using empirical rela-

tions [50], and a few steady state computational fluid dynamics (CFD) simulations, as explained in the previous chapter. The convective heat transfer coefficient is a function of the mean power loss and/or wall temperature. The enclosure wall resistance is thus a dynamic variable, and needs to be recalculated continuously.

Whereas for the forced water cooling methods the case-to-ambient thermal resistance is almost independent of the heat loss in the power module, same cannot be said for the passively cooled converter. For the latter, heat transfer coefficient at the external wall of enclosure is a function of the heat flux from the power module [11]. Commonly encountered values of case to ambient thermal resistance for forced water cooled systems falls in the range of 0.005-0.020 K/W. In this study, depending on the heat loss this thermal resistance falls in the range of 0.02-0.1 K/W. The case-to-sea water thermal resistance decreases with increase in loss in the power module. Please note that increased thermal resistance in passive cooling is compensated by its improved reliability due to no moving parts.

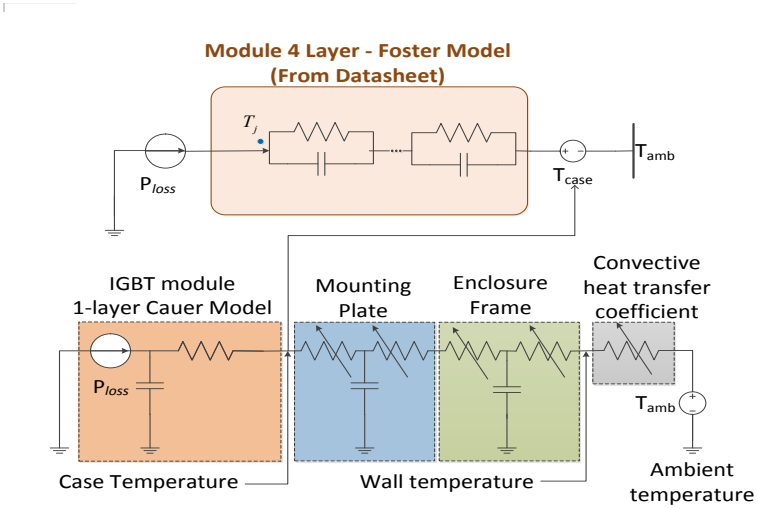

Figure 4.15 Lumped element thermal network model for the system shown in Figure 4.2.

4.6 Case study: Lifetime analysis of a tidal turbine converter

In this section we apply the lifetime model presented earlier to a 110 kW tidal turbine PTO system, specified in Section 4.3. The idea is to first demonstrate the speed control algorithm works as expected, and then assess the impact of loading on the lifetime due to various operating conditions to which the PTO is subjected to.

4.6.1 Speed control

Figure 4.16 shows the corresponding variation in the generator speed against the tidal stream velocity. In Figure 4.16 the generator is operating at the rated power near cut-off speed of 3.3 m/s. This means that for any increase in the tidal velocity, the generator rpm must drop as a consequence of the active speed stall-control to maintain constant power. As expected, for higher fluctuation in tidal stream velocity, the generator speed also varies with higher magnitude.

4.6.2 Converter loading

The change in the tidal stream velocity is also reflected as the change in the phase current of the generator. This can be seen in Figure 4.17. A comparison between Figures 4.16 and 4.17 shows that the drop in generator speed is accompanied by the increase in current. In the constant power region, drop in phase emf due to reduced speed is compensated by the increase in current, and vice-versa.

Another observation from Figure 4.16 is that there is a substantial change in the generator speed as a result of the change in tidal stream velocity. This characteristic is particular to tidal turbines controlled by active speed stall. Compare this with the data obtained from a case study of a 10 MW wind turbine, as shown in Figure 4.18 [6]. Both the 10 MW wind turbine and 110 kW tidal turbine are operating in the region of constant power above the rated wind and tidal speed; whereas wind turbine is pitch-controlled, the tidal turbine is active speed stall-controlled.

The point to note here is that the fluctuations in wind speed will not be reflected so much in the generator currents as much as the fluctuations in tidal speed would be. This is both a consequence of pitch control as well as the large inertia of the wind turbine rotor over the tidal turbine. As a result when a pitch-controlled wind turbine operates in the region of constant power, its speed is nearly constant and so is the magnitude of the phase currents. Therefore, significant differences in the lifetime consumption of the power semiconductor devices can be expected in wind and tidal turbines, as a result of change in the incoming wind and tidal current velocity. We shall return to this point again in the next chapter.

4.6.3 Junction temperatures

For the corresponding currents shown in Figure 4.17, the Generator side converter diode (D1) and IGBT (T1) junction temperatures are shown in Figures 4.19 and 4.20 respectively. Figure 4.19 also shows the zoomed-in version, where power cycling (high frequency) can be seen alongside the low frequency cycling caused by turbulence and surface waves. Similar high frequency cycling will also be observed in Figure 4.20, however, we omit showing that here for sake of brevity. As expected, the junction temperatures follow a similar trend to the phase currents because the losses increase with the increase in current.

The mean junction temperature of the diode increases with the increase in the tidal stream velocity, as shown in Figure 4.21. At lower tidal velocities, this is because of the increase in output power. In the constant power range, the increase in mean junction temperature is inversely

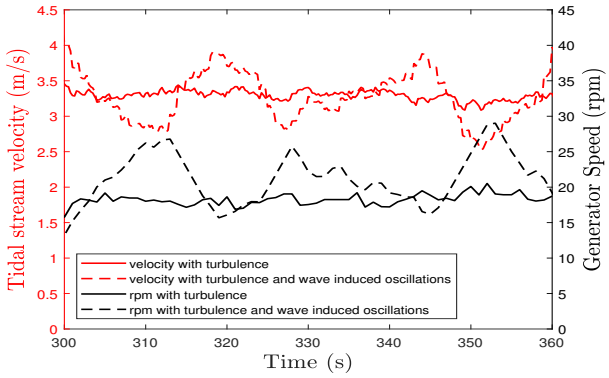

Figure 4.16 Active speed stall-control of generator speed as a function of change in tidal stream velocity. Mean tidal velocity in this image is set at 3.3 m/s.

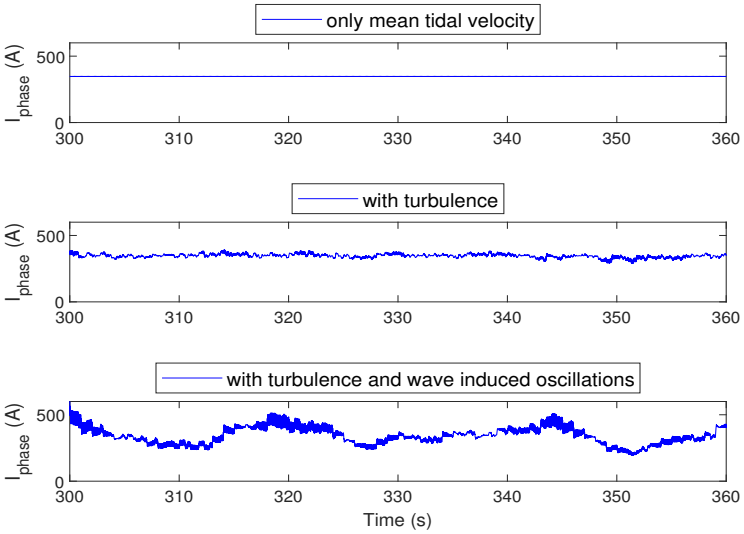

Figure 4.17 Generator phase currents (RMS values).

related to the generator speed. Consequently, bulk of the lifetime consumption of the power semiconductor devices is expected above rated speed.

The results here are shown only for a 60 s interval for a specific value of mean tidal velocity, turbulence and wave condition. However, the total lifetime analysis is performed over the entire range of the tidal velocity and the wave spectrum (see Tables 4.3 and 4.4), in accordance with Figure 4.11.

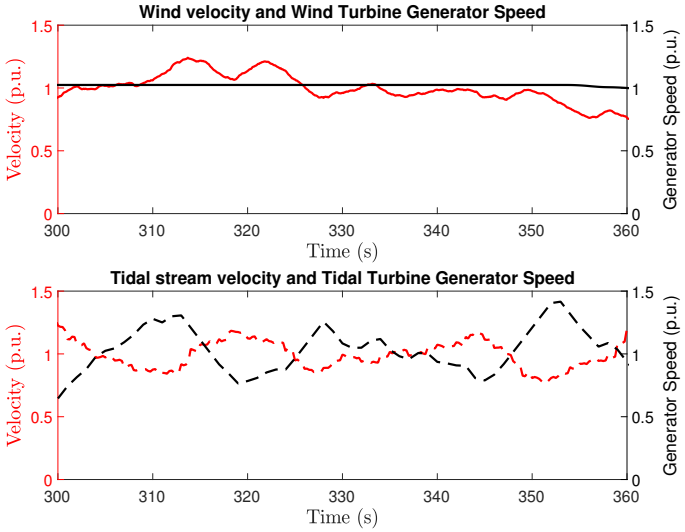

Figure 4.18 Comparison of generator speed fluctuations in a 10 MW wind turbine and a 110 kW tidal turbine.

4.6.4 Lifetime consumption

The estimated lifetime of the converter is presented in Table 4.7. The critical component in terms of lifetime was found to be the diode of the generator side converter, which is taken as the lifetime of the converter. For this reason, results from the grid side converter are not presented in this thesis. It is evident that including turbulence and surface waves has a significant effect on the estimated lifetime.

Another interesting thing to note here is that even though the lifetime drops significantly because of the turbulence in tidal stream velocity, the difference in annual loss of the converter IGBT modules with and without turbulence is negligible, as shown in Table 4.8. This also implies that in this case is the magnitude of temperature swing is more responsible for component degradation than the mean value of temperature. The mean junction temperature is a function of the mean power loss. For the waveforms shown in Figure 4.19, the temperature swings are listed in Table 4.9.

Table 4.7 Lifetime Values

Velocity type	**Lifetime (in years)**
Considering only mean tidal velocity	151.5
With turbulence	67.0
With turbulence and waves	38.2

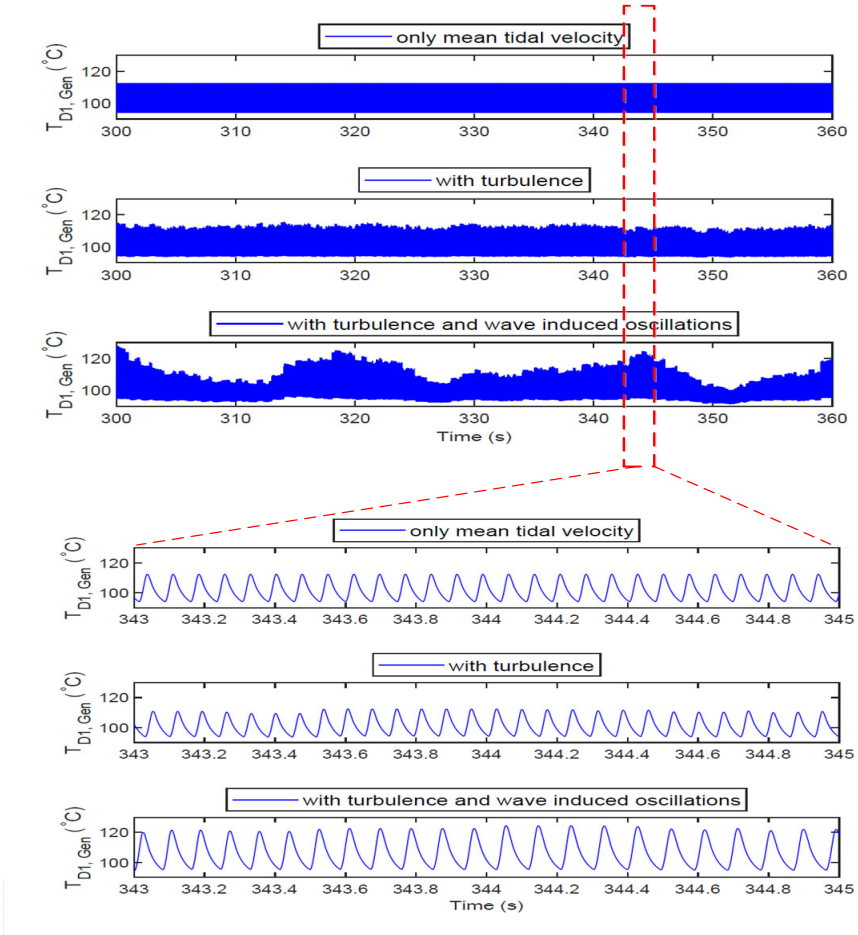

Figure 4.19 Temperature of the Generator side converter diode (D1) as a function of the fluctuations in the tidal stream velocity. These curves correspond to the currents shown in Figure 4.17 and/or the generator speeds depicted in Figure 4.16.

Normally the tidal turbines are designed to have a lifetime of 20 years. Therefore, from above results it can be said that passive cooling can provide adequate lifetime as long as the system is properly designed, and devices are properly rated. Moreover, improvements in lifetime can be gained by overrating the devices further, as demonstrated in other studies [6].

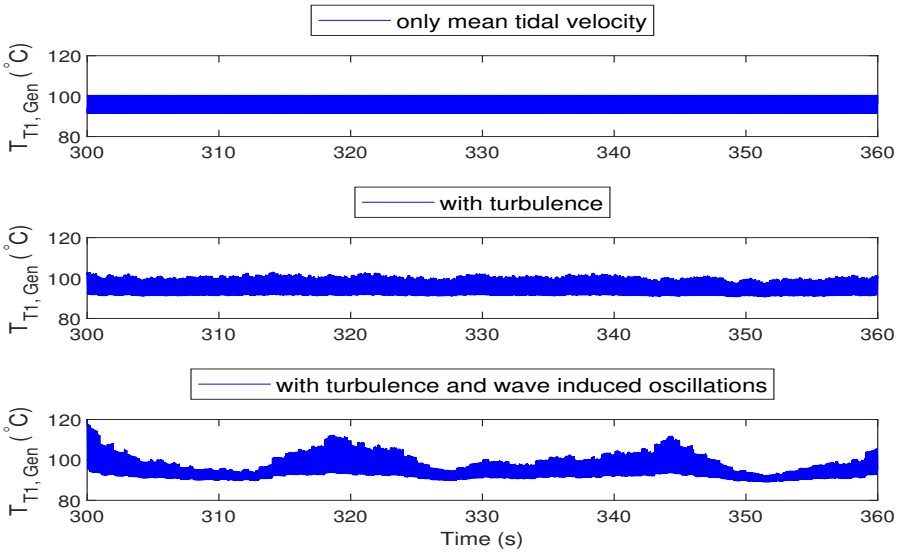

Figure 4.20 Temperature of the Generator side converter IGBT (T1) as a function of the fluctuations in the tidal stream velocity.

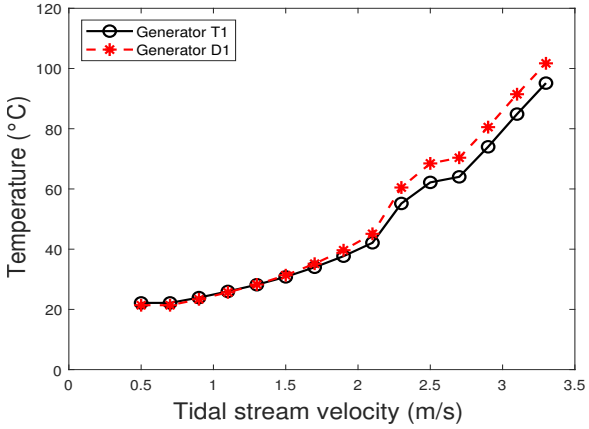

Figure 4.21 Mean junction temperature of Generator side converter diode.

4.6.5 Damage distribution

To understand the damage distribution better due to turbulence and wave induced speed oscillations, we consider the operation of the tidal turbine near rated speed (2.5 m/s). Assuming no fluctuations in the tidal stream velocity, almost all of the damage is done by the power cycling frequency—that is, frequency of the generator phase currents which is about 20 Hz—as shown in

Table 4.8 Annual Generator Side Converter Loss (includes losses for all phases)

Velocity type	Generator IGBTs (in MWh)	Generator Diodes(in MWh)
Considering only mean tidal velocity	2.11	2.53
With turbulence	2.07	2.44

Table 4.9 Diode Temperatures corresponding to Figure 4.19.

Velocity type	$T_{j,D1,max}$ ($^{\circ}C$)	$T_{j,D1,min}$ ($^{\circ}C$)	$\Delta T_{j,D1}$($^{\circ}C$)
Mean tidal velocity	112.4	93.3	18.4
With turbulence	115.5	93.4	21.1
With turbulence and waves	129.6	91.5	38.1

Figure 4.22.

When turbulence is included in the tidal stream velocity, the damage distribution histogram shows a lot of frequency components in the lower frequency range as seen in Figure 4.22. This arises because of the lower frequency components in the junction temperatures of the diode when turbulence is included. Furthermore, if a wave induced oscillation from a wave of time period of 11 s is superimposed on the tidal stream velocity with turbulence, the damage distribution is reflected in this frequency range (< 0.10 Hz) as well. Therefore, turbulence and wave induced oscillations not only cause more damage but also shift the damage distribution to lower frequency components.

There is another component of thermal cycling or damage not seen in Figure 4.22. This thermal cycling component arises because of the daily variation of mean tidal velocity as explained in section 4.4. The mean junction temperature of the generator diode D1 varies with the tidal stream velocity as shown in Figure 4.21. This low frequency cycling in the mean junction temperature is what we refer to as long term damage. The frequency and magnitude of long term cycling depends on the history of the mean tidal velocity. In other words, the amplitude and period of each long term cycle depends on whether it was a spring or a neap tide cycle; this was highlighted in Section 4.2.

The net lifetime damage due to long term cycling is constant irrespective of whether turbulence and waves are included or not. Therefore, the damage contribution in percentage from long term cycling is less when other effects such as turbulence or waves are accounted for, as seen in Table 4.10.

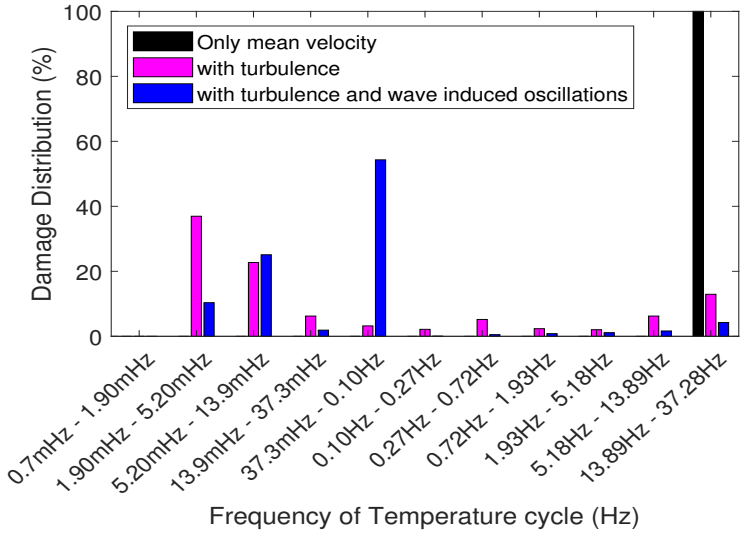

Figure 4.22 Percentage of total damage vs. frequency of thermal cycling, when turbulence and surface wave (Hs = 5.75 m, Tp = 11 s) is superimposed to the mean tidal velocity of 2.5 m/s.

Table 4.10 Lifetime Values

Velocity type	**Damage from daily cycling (%)**
Considering only mean tidal velocity	27
With turbulence	12
With turbulence and waves	6.9

4.7 Conclusion

The purpose of this chapter was to investigate the lifetime of IGBT modules for tidal turbine power converters on the basis of thermal cycling. The converter is submerged and passively cooled by sea water. Results indicate that in such a converter significant reduction in lifetime of the IGBT modules can occur because of the turbulence and surface waves. Daily variations in the mean tidal velocity also contribute, albeit little, to the reduction in lifetime. It was observed that passive cooling can yield adequate lifetime for the IGBT modules in tidal turbine converters. Whereas passive cooling is less prone to failure than forced water cooling methods, the latter can provide better cooling. On the other hand, passive cooling on account of its reliability can minimize maintenance expenses, and reduce cost of energy in the long term. Unless even the most optimally designed passive cooling system proves inadequate, forced cooling methods should not necessarily be the first choice. Furthermore, passive cooling systems have longer thermal time constants than forced cooling systems, which would mean longer computation

time for the thermal models. Therefore, this chapter used a modified approach to reduce the computation time by dividing the thermal model into low and high frequency models.

Appendix

Parameters used in (4.3) can be obtained from following equations:

$$\begin{aligned} a_i &= \sqrt{2S(f_i)\Delta f}, \\ L_i &= \frac{gT_i^2}{2\pi} tanh(2\pi \frac{d}{L_i}) \end{aligned} \tag{4.15}$$

$$\begin{aligned} S(f) &= \beta_j \frac{H_s^2}{T_p^4} \frac{1}{f^5} exp(-\frac{4}{5} \frac{1}{T_p^4 f^4}) \gamma^Y, \\ \beta_j &= 0.09624(1.094 - 0.0195 \log\gamma)/0.23 + 0.0336\gamma - 0.185(1.9+\gamma), \end{aligned} \tag{4.16}$$

$$\begin{aligned} Y &= exp\big[\frac{-(T_p f - 1)^2}{2\sigma^2}\big], \\ \sigma &= 0.07, \quad \text{if} \quad f \le \frac{1}{T_p}, \\ &= 0.09, \quad \text{if} \quad f \ge \frac{1}{T_p}, \end{aligned} \tag{4.17}$$

where H_s is the significant wave height and T_p is the peak time period.

Bibliography

[1] N. Vedachalam, S. Babu, G. Ramadass and M. Atmanand, "Review of maturing multi-megawatt power electronic converter technologies and reliability modeling in the light of subsea applications", *Applied Ocean Research*, vol. 46, pp. 28–39, 2014.

[2] D. Magagna, R. Monfardini and A. Uihlein, "JRC Ocean Energy Status Report". *European Commission*, Luxembourg, 2016. [Online] https://setis.ec.europa.eu/sites/default/files/reports/ocean_energy_report_2016.pdf, [Last accessed: 20 Dec 2019].

[3] J. Carroll, A. McDonald and D. McMillan, "Reliability comparison of wind turbines with DFIG and PMG drive trains", *IEEE Transactions on Energy Conversion*, vol. 30, pp. 663–670, 2014.

[4] CATAPULT, "Portfolio review 2016: System performance, availability and reliability trends analysis (SPARTA)", 2017. [Online] https://s3-eu-west-1.amazonaws.com/media.ore.catapult/wp-content/uploads/2017/03/28102600/\protect\@normalcr\relaxSPARTAbrochure_20March-1.pdf, [Last accessed: 01 Jan 2020].

[5] K. Fischer, K. Pelka, S. Puls, M. Poech, A. Mertens, A. Bartschat, B. Tegtmeier, C. Broer and J. Wenske, "Exploring the causes of power-converter failure in wind turbines based on comprehensive field-data and damage analysis", *Energies*, vol. 12, pp. 593-619, 2019.

[6] U. Shipurkar, E. Lyrakis, K. Ma, H. Polinder and J. Ferreira, "Lifetime comparison of power semiconductors in three-level converters for 10 MW wind turbine systems", *IEEE Journal of Emerging and Selected Topics in Power Electronics*, vol. 6, 1366–1377, 2018.

[7] Y. Hu, P. Shi, H. Li, and C. Yang, "Health condition assessment of base-plate solder for multi-chip IGBT module in wind power converter", *IEEE Access*, vol. 7, pp. 72134–72142, 2019.

[8] C. Qian, A. Gheitaghy, J. Fan, H. Tang, B. Sun, H. Ye and G. Zhang, "Thermal management on IGBT power electronic devices and modules", *IEEE Access*, vol. 6, pp. 12868–12884, 2018.

[9] Y. Yang, H. Wang, A. Sangwongwanich and F. Blaabjerg, "Design for reliability of power electronic systems", in *Power Electronics Handbook*, 4th ed. Oxford, UK: Elsevier, pp. 1423-1440, 2018. [Online] https://www.sciencedirect.com/science/article/pii/B9780128114070000519

[10] P. Tavner, J. Xiang and F. Spinato, "Reliability analysis for wind turbines", *Wind Energy*, vol. 10, pp. 1–18, 2007.

[11] F. Wani, U. Shipurkar, J. Dong, and H. Polinder, "A study on passive cooling in subsea power electronics", *IEEE Access*, vol. 6, pp. 67543–67554, 2018.

[12] D. Toma, A. Mànuel-Làzaro, M. Nagueras and J. Del Rio, "Study on heat dissipation and cooling optimization of the junction box of OBSEA seafloor observatory", *IEEE/ASME Transactions on Mechatronics*, vol. 20, pp. 1301–1309, 2014.

[13] M. Liu, W. Li, C. Wang, R. Billinton and J. Yu, "Reliability evaluation of a tidal power generation system considering tidal current speeds", *IEEE Transactions on Power Systems*, vol. 31, pp. 3179–3188, 2016.

[14] Z. Ren, H. Li, W. Li, X. Zhao, Y. Sun, T. Li and F. Jiang, "Reliability evaluation of tidal current farm integrated generation systems considering wake effects", *IEEE Access*, vol. 6, pp. 52616–52624, 2018.

[15] R. Bayerer, T. Herrmann, T. Licht, J. Lutz and M. Feller, "Model for power cycling lifetime of IGBT modules – various factors influencing lifetime", in *Proceedings of 5th International Conference on Integrated Power Systems (CIPS)*, Nuremberg, Germany, 2008, pp. 1–6.

[16] M. Musallam, C. M. Johnson, C. Yin, H. Lu and C. Bailey, "Real-time life expectancy estimation in power modules", in *2nd Electronics System-Integration Technology Conference*, Greenwich, UK, 2008, pp. 231–236.

[17] I. F. Kovacevic-Badstuebner, J. W. Kolar, U. Schilling, H. Chung, H. Wang, F. Blaabjerg and M. Pecht, "Modelling for the lifetime prediction of power semiconductor modules", in *Reliability of Power Electronic Converter Systems*, 2015, IET, London, UK, pp. 103–140.

[18] M. Ikonen, *Power cycling lifetime estimation of IGBT power modules based on chip temperature modeling*, PhD Dissertation, Lappeenranta University of Technology, Lappeenranta, Finland, 2012.

[19] K. Ma, M. Liserre, F. Blaabjerg and T. Kerekes, "Thermal loading and lifetime estimation for power device considering mission profiles in wind power converter", *IEEE Transactions on Power Electronics*, vol. 30, pp. 590–602, 2015.

[20] K. Givaki, M. Parker and P. Jamieson, "Estimation of the power electronic converter lifetime in fully rated converter wind turbine for onshore and offshore wind farms", in *Proceedings of 7th IET International Conference on Power Electronics, Machines and Drives (PEMD)*, Manchester, UK, 2014.

[21] K. Ma, M. Liserre and F. Blaabjerg, "Reactive power influence on the thermal cycling of multi-MW wind power inverter", *IEEE Transactions on Industry Applications*, vol. 49, pp. 922–930, 2013.

[22] D. Zhou, F. Blaabjerg and M. Lau, M. Tønnes, "Optimized reactive power flow of DFIG power converters for better reliability performance considering grid codes" *IEEE Transactions on Industrial Electronics*, vol. 62, pp. 1552–1562, 2014.

[23] K. Ma and F. Blaabjerg, "Multilevel converters for 10 MW wind turbines", in *Proceedings of the 14th European Conference on Power Electronics and Applications*, Birmingham, UK, 2011, pp. 1–10.

[24] M. Andresen, K. Ma, G. Buticchi, J. Falck, F. Blaabjerg and M. Liserre, "Junction temperature control for more reliable power electronics", *IEEE Transactions on Power Electronics*, vol. 33, pp. 765–776, 2017.

[25] G. Chen and X. Cai, "Adaptive control strategy for improving the efficiency and reliability of parallel wind power converters by optimizing power allocation", *IEEE Access*, vol. 6, pp. 6138–6148, 2018.

[26] M. Andresen, J. Kurpat, V. Raveendran, J. Falck and M. Liserre, "Active thermal control for delaying maintenance of power electronics converters" *Chinese Journal of Electrical Engineering*, vol. 33, pp. 13–20, 2018.

[27] U. Shipurkar, *Improving the Availability of Wind Turbine Generator Systems*, PhD dissertation, Delft University of Technology, Netherlands, 2019.

[28] K. Rajashekara, H. Krishnamoorthy and B. Satish, "Electrification of subsea systems: requirements and challenges in power distribution and conversion", *CPSS Transactions on Power Electronics and Applications*, vol. 2, pp. 259–266, 2017.

[29] M. Hernes and R. Pittini, "Enabling pressure tolerant power electronic converters for subsea applications", in *Proceedings of the 13th European Conference on Power Electronics and Applications*, New Jersey, USA, 2009, pp. 1–10.

[30] A. Wintrich, U. Nicolai, W. Tursky and T. Reimann. Application manual power semiconductors. SEMIKRON International GmbH, 2015. [Online] https://www.semikron.com/dl/service-support/downloads/download/semikron-application-manual-\protect\@normalcr\relaxpower-semiconductors-english-en-2015/, [Last accessed: 30 Oct 2019].

[31] CATAPULT, “ReDAPT - Public Domain Report: Final (MC7.3). Technical report,” 2015. [Online] http://redapt.eng.ed.ac.uk/library/eti/reports/MC7.3%20Operations%20Final%20Report.pdf, [Last accessed: 05 Jan 2020].

[32] B. Sellar, G. Wakelam, D. Sutherland, D. Ingram and V. Venugopal, "Characterisation of tidal flows at the european marine energy centre in the absence of ocean waves", *Energies*, vol. 11, p. 176, 2018.

[33] B. Jonkman, L. Kilcher. Turbsim User's Guide: Version 1.06.00, National Renewable Energy Laboratories. Colorado, USA. [Online]. https://nwtc.nrel.gov/TurbSim, [Last accessed: 25 Sep 2019].

[34] Z. Zhou, F. Scuiller, J. F. Charpentier, M. Benbouzid and T. Tang, "Power smoothing control in a grid-connected marine current turbine system for compensating swell effect", *IEEE Transactions on Sustainable Energy*, vol. 4, pp. 816–826, 2013.

[35] H. Chen, W. Xie, X. Chen, J. Han, N. Ait-Ahmed, Z. Zhou, T. Tang and M. Benbouzid, M, "Fractional-order PI control of dfig-based tidal stream turbine", *Journal of Marine Science and Engineering*, vol. 8, p. 1875, 2020.

[36] Z. Zhou, M. Benbouzid, J. F. Charpentier, F. Scuiller and T. Tang, "A review of energy storage technologies for marine current energy systems", *Renewable and Sustainable Energy Reviews*, vol. 18, pp. 390–400, 2013.

[37] A. Techet, "MIT Ocean Engineering: Ocean Waves." [Online] https://ocw.mit.edu/courses/mechanical-engineering/2-22-design-principles-for-ocean-vehicles-13-42-\protect\@normalcr\relaxspring-2005/readings/lec6_wavespectra.pdf, [Last accessed: 20 Dec 2019].

[38] BS 6349: Part 1: Maritime structures, code of practice for general criteria. B. S. Institute, 2000.

[39] G. Lavidas and V. Venkatesan, "Characterising the wave power potential of the scottish coastal environment", *International Journal of Sustainable Energy*, vol. 37, pp. 684–703, 2017.

[40] Climate-data.org. Climate: Kirkwall. [Online] https://en.climate-data.org/location/56552/, [Last accessed: 05 Mar 2018].

[41] B. Whitby and C. E. Ugalde-Loo, "Performance of pitch and stall regulated tidal stream turbines" *IEEE Transactions on Sustainable Energy*, vol. 5, pp. 64–72, 2014.

[42] H. Polinder, D. Bang, R. Van Rooij, A. McDonald and M. Mueller, "10 MW wind turbine direct-drive generator design with pitch or active speed stall control", in *Proceedings of IEEE International Electric Machines and Drives Conference*, Antalya, Turkey, 2007, pp. 1390–1395.

[43] K. Ma, "Electro-thermal model of power semiconductors dedicated for both case and junction temperature estimation", in *Power Electronics for the Next Generation Wind Turbine System*, Springer Cham, London, UK, 2015, pp. 139–143.

[44] S. Djebarri, J. F. Charpentier, F. Scuiller and M. Benbouzid, "A systemic design methodology of PM generators for fixed-pitch marine current turbine", in *1st International Conference on Green Energy*, 2014, pp. 32–37.

[45] Z. Zhou, F. Scuiller, J. F. Charpentier, M. Benbouzid and T. Tang, "Power control of a non-pitchable PMSG-based marine current turbine at overrated current speed with flux-weakening strategy", *IEEE Journal of Oceanic Engineering*, vol. 40, pp. 536–545, 2015.

[46] M. Denk and M. Bakran, "Comparison of counting algorithms and empiric lifetime models to analyze the load-profile of an IGBT power module in a hybrid car", in *3rd International Electric Drives Production Conference (EDPC)*. IEEE, 2013, pp. 1–6.

[47] Infineon Technologies, "IGBT Modules." [Online] https://www.infineon.com/cms/en/product/power/igbt/igbt-modules/, [Last accessed: 15 Sep 2019].

[48] K. Ma, Y. Yang, F. Blaabjerg, "Transient modelling of loss and thermal dynamics in power semiconductor devices", in *Energy Conversion Congress and Exposition (ECCE)*, Pittsburg, PA, USA, 2014, pp. 5495–5501.

[49] Y. Muzychka, J. Culham and M. Yovanovich, "Thermal spreading resistance of eccentric heat sources on rectangular flux channels", *Journal of Electronic packaging*, vol. 125, pp. 178–185, 2003.

[50] Y. A. Cengel and A. J. Ghajar. *Heat and Mass Transfer, Fundamentals & Application, Fifth Edition in SI Units*, McGraw-Hill, New York, 2014.

CHAPTER 5

Thermal Cycling in IGBT Modules with Different Cooling Systems in Pitch and Active Stall-Controlled Tidal Turbines

This chapter is the last in the series of three chapters on reliability of submerged power electronic converters for tidal turbines. In the previous chapter, we presented the lifetime analysis for power modules in a passively cooled power converter. Effects of turbulence and surface waves on the module lifetime were also investigated. In this chapter, we compare active and passive cooling systems in submerged converter on the basis of module lifetime. In addition to this, influence of having either the active speed stall or the pitch control of the turbine on module lifetime is also studied.

Abstract

This chapter compares active and passive cooling systems in tidal turbine power electronic converters. The comparison is based on the lifetime of the IGBT (insulated gate bipolar transistor) power modules, calculated from the accumulated fatigue due to the thermal cycling. The lifetime analysis accounts for the influence of site conditions, namely turbulence and surface waves. Moreover, we study the influence of pitch control and active speed stall control on the IGBT lifetime. Results indicate that active cooling results in significant improvement in IGBT lifetime over the passive cooling. The lifetime improvement is primarily due to the reduction in the mean junction temperature of the diodes in IGBT modules, and not the amplitude of thermal cycling. On the other hand, passive cooling systems are inherently more reliable. Furthermore, we show that IGBT modules in pitch-controlled turbines are likely to have longer lifetimes than their counterparts in stall-controlled turbines, for the same power rating. In conclusion it is possible for passive cooling systems to provide adequate cooling in tidal turbine converters, both for pitch-controlled and active speed stall-controlled turbines. In other words, passively cooled converters provide an opportunity to improve the reliability of tidal turbine systems.

5.1 Introduction

As mentioned in the previous chapters, power converters require cooling in order to prevent their early failure from thermo-mechanical stress. Such failures occur mostly in IGBT (insulated gate bipolar transistors) power modules from thermal cycling [1,2]. The time to failure from this failure mechanism can be prolonged by providing adequate cooling to the IGBT power modules. For submerged power converter, an active cooling method, such as forced water cooling, is undesirable due to the limited opportunities for maintenance [3]. On the other hand, passive cooling systems offer higher degree of reliability, albeit at a lower cooling efficacy [1,3]. Therefore, a comparison between different cooling systems becomes imperative.

In a passively cooled system, IGBT modules can be mounted directly on the interior walls of the sealed enclosure via a mounting plate, as shown in Figure 5.1 [3,4]. The walls of the enclosure directly exchange heat with the sea water via natural convection. For active cooling systems, the modules are mounted on a heat sink through which a coolant is driven by means of a pump [1], as seen in Figure 5.2.

This chapter takes further the work done in the previous chapter, where lifetime analysis of IGBT modules in a passively cooled converter was studied. In this chapter, we evaluate the feasibility of the passive cooling system by comparing it with an active cooling system. Here, by active cooling system we mean a forced water cooling system. The reason is that latter is the standard choice in tidal turbine converters, and the former has potentially the highest reliability, and is likely to be inexpensive with no energy consumption. The cooling systems are compared in terms of the mean junction temperatures, the amplitude of thermal cycling, annual losses in the IGBT modules, and the damage distribution w.r.t the tidal velocity. We also overrate the forced water

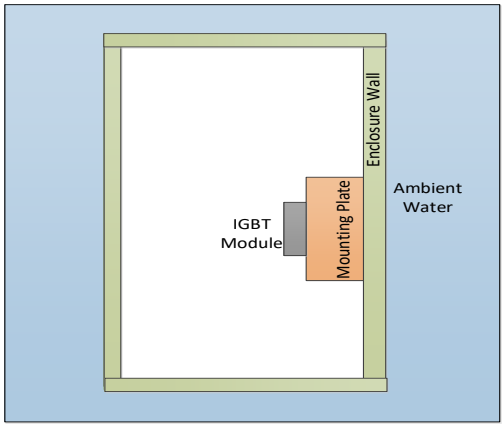

Figure 5.1 Passive cooling: power electronic module in a submerged and hermetically sealed power converter [3].

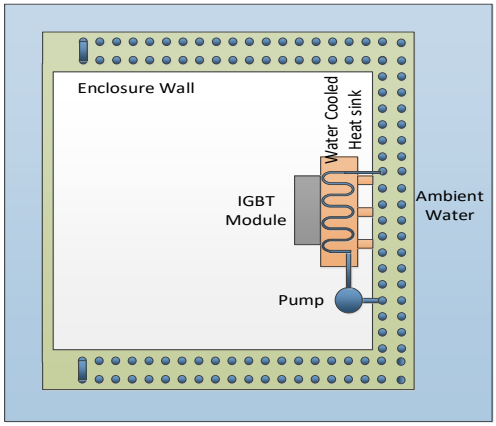

Figure 5.2 Active cooling: a liquid coolant, such as water, is passed through a heat sink on which the IGBT modules are mounted. The coolant then exchanges the heat with the ambient sea water through a separate heat exchanger, which may be embedded in the converter walls.

cooling system to show how it can be used to further improve the lifetime.

Furthermore, we look at the lifetime of the IGBT modules in two similarly rated (power and speed) tidal turbines. The turbines differ in the mechanism of power regulation beyond the rated speed. One of the turbines utilizes the active speed stall control, whereas the other employs pitch control [5, 6]. Both these systems can be found in commercial tidal turbines [7].

The main contributions from this chapter can be summarized as:

- to evaluate active and passive cooling systems in terms of the lifetime of IGBT modules in tidal turbine converters, and
- to study the impact of active speed stall and pitch control on the IGBT lifetime.

The rest of the chapter is structured as follows. The following section gives a literature review of active and passive cooling systems used for cooling of power semiconductor devices (including IGBT modules), and lifetime analyses of IGBT modules. In doing so, Section 5.2 also justifies the system selected for this study. In Section 5.3, the description of the tidal stream turbine system used for analysis in this chapter is given. Section 5.4 describes the methodology adopted for the calculation of IGBT module lifetime. Section 5.5 briefly explains the thermal model for active (forced water) and passive cooling systems. Section 5.6 gives the results of a case study carried on a 110 kW tidal turbine system. Conclusions from the chapter are given in Section 5.7.

5.2 Literature review

First of all little data, if any, is available regarding the failures of power electronics in tidal turbines. Due to similarity with wind turbines, it could be reasonably assumed that similar failures can be expected in tidal turbines. For direct drive generators with fully rated converters majority of the converter failures relate to the cooling system [8–10].

IGBT modules are one of the most commonly failing components in power converters [11–13]. Multiple studies suggest that IGBT modules fail due to the fatigue accumulated from thermal cycling [13–15]. Such failures are mainly due to the aging of bond-wires [14, 16], and solder fatigue [14, 17], see Figure 1.5.

However, Fischer et al. [12], recently claimed that most failures in wind turbines occurred from moisture and humidity, rather than thermal cycling. Because the submerged converter is hermetically sealed, moisture amount in the enclosure can be in principle controlled. No fresh air circulates in the enclosure, and the moisture already present inside can be absorbed by materials, such as silica. Another alternative could be to fill the enclosure with dehumidified air before submersion. Under these circumstances, thermal cycling can be expected to be a major failure mode in subsea power electronics.

Providing adequate cooling to a power module can limit the thermal cycling, thereby increasing the lifetime. The methods of cooling can be broadly classified into active and passive cooling methods. Active methods comprise of [1]:

- forced air cooling;
- forced liquid cooling;
- micro-channel heat sinks;
- Two-phase forced convection cooling;
- jet impingement and spray cooling; and

– hybrid solid and liquid cooling.

Active cooling systems could also be adaptively controlled to improve the lifetime of IGBT modules [18, 19]. The idea is to control the heat sink thermal resistance so as to minimize junction temperature cycling. Adaptive cooling or not, most actively cooled systems utilize rotating components, such as pumps, thus compromising reliability. However, an exception can be found in [20], where liquid metal is proposed as a coolant. The metal coolant is driven by a magnetohydrodynamic pump. This system eliminates any rotating components, thus improving reliability over conventional pumped systems. However, that system is not under consideration in this thesis.

On the other hand, passive cooling could be either of the following:

– air cooling [1]; and

– submerged water cooling [3, 4].

Of these aforementioned cooling techniques, this chapter compares the forced water cooling with passive (submerged) water cooling for submerged TST power electronic converters. The former because it is the most widely used one, and the latter because of its potentially highest reliability.

In addition to cooling, lifetime of converters can also be enhanced by using different converter topologies [13, 21]. In [21], neutral point clamped (NPC) and T-type inverters are compared based on the lifetime in photo voltaic inverters. In [13], authors compare different three-level converter topologies for wind turbine converters; they claim overrating components can lead to the improvement in lifetime, which is comparable to the improvement achieved from overrating topologies. This thesis, however, focuses on a two-level back-to-back converter. Two-level converters are widely used for low voltage applications owing to their simplicity [22]. Other methods of improving lifetime involve control of modulation strategies, switching frequency, and in case of parallel converters, power loss redistribution [23–27]. Furthermore, reactive current circulation [28], and active gate-driver control [29] are some other techniques with a potential to improve lifetime. These methods are not investigated in this thesis, and we focus solely on the cooling system.

Ma and Blaabjerg [30] compared the thermal performance in a three-level NPC converters with IGBT module, IGBT press-pack and IGCT press-pack packaging technologies. IGBT modules were shown to have the lowest losses and lowest temperature cycling compared to other two technologies. Furthermore, IGBT modules exhibit better insulation between the chip and the heat sink, are cheaper and easier to maintain [2, 30]. For these reasons, IGBT modules are more prevalent in renewable energy applications, and are thus analyzed in this thesis.

Lifetime evaluation of IGBT modules mostly falls under either a priori lifetime estimation or condition monitoring techniques [11, 16]. The former requires prior knowledge of loading patterns and system parameters, and is mainly done for an estimate of lifetime prior to deployment. The latter is more concerned with the real-time measurements, and monitoring aging in the modules. This thesis deals with the lifetime assessment prior to deployment.

Lifetime estimation during the design phase is a critical step in ensuring long term reliability [31]. The procedure mainly involves three stages. First, the calculation of the mean junction temperature and temperature cycles for all points on the mission profile is done. Then using the cycle counting algorithms, such as rainflow method, the total number of cycles corresponding to a particular amplitude for each mean temperature are estimated. And finally, the time at which the number of cycles approaches the number of cycles to failure is calculated. The approach has been adopted in various studies across applications [13, 32–36]. The same approach shall be adopted here. More details and literature on this is given in section 5.4.

All the aforementioned literature address certain aspects related to the lifetime analysis of power semiconductor devices. However, none of them have analyzed lifetime analysis in the context of comparing passive and active cooling systems in a submerged TST. Furthermore, assuming passive cooling system is inherently more reliable than the active cooled one, the objective is to study the feasibility of the passive system over active one. This thesis addresses these questions by means of investigating a TST system described in the following section.

5.3 System description

The lifetime of IGBT modules depends strongly on its loading mission profile [25]. Thus, defining site conditions and the turbine-generator-converter specifications are imperative to contextualize any obtained lifetime results. This section gives the main parameters required in the lifetime analysis.

5.3.1 Site conditions

The site conditions used in this chapter are exactly the same as defined in the previous chapter (Section 4.2), and hence will not be repeated here.

5.3.2 Turbine and Generator specifications

In the preceding chapter, a lifetime analysis of a fixed-pitch TST rated at 110 kW with a rated speed of 30 rpm was presented. Power regulation of the fixed-pitch turbine was achieved by the active speed stall mechanism. In this chapter, we compare the fixed-pitch turbine with a pitch-controlled turbine [5, 6, 37]. For comparison purposes, both turbines are rated at 110 kW, and have the same power-tidal speed curve shown in Figure 5.3. However, their rpm-tidal speed profiles are different, as seen in Figure 5.4. The maximum value of C_p for both the turbines is roughly 0.43, and thus they have the same power output even below the rated tidal stream speed.

The active speed stall-controlled turbine has the following $C_p - \lambda$ equation [37],

$$C_p(\lambda) = 0.000342\lambda^4 - 0.008056\lambda^3 + 0.046882\lambda^2 - 0.000434\lambda + 0.045225 \tag{5.1}$$

where, C_p is the power coefficient of the turbine and λ is the tip-speed ratio.

The pitch-controlled turbine has the following $C_p - \lambda$ relation,

$$C_p(\lambda,\beta) = 0.6\left(\frac{38}{\lambda_1} - 0.25\beta - 2\right) e^{\frac{-11}{\lambda_1}}$$
$$\frac{1}{\lambda_1} = \frac{1}{\lambda + 0.08\beta} - \frac{0.035}{\beta^3 + 1}, \tag{5.2}$$

where, β is the blade pitch angle. The $C_p - \lambda$ curve for the pitch-controlled turbine, and the pitch controller used here is similar to that of the 120 kW turbine studied in [38]. The maximum rate for the pitch controller is limited to $\pm$ 5° per second .

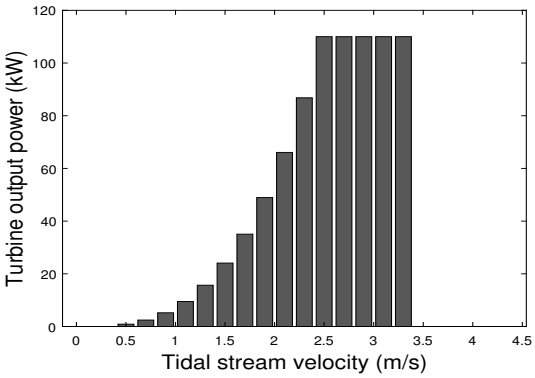

Figure 5.3 Power curve of the pitch and active speed (stall) [37] controlled tidal turbines as a function of tidal stream velocity.

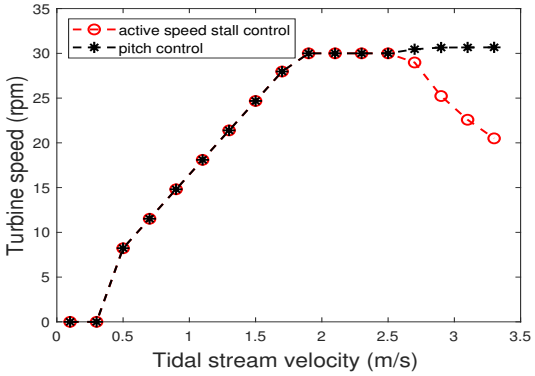

Figure 5.4 Speed curves of the pitch and active speed (stall) [37] controlled tidal turbines as a function of the tidal stream velocity.

For both turbines, the same generator is assumed, which is a direct-drive permanent magnet synchronous generator (PMSG). The parameters of this PMSG are listed in Table 5.1.

Table 5.1 Generator Parameters

Parameter	Value
Rated Power	110 kW
Rated speed	30 rpm
Pole pairs	40
No-load emf at 30 rpm	188 V
Resistance per phase	0.04 Ω
Synchronous inductance per phase	4 mH
Mass Moment of Inertia	6100 kg.m^2

Both turbines operate in the maximum power point tracking (MPPT) mode until they reach their rated speeds. In the MPPT region, the speed control is achieved by the constant K strategy explained in [39]. The required torque in the MPPT region is given obtained by:

$$T^* = K\omega_r^2, \tag{5.3}$$

where, K is a constant depending on factors such as nominal turbine speed and power, maximum value of power coefficient C_p, and the optimal tip-speed ratio, etc [39]. ω_r is the rotational speed of the turbine. Torque control is achieved by employing the classical PI control strategy in generator dq-axes. The q-axis current is obtained from the following equation:

$$i_q = \frac{T_e^*}{p\lambda_m} \tag{5.4}$$

where, p is the number of pole pairs of the generator, and λ_m is the magnetic flux linkage due to PM. If possible, d-axis current is kept at zero. Otherwise, flux weakening strategy is employed to ensure the required output voltage is deliverable from the converter [37, 40].

When the output power is greater than the rated power, the two turbines use different mechanisms to regulate the output power. The pitch-controlled turbine keeps operating at the rated speed, using the blade pitch angle to maintain the rated power [38]. On the other hand, in the stall-controlled turbine, the speed of the turbine is reduced to lower the C_p and keep the power at its rated value [37].

5.3.3 Converter specifications

The specifications of interest in the converter are the power loss and the thermal parameters of the IGBT modules and cooling system. In this section we give the specifications for the IGBT modules; cooling system specifications are given later in Section 5.5.

The loss parameters can be determined from the IGBT module datasheet. It is clear that the current rating of the IGBTs in the active stall-controlled turbine converter must be higher, owing to its lower rpm at rated power. For comparison purposes, we use the same IGBT module in the

pitch-controlled turbine as in the active stall-controlled one. In other words, Infineon's IGBT module FF600R12ME4 (1200V, 600 A) is selected in this study. The reason for selecting this particular switch is given in Section 4.3.3; IGBT parameters can also be found there.

5.4 Methodology

This section briefly describes how the lifetime of the IGBT module can be estimated based on the thermal cycling. The lifetime estimation basically involves the following steps:

1. Estimation of power loss in IGBT modules;
2. Thermal modeling of the IGBT modules; and
3. Lifetime estimation based on thermal cycling.

These three steps have been explained in Chapter 4. However, a short qualitative description is given here to facilitate reading.

5.4.1 Power loss

For this purpose, first the converter currents must be determined. The algorithm is summarised in Figure 5.5 [37].

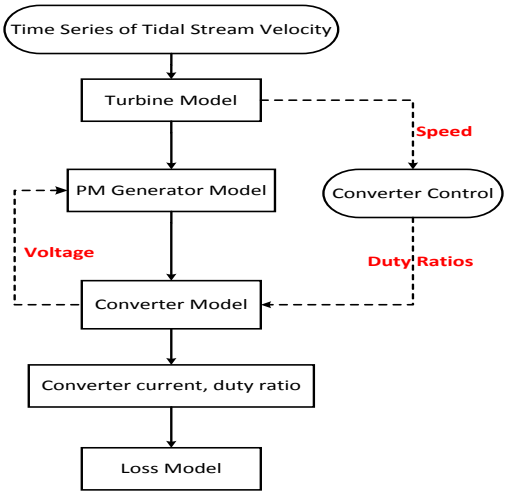

Figure 5.5 Calculating converter currents and duty ratios for loss calculation in IGBT modules; image adapted from [37].

IGBTs and diodes in a power module experience conduction and switching losses [13, 25]. Both of

these losses are a function of the junction temperature [41], as explained in Section 4.5. Figure 5.6 is repeated here from the previous chapter to recap the loss calculation. More details on the loss calculation can also be found in multiple references [13, 42, 43].

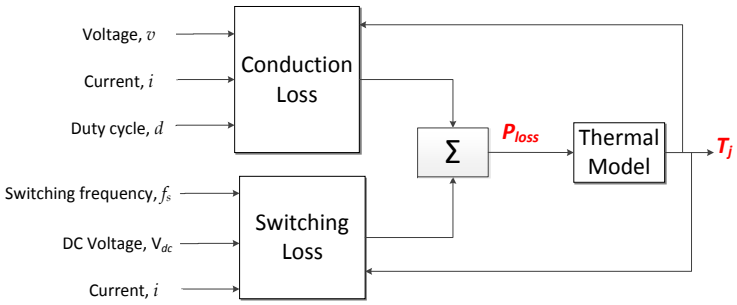

Figure 5.6 Loss calculation in IGBT and diode. The diagram shows that losses also depend on the junction temperature T_j, hence, the feedback loop from the thermal model. Equations for loss calculation are given in previous chapter (Section 4.5).

5.4.2 IGBT thermal modeling

From the power loss in the IGBT modules, thermal models are used to estimate the junction temperature (mean and amplitude). Thermal modeling must be performed for each operating point corresponding to Figure 5.3, in conjunction with the knowledge of turbulence and surface waves.

The thermal models for IGBT modules can be categorized into three types, namely, analytical, numerical and thermal network models [1]. Analytical models are primarily based on analytical solutions of the heat diffusion equation. These models are fast, but can only be applied for simple geometries and with simplified boundary conditions [44, 45]. Numerical models are based usually on finite element analysis, sometimes coupled with computational fluid dynamics (CFD) analysis [46, 47]. These models are extremely time consuming, and are unsuitable for dynamic electro-thermal simulations.

When it comes to using thermal models for lifetime analysis, thermal network models based on the RC elements appears to be the most favored one [37, 48–50]. Simplicity of these models, fast results and the possibility of combining RC elements of different components (especially in the Cauer form) into a combined RC network of the whole system are its main advantages [49, 50].

The main idea is to combine the RC thermal network of the IGBT modules (normally provided as Foster network parameters in datasheets) to the RC network of the heat sink (or cooling system) to form a complete thermal network of the system. This is described in Section 5.5.

5.4.3 Lifetime estimation

This is done using the lifetime models for the IGBT power modules as explained in the previous chapter, with the same set of assumptions. For active cooling systems, same methodology as adopted in [13] can be used.

After knowing the junction temperature values, the thermal fatigue accumulated for each operating point in Figure 5.3 is calculated. Multiplying the fatigue for each operating point with the probability of occurrence of each operating point, the net annual fatigue is calculated. From this information, the number of years to failure is estimated.

5.5 Thermal models for active and passive cooling systems

In this section a brief explanation of how the active (forced water cooling) and passive cooling systems are modeled into the thermal models for the IGBT modules in a submerged power converter is provided. Furthermore, the specifications of the two cooling systems are also presented, along with necessary assumptions made in the thermal models.

5.5.1 Forced water cooling

For the forced water cooling system, IGBT modules are mounted on a water cooled heat sink. The water is circulated in and out of the heat sink using a pump, as shown in Figure 5.2. Two different configurations of the forced cooling system are evaluated in this chapter:

- 6-pass system; and
- 4-pass system.

The reason for evaluating two different forced water cooling systems is to demonstrate that further improvement in lifetime is possible by overrating the heat sink. There is also a possibility of overrating a heat sink by increasing the flow rate of the coolant. However, the latter is not investigated here.

In the 6-pass system, three modules (each corresponding to one phase of the generator side converter) are mounted on a single heat sink. This is shown in Figure 5.7. In the 4-pass system, only one phase module is mounted on a single heat sink. The necessary thermal parameters corresponding to each of these cooling configurations are listed in Table 5.2. The heat sinks correspond to the commercial manufacturer Wakefield-Vette [51].

Figure 5.8 shows the thermal circuit for the IGBT module coupled with the water cooled heat sink. The combined Cauer-Foster network used in Figure 5.8 is based on [3, 52]. For simplification, uniform heat sink temperatures are assumed for all the modules (IGBTs as well as diodes) mounted on the same heat sink [43].

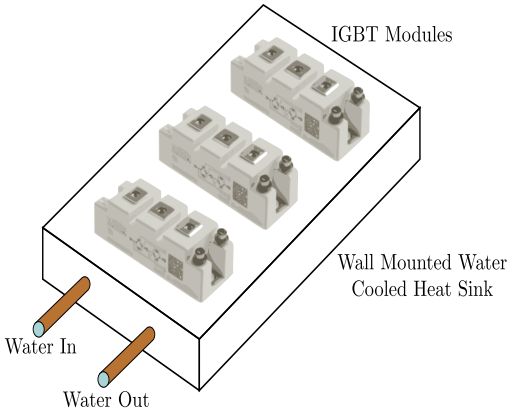

Figure 5.7 Three phase modules of the generator side converter mounted on a single water cooled heat sink (6-pass cold plate from Wakefield Vette). In the case of 4-pass cold plate, only one phase module is mounted on each cold plate.

Table 5.2 Forced water cooling parameters

Parameter	**Value**
6-pass cold plate	
No. of dual IGBT modules per heat sink	3
Rated fluid flow rate	5 litre/min
Fluid inlet temperature	15°C
Thermal resistance	0.01 K/W
Thermal capacitance	1930 W.s/K
Cold plate dimensions	0.304m x 0.177 m x 0.0152 m
4-pass cold plate	
No. of dual IGBT modules per heat sink	1
Rated fluid flow rate	5 litre/min
Fluid inlet temperature	15°C
Thermal resistance	0.02 K/W
Thermal capacitance	690 W.s/K
Cold plate dimensions	0.152m x 0.127 m x 0.0152 m

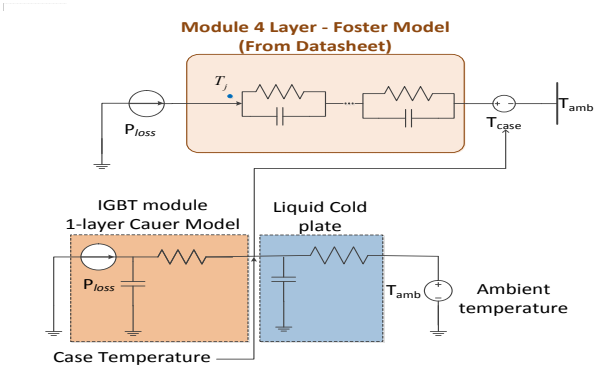

Figure 5.8 Thermal circuit for determining IGBT and diode junction temperatures in an actively cooled converter. From [3].

5.5.2 Passively cooled system

Figure 5.9 shows the placement of the switches in the passively cooled converter. Each module corresponds to a phase leg of the generator side converter, and is mounted on a separate mounting plate. The mounting plate is made of a thermally conductive material such as copper [3]. The dimensions of the mounting plate are listed in Table 5.3. The system used here is the same as in the previous chapter, where the modeling of the passively cooled system can also be found.

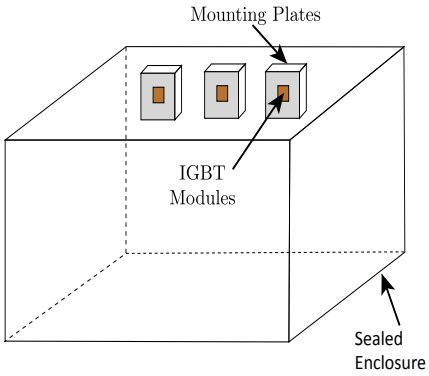

Figure 5.9 Three phase IGBT modules for Generator side converter mounted on the inner walls of the submerged enclosure via a copper mounting plate. The copper mounting plate minimizes the thermal spreading resistance [3].

Table 5.3 Passive water cooling parameters

Parameter	Value
Enclosure wall thickness	0.010 m
Enclosure height	1.5 m
Enclosure width	0.5 m
Enclosure length	1.5 m
Cu mounting plate dimensions	0.171 m x 0.330 m
Cu mounting plate thickness	0.020 m
Thermal resistance (function of heat loss) including thermal paste	0.05-0.13 K/W [37]
Thermal capacitance	7862 W.s/K

There is an important point of difference between the active and the passive cooling systems. Whereas in active cooling system, R_{c-a} (case-to-ambient thermal resistance) is assumed to be constant, same cannot be done in passively cooled system. The reason is that the external convective heat transfer coefficient in Figure 5.10 is a function of the heat flux from the IGBT power module [3, 53], as explained in the previous chapter. As a result, the spreading thermal resistances in the enclosure frame and the mounting plate are modeled as variable resistances in Figure 5.10 [3, 54].

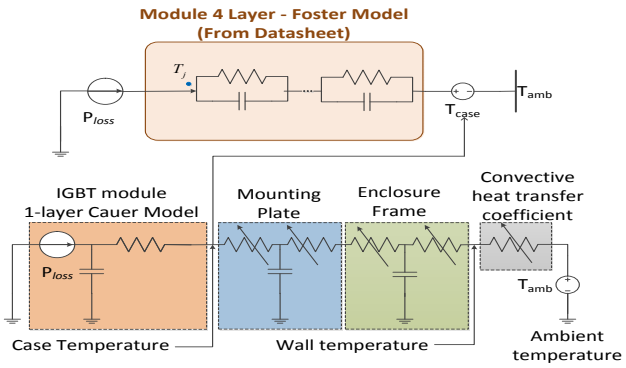

Figure 5.10 Thermal circuit for determining IGBT and diode junction temperatures in a passively cooled converter. From [3].

Furthermore, the area footprint of the forced cooling heat sink appears smaller than the passively cooled converter. However, the auxiliary system such as pumps, condenser in the former occupy

space elsewhere.

5.6 Case Study: Lifetime analysis of 110 kW tidal turbines

In this section we compare the cooling systems in the submerged power converter for 110 kW tidal turbines described in Section 5.3. The analyses is divided into two parts. Section 5.6.1 compares different cooling systems in terms of mean junction temperatures, temperature cycling amplitudes, lifetime of the IGBT modules and annual losses in the IGBT modules for the active stall-controlled tidal turbine. On the other hand, section 5.6.2 compares the IGBT lifetimes in pitch-controlled and active stall-controlled turbines. In both cases, lifetime of the IGBT modules is taken to be the lifetime of the diodes in the generator side converter. This is because the lifetime of the diodes on the generator side converter is the minimum of all IGBTs and diodes in the back-to-back converter shown in Figure 4.10 [37].

5.6.1 Comparison of different cooling systems

Figure 5.11 demonstrates the speed variation of the generator as a consequence of the variation in the tidal stream velocity for the active speed stall-controlled turbine. Because the velocity at all times in Figure 5.11 is greater than the rated speed of 2.5 m/s, the generator power is maintained at 110 kW. Consequently, the rise and fall in the generator speed is reflected by the fall and rise in the rms value of the generator phase currents, as seen in Figure 5.12.

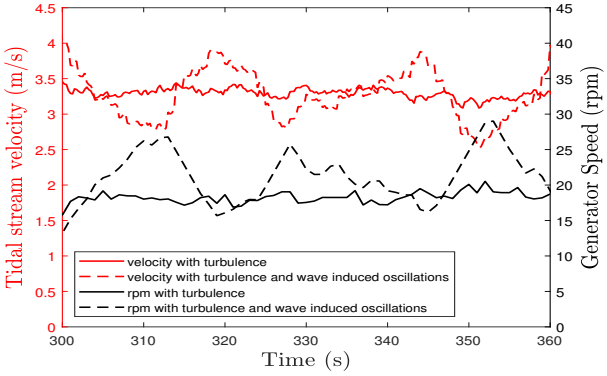

Figure 5.11 Active speed stall control of generator speed as a function of change in tidal stream velocity. Mean tidal velocity in this image is set at 3.3 m/s [37]. This figure is repeated from the previous chapter for easier readability.

Figure 5.13 shows the estimated lifetime for the IGBT modules (including the effects of turbulence) with and without the impact of surface waves for different cooling systems. Clearly, forced water cooling systems show significantly improved lifetime values over passive cooling systems.

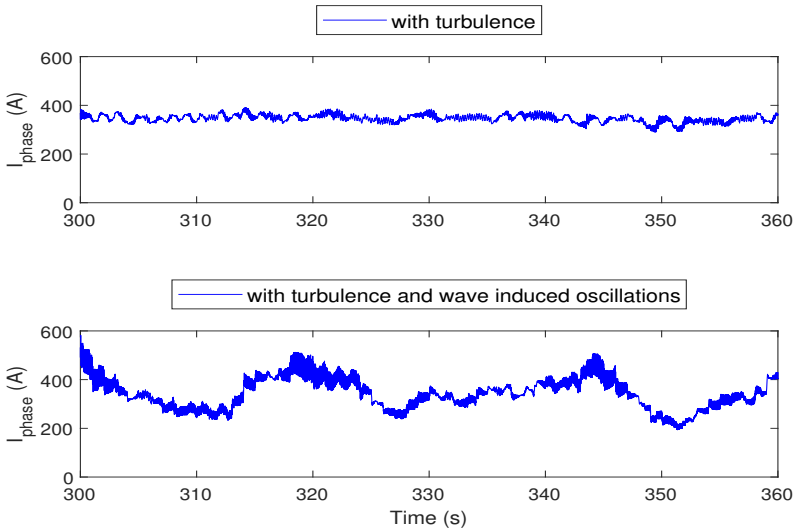

Figure 5.12 Generator phase currents (rms values). The variations in the phase current value is a direct consequence of the generator speed variations in Figure 5.11. This also illustrates why IGBT module with 600 A rating was selected in this thesis. The above graph would have depicted a flat line (about 380 A) without any velocity oscillations.

However, this increase in lifetime reduces when waves are also considered, in addition to the turbulence.

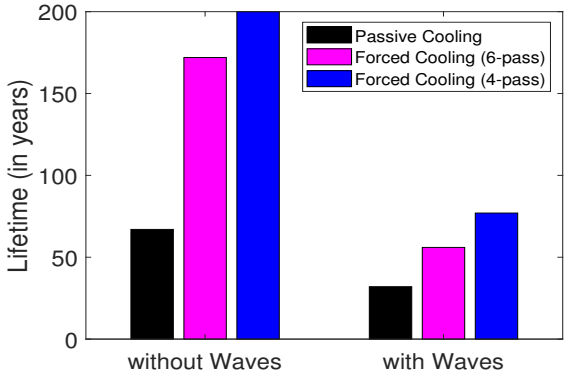

Figure 5.13 Estimated lifetime of the IGBT modules on the generator side converter with different cooling systems.

Even though there seems to be a significant difference in the lifetime, the annual IGBT module losses in the generator side converter do not seem to be that different. This can be seen in Table

5.4. The losses in the passive cooling system are higher because higher junction temperatures also mean more losses in the IGBT modules. Figure 5.14 shows the mean junction temperatures as a function of the tidal stream velocity. Passive cooling system has a higher thermal resistance compared to the forced water cooling systems. Therefore, similar magnitude of losses result in higher temperature in the passive cooling system.

There is not much difference between the mean temperatures of 4-pass and 6-pass cooling systems, except at higher tidal velocities. The difference in lifetimes of 6-pass and 4-pass cooling systems is because bulk lifetime consumption also occurs at higher tidal velocities. This is shown in Figure 5.15. This predominant lifetime consumption at high velocities is a consequence of the active stall control mechanism. In active stall control strategy, at higher tidal velocities rated power is delivered at lower rpm and higher currents. This means more losses in the IGBT modules, and hence more lifetime consumption. In other words, lifetime consumption below rated tidal speed can be neglected.

Table 5.4 Annual loss in the generator side converter for passive and active cooling systems, without waves

Cooling system	IGBTs Loss (in MWh)	Diodes Loss (in MWh)
Passive Cooling	2.11	2.53
Forced water cooling (6-pass cold plate)	1.90	2.36
Forced water cooling (4-pass cold plate)	1.89	2.35

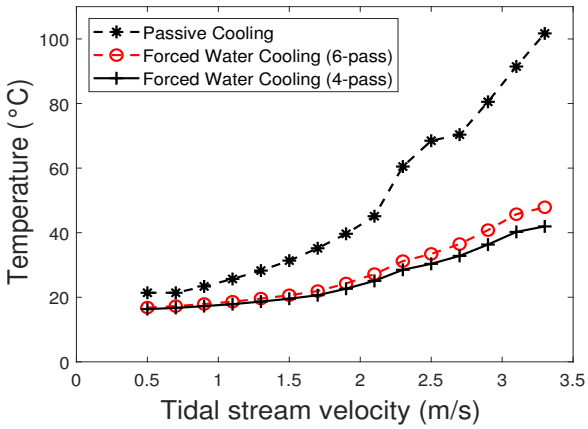

Figure 5.14 Comparison of mean junction temperatures between different cooling systems as a function of tidal stream velocity. Data for passive cooling is taken from [37].

Figures 5.16 and 5.17 show the diode junction temperature variation corresponding to the velocity

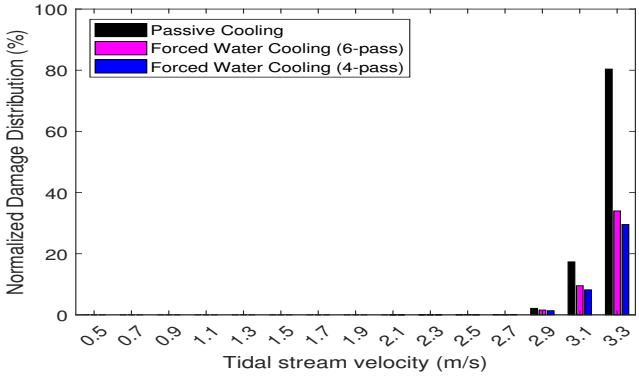

Figure 5.15 Annual damage distribution between different cooling systems as a function of tidal stream velocity. The values are normalized w.r.t annual damage in passively cooled systems. More annual damage can be seen in passive cooling systems. Lifetime consumption mostly happens at higher tidal velocities.

variations in Figure 5.11. The amplitude of thermal cycling appears similar in all the three cases. Although passive systems have higher thermal time constant for the heat sink, for cycling of the junction temperature IGBT and diode thermal capacitances are more influential.

From the above discussion we conclude that the difference in lifetime for different cooling systems is primarily due to the difference in mean junction temperatures, and not so much due to the amplitude of thermal cycling. This is shown more clearly in Figure 5.18. However, when considering the same cooling system, the lifetime reduction from waves is due to the higher amplitude of thermal cycling.

5.6.2 Comparing active speed stall and pitch control

Here we compare the lifetime of IGBT modules in active stall and pitch-controlled turbines. This analysis has only been done considering the forced water cooling (6-pass coldplate) system. Table 5.5 shows the lifetime values for converters in pitch and active stall-controlled turbines. Lifetime values in pitch-controlled turbine are large because the device (IGBT) selection was done considering the active stall control (i.e. at high rms current values). Main reason for this is the lower mean junction temperature and temperature cycling experienced in the pitch-controlled turbine converter, especially at tidal velocities greater than the rated velocity, see Figure 5.19. Another conclusion that can be drawn from the lifetime in pitch-controlled turbine is that IGBT overrating could also be used to improve the lifetime.

For the similar power rating and turbine size, pitch-controlled turbines draw lower phase current above rated speed because of the smaller oscillations and higher mean value of the generator speed, see Figures 5.20 and 5.21. Consequently, diode junction temperature has lower mean value, and lower amplitude of temperature cycling as seen in Figure 5.22. Another point to note

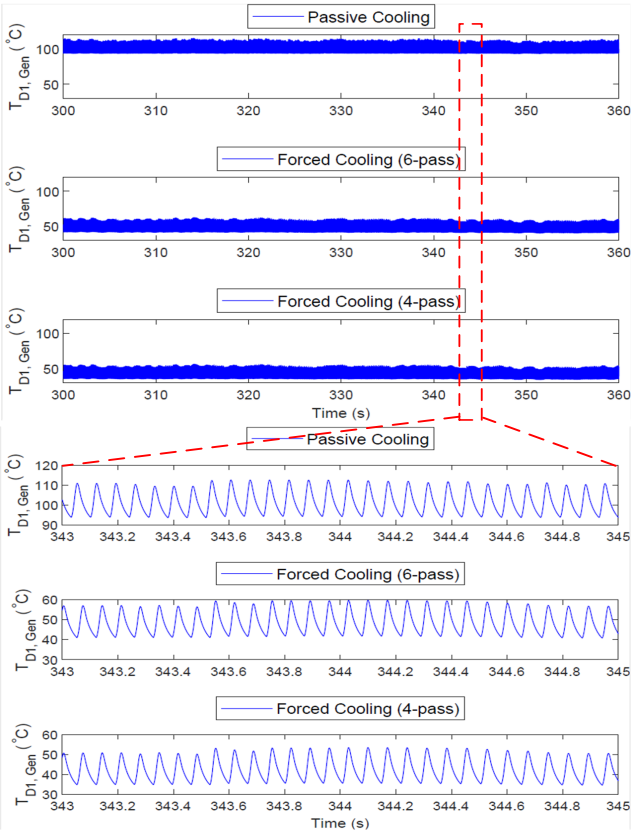

Figure 5.16 Comparison of cooling systems in terms of diode junction temperature cycling considering only turbulence in tidal stream velocity shown in Figure 5.11. This plot only corresponds to a time duration of 60 s under certain turbulence conditions. Results at different time instants and different values of mean tidal velocity and turbulence will give different values.

is the distribution of the lifetime damage w.r.t tidal stream velocity in active speed stall and pitch-controlled turbines as shown in Figure 5.23.

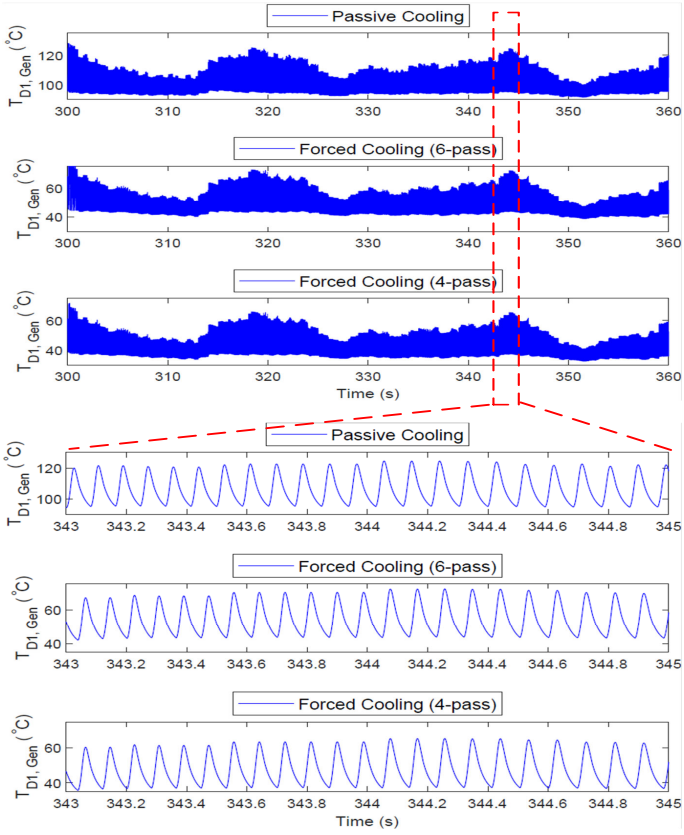

Figure 5.17 Comparison of cooling systems in terms of diode junction temperature cycling considering both turbulence and waves in tidal stream velocity shown in Figure 5.11.

Table 5.5 IGBT lifetime comparison between active speed stall-controlled and pitch-controlled turbines.

Turbine	**Lifetime (in years)**
Active speed stall control	55
Pitch control	30×10^3

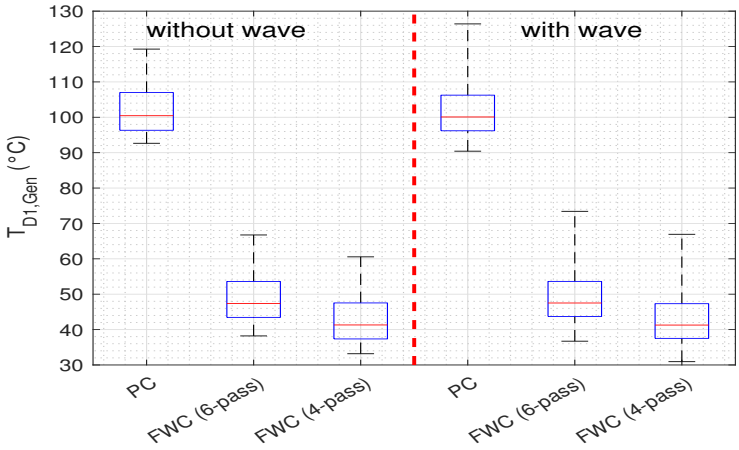

Figure 5.18 Diode junction temperature swing for different cooling systems at mean velocity of 3.3 m/s, and TI value of 13%. Difference in minimum and maximum temperature is shown without waves and with a wave of H_s = 5.75 m, and T_p = 11 s. For different cooling systems with same wave conditions, we see that the temperature swing is nearly same albeit with difference in mean temperatures. However, for the same cooling system, with and without waves the mean temperature is same but with difference in temperature swing. PC—Passive cooling; FWC—Forced water cooling.

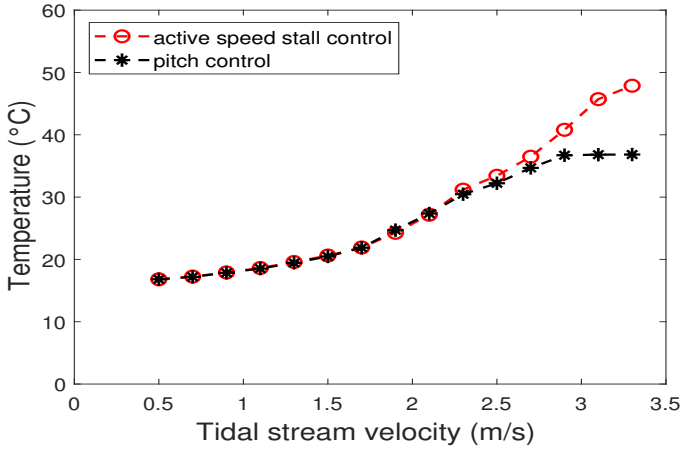

Figure 5.19 Mean junction temperatures of the diode (in the generator side converter) as a function of tidal stream velocity. Both turbines deliver same power, albeit at different generator speeds. Below 2.5 m/s active stall-controlled turbine operates at higher speed, and thus has lower temperature. Above 2.5 m/s pitch-controlled turbine runs at higher speed, see Figure 5.4.

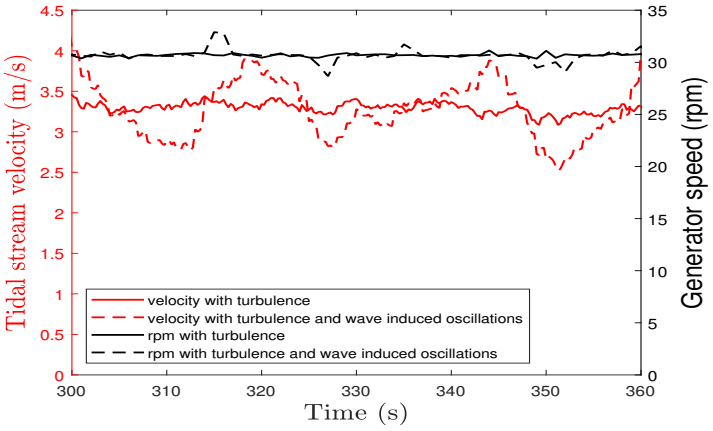

Figure 5.20 Variation of generator speed as a function of change in tidal stream velocity in a pitch-controlled turbine. Compare this with the generator speed variations in Figure 5.11.

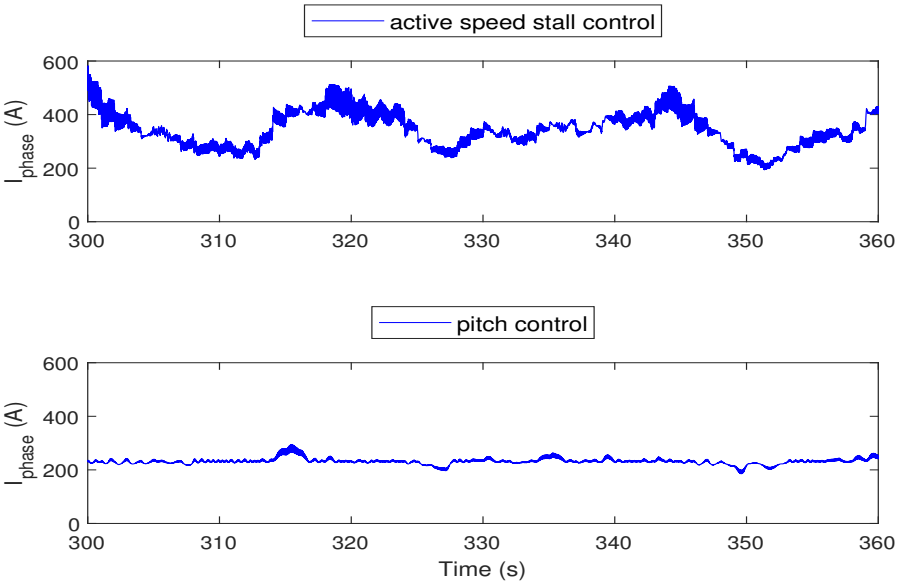

Figure 5.21 Generator phase currents (rms values) in the active speed stall and the pitch-controlled turbine, under the influence of turbulence and wave induced tidal stream velocity oscillation (as shown in Figure 5.11).

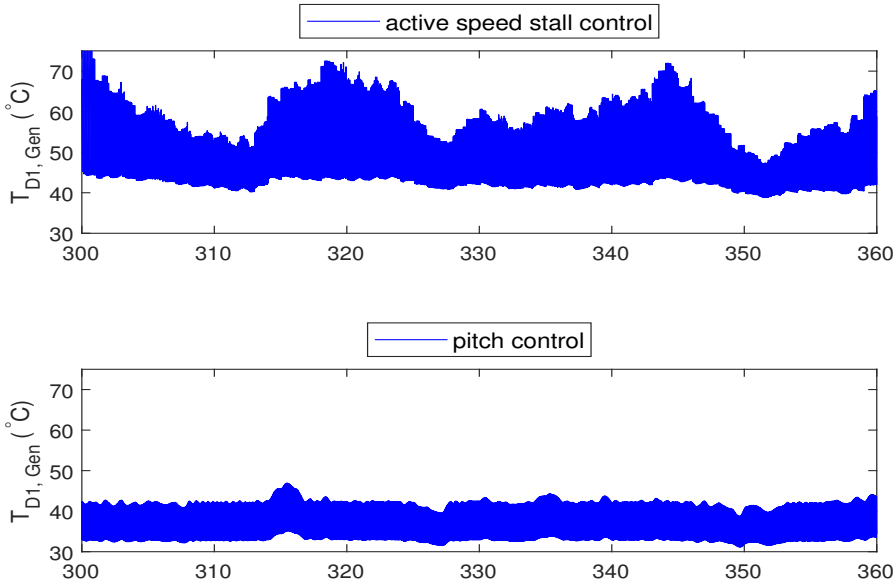

Figure 5.22 Comparison of the diode junction temperatures in turbines with active stall control and pitch control. It is clearly seen that pitch control mitigates the diode temperature cycling by maintaining nearly the same current even under significant wave induced oscillations by virtue of maintaining nearly the same generator speed.

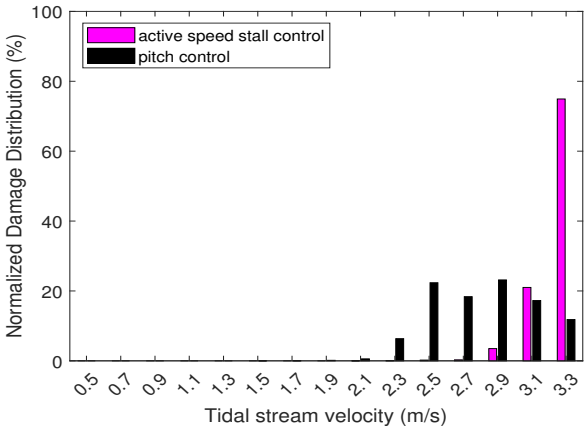

Figure 5.23 Damage distribution in active stall-controlled and pitch-controlled turbines (each normalized to 100%). Overall IGBT lifetime in the pitch-controlled turbine is much higher than in the active stall-controlled turbine. Whereas the lifetime consumption is concentrated at higher tidal velocities in active stall-controlled turbine, it is more distributed in pitch-controlled turbine. The cooling system used in each case is the forced water cooling (6-pass) system.

5.7 Conclusion

This chapter compared active and passive cooling systems in TST converters on the basis of estimated lifetime of IGBT power modules. Different cooling systems were compared for the active speed stall-controlled turbine. The comparison assumed thermal cycling as the main failure mode in IGBT modules. Results indicate that forced water cooling (active) system can yield significant improvement in the lifetime of IGBT modules over passive systems. This improvement is primarily due to the decrease in mean junction temperature of the IGBT modules rather than the decrease in the amplitude of thermal cycling. The amplitude of the thermal cycling was almost the same in both cooling systems for the power frequency. This implies cycling is mostly determined by the IGBT thermal capacitance, and not the capacitance of the heat sink. Overrating forced water cooling systems, e.g. by using larger heat sink, can further improve lifetime. In active stall-controlled TSTs, bulk of the lifetime consumption happens at higher velocities.

In contrast, lifetime of the IGBT modules increases significantly when pitch control is used instead of the active stall control in a similarly rated turbine. In pitch-controlled turbines, lifetime damage is more widespread rather than just being concentrated at higher tidal velocities. These conclusions hold true for both active and passive cooling systems. Passive cooling system is inherently more reliable due to the lack of any moving parts, but it comes at the cost of reduced lifetime.

Bibliography

[1] C. Qian, A. Gheitaghy, J. Fan, H. Tang, B. Sun, H. Ye and G. Zhang, "Thermal management on IGBT power electronic devices and modules", *IEEE Access*, vol. 6, pp. 12868–12884, 2018.

[2] A. Wintrich, U. Nicolai, W. Tursky and T. Reimann, "Application manual power semiconductors", SEMIKRON International GmbH, 2015. [Online] https://www.semikron.com/dl/service-support/downloads/download/semikron-application-manual-power-semiconductors-english-en-2015/, [Last accessed: 10 Jan 2020].

[3] F. Wani, U. Shipurkar, J. Dong and H. Polinder, "A study on passive cooling in subsea power electronics", *IEEE Access*, vol. 6, 67543–67554, 2018.

[4] D. Toma, A. Mànuel-Làzaro, M. Nogueras and J. Del Rio, "Study on heat dissipation and cooling optimization of the junction box of OBSEA seafloor observatory", *IEEE/ASME Transactions on Mechatronics*, vol. 20, pp. 1301–1309, 2014.

[5] B. Whitby, and C. E. Ugalde-Loo, "Performance of pitch and stall regulated tidal stream turbines", *IEEE Transactions on Sustainable Energy*, vol. 5, pp. 64–72, 2014.

[6] H. Polinder, D. Bang, R. Van Rooij, A. McDonald and M. Mueller, "10 MW wind turbine direct-drive generator design with pitch or active speed stall control", in *Proceedings of the IEEE International Electric Machines and Drives Conference*, Antalya, Turkey, 3–5 May 2007, pp. 1390–1395.

[7] F. Wani and H. Polinder, "A Review of Tidal Current Turbine Technology: Present and Future", in *Proceedings of the 12th European Wave and Tidal Energy Conference (EWTEC 2017)*, Cork, Ireland, 2017, pp. 1133-1–10. ISSN 2309-1983.

[8] J. Carroll, A. McDonald, D. McMillan, "Reliability comparison of wind turbines with DFIG and PMG drive trains", *IEEE Transactions on Energy Conversion*, vol. 30, pp. 663–670, 2015.

[9] F. Spinato, P. Tavner, G. van Bussel, E. Koutoulakos, "Reliability of wind turbine subassemblies", *IET Renewable Power Generation*, vol.3, no. 4, pp. 387–401, 2009.

[10] CATAPULT, "Portfolio Review 2016: System performance, availability and reliability trends analysis (SPARTA)," 2016. [Online] https://s3-eu-west-1.amazonaws.com/media.ore.catapult/wp-content/uploads/2017/03/28102600/SPARTAbrochure_20March-1.pdf, [Last accessed: 15 Apr 2020].

[11] S. Yang, D. Xiang, A. Bryant, P. Mawby, L. Ran and P. Tavner, "Condition monitoring for device reliability in power electronic converters: A review", *IEEE Transactions on Power Electronics*, vol. 25, no. 11, pp. 2734–2752, 2010.

[12] K. Fischer, K. Pelka, S. Puls, M. Poech, A. Mertens, A. Bartschat, B. Tegtmeier, C. Broer and J. Wenske, "Exploring the causes of power-converter failure in wind turbines based on comprehensive field-data and damage analysis", *Energies*, vol. 12, no. 4, p. 593, 2019.

[13] U. Shipurkar, E. Lyrakis, K. Ma, H. Polinder and J. Ferreira, "Lifetime comparison of power semiconductors in three-level converters for 10MW wind turbine systems", *IEEE Journal of Emerging and Selected Topics in Power Electronics*, vol. 6, no. 3, pp. 1366–1377, 2018.

[14] U. Choi, F. Blaabjerg, F. Iannuzzo and S. Jørgensen, "Junction temperature estimation method for a 600 V, 30 A IGBT module during converter operation", *Microelectronics Reliability*, vol. 15, no. 9, pp. 2022–2026, 2015.

[15] K. Ma, F. Blaabjerg and M. Liserre, "Thermal analysis of multilevel grid-side converters for 10-MW wind turbines under low-voltage ride through", *IEEE Transactions on Industrial Applications*, vol. 49, no. 2, pp. 909–921, 2013.

[16] Z. Hu, X. Ge, D. Xie, Y. Zhang, B. Yao, J. Dai and F. Yang, "An aging-degree evaluation method for IGBT bond wire with online multivariate monitoring", *Energies*, vol. 12, no. 20, p. 3962, 2019.

[17] Y. Hu, P. Shi, H. Li and C. Yang, "Health condition assessment of base-plate solder for multi-chip IGBT module in wind power converter", *IEEE Access*, vol. 7, pp. 72134–72142, 2019.

[18] A. De Rijck and H. Huisman, "Power semiconductor device adaptive cooling assembly", US Patent 8,547,687, 2013. [Online] https://patentimages.storage.googleapis.com/cf/bf/f1/f8fd4113102d38/US8547687.pdf, [Last accessed: 05 Apr 2020].

[19] U. Shipurkar, *Improving the availability of wind turbine generator systems*, PhD dissertation, Delft University of Technology, 2019.

[20] Y. Yerasimou, V. Pickert, B. Ji and X. Song, "Liquid metal magnetohydrodynamic pump for junction temperature control of power modules", *IEEE Transactions on Power Electronics*, vol. 33, no. 12, pp. 10583–10593, 2018.

[21] U. Choi and J. Lee, "Comparative evaluation of lifetime of three-level inverters in grid-connected photovoltaic systems", *Energies*, vol. 13, no. 5, p. 1227, 2020.

[22] K. Rajashekara, H. Krishnamoorthy and B. Naik, "Electrification of subsea systems: requirements and challenges in power distribution and conversion", *CPSS Trans. Power Electron. Appl.*, vol. 2, no. 4, pp. 259–266, 2017.

[23] M. Andresen, K. Ma, G. Buticchi, J. Falck, F. Blaabjerg and M. Liserre, "Junction temperature control for more reliable power electronics", *IEEE Transactions on Power Electronics*, vol. 33, no. 1, pp. 765–776, 2017.

[24] G. Chen and X. Cai, "Adaptive control strategy for improving the efficiency and reliability of parallel wind power converters by optimizing power allocation", *IEEE Access*, vol. 6, pp. 6138–6148, 2018.

[25] M. Weckert and J. Roth-Stielow, "Chances and limits of a thermal control for a three-phase voltage source inverter in traction applications using permanent magnet synchronous or induction machines", in *Proceedings of the 14th European Conference on Power Electronics and Applications, IEEE*, Birmingham, UK, Aug 30-Sep 1, 2011, pp. 1–10.

[26] K. Ma and F. Blaabjerg, "Thermal optimised modulation methods of three-level neutral-point-clamped inverter for 10 mw wind turbines under low-voltage ride through", *IET Power Electronics*, vol. 5, no. 6, pp. 920–927, 2012.

[27] M. Andresen, J. Kuprat, V. Raveendran, J. Falck and M. Liserre, "Active thermal control for delaying maintenance of power electronics converters", *Chinese Journal of Electrical Engineering*, vol. 4, pp. 13–20, 2018.

[28] K. Ma, M. Liserre and F. Blaabjerg, "Reactive power influence on the thermal cycling of multi-MW wind power inverter", *IEEE Transactions on Industrial Applications*, vol. 49, no. 2, pp. 922–930, 2013.

[29] L. Wu and A. Castellazzi, "Temperature adaptive driving of power semiconductor devices", in *2010 IEEE International Symposium on Industrial Electronics*. IEEE, 2010, pp. 1110–1114.

[30] K. Ma and F. Blaabjerg, "The impact of power switching devices on the thermal performance of a 10 MW wind power NPC converter", *Energies*, vol. 5, no. 7, pp. 2559–2577, 2012.

[31] Y. Yang, H. Wang, A. Sangwongwanich and F. Blaabjerg, "Design for reliability of power electronic systems". In *Power electronics handbook*. Elsevier, 2018, pp.1423–1440.

[32] K. Ma, M. Liserre, F. Blaabjerg and T. Kerekes, "Thermal loading and lifetime estimation for power device considering mission profiles in wind power converter", *IEEE Transactions on Power Electronics*, vol. 30, no. 2, pp. 590–602, 2014.

[33] K. Givaki, M. Parker and P. Jamieson, "Estimation of the power electronic converter lifetime in fully rated converter wind turbine for onshore and offshore wind farms", in *Proceedings of IET Power Electronics, Machines and Drives (PEMD 2014)*, Manchester, UK, 8-10 April, 2014.

[34] M. Denk and M. Bakran, "Comparison of counting algorithms and empiric lifetime models to analyze the load-profile of an IGBT power module in a hybrid car", in *Proceedings of the IEEE 2013 3rd International Electric Drives Production Conference (EDPC)*, Nuremberg, Germany, 29-30 October 2013; pp. 1–6.

[35] Y. Wang, S. Jones, A. Dai and G. Liu, "Reliability enhancement by integrated liquid cooling in power IGBT modules for hybrid and electric vehicles", *Microelectronics Reliability*, vol.54, no. 9, pp. 1911–1915, 2014.

[36] M. Thoben, F. Sauerland, K. Mainka, S. Edenharter and L. Beaurenaut, "Lifetime modeling and simulation of power modules for hybrid electrical vehicles", *Microelectronics Reliability*, vol.54, no. 9, 1806–1812, 2014.

[37] F. Wani, U. Shipurkar, J. Dong, H. Polinder, A. Jarquin-Laguna, K. Mostafa and G. Lavidas, "Lifetime analysis of IGBT power modules in passively cooled tidal turbine converters", *Energies*, vol. 13, no. 8, p. 1875, 2020.

[38] G. Lavidas and V. Venkatesan, "Integrated design and implementation of 120-kW horizontal-axis tidal current energy conversion system", *Ocean Engineering.*, vol. 158, pp. 684–703, 2018.

[39] M. Jahromi, A. Maswood and K. Tseng, "Design and evaluation of a new converter control strategy for near-shore tidal turbines", *IEEE Transactions on Industrial Electronics*, vol. 60, no. 12, pp. 5648–5659, 2012.

[40] Z. Zhou, F. Scuiller, J. F. Charpentier, M. Benbouzid and T. Tang, "Power control of a non-pitchable PMSG-based marine current turbine at overrated current speed with flux-weakening strategy", *IEEE Journal of Oceanic Engineering*, vol. 40, pp. 536–545, 2015.

[41] I. Technologies, "IGBT Modules." [Online] https://www.infineon.com/cms/en/product/power/igbt/igbt-modules/, [Last accessed: 10 Jan 2020].

[42] Z. Zhou, M. Khanniche, P. Igic, S. Kong, M. Towers and P. Mawby, "A fast power loss calculation method for long real time thermal simulation of IGBT modules for a three-phase inverter system", in *Proceedings of European Conference on Power Electronics and Applications*, Dresden, Germany, 11-14 September, 2005.

[43] J. Lemmens, P. Vanassche and J. Driesen, "Optimal control of traction motor drives under electrothermal constraints", *IEEE Journal of Emerging and Selected Topics in Power Electronics* vol. 2, no. 2, pp. 249–263, 2014.

[44] M. Musallam and C. M. Johnson, "Real-time compact thermal models for health management of power electronics", *IEEE Transactions on Power Electronics*, vol. 25, pp. 1416–1425, 2010.

[45] J. Reichl, J. M. Ortiz-Rodriguez, A. Hefner, J. S. Lai, "3D thermal component model for electrothermal analysis of multichip power modules with experimental validation", *IEEE Transactions on Power Electronics*, vol. 30, no. 6, pp. 3300–3308, 2014.

[46] M. Riccio, G. De Falco, L. Maresca, G. Breglio, E. Napoli, A. Irace, Y. Iwahashi and P. Spirito, "3D electro-thermal simulations of wide area power devices operating in avalanche condition", *Microelectronics Reliability*, vol. 52, no. 9, pp. 2385–2390, 2012.

[47] S. Xu, Y. Peng and S. Li, "Application thermal research of forced-air cooling system in high-power NPC three-level inverter based on power module block", *Case Studies in Thermal Engineering*, vol. 8, pp. 387–397, 2016.

[48] C. S. Yun, P. Malberti, M. Ciappa and W. Fichtner, "Thermal component model for electrothermal analysis of igbt module systems", *IEEE Transactions on Advanced Packaging*, vol. 24, no. 3, pp. 401–406, 2001.

[49] K. Ma, "Electro-thermal model of power semiconductors dedicated for both case and junction temperature estimation", Power Electronics for the Next Generation Wind Turbine System. Springer, 2015, pp. 139–143.

[50] Z. Luo, H. Ahn and M. Nokali, "A thermal model for insulated gate bipolar transistor module", *IEEE Transactions on Power Electronics*, vol. 19, no. 4, pp. 902–907, 2004.

[51] Wakefield-vette, “Exposed Tube Liquid Cold Plates,” Technical Report, 2016. [Online] https://eu.mouser.com/datasheet/2/433/Wakefield-Vette_Exposed_Tube_Liquid_Cold_Plates_Fi-1500597.pdf, [Last accessed: 25 Mar 2020].

[52] K. Ma, Y. Yang and F. Blaabjerg, "Transient modelling of loss and thermal dynamics in power semiconductor devices", in *Proceedings of Energy Conversion Congress and Exposition (ECCE)*, Pittsburg, PA, USA, 2014; pp. 5495–5501.

[53] Y. A. Cengel and J. Ghajar. *Heat and Mass Transfer, Fundamentals & Application, Fifth Edition in SI Units*; McGraw-Hill New York, NY, USA, 2014.

[54] Y. Muzychka, J. Culham and M. Yovanovich, "Thermal spreading resistance of eccentric heat sources on rectangular flux channels", *Journal of Electronic Packaging*, vol. 125, no. 2, pp. 178–185, 2003.

CHAPTER 6

Flooded Generator Design-I : Electromagnetic Model

This chapter is the first of the series of two chapters on design of permanent magnet flooded generators. The concept of the flooded generator was introduced under the section "Possible future trends in power take-off design" in chapter 2. This chapter addresses the flooded generator design from the electromagnetic perspective. Primarily the focus is to demonstrate the additional losses that can occur in a flooded generator compared to a conventional airgap generator.
A brief description about the prototype flooded generator developed under the TiPA project is also given.

Based on:

- F. Wani, U. Shipurkar, J. Dong and H. Polinder, "Calculation of PWM-Induced Rotor-Can Losses in Flooded Generator," in *13th European Wave and Tidal Energy Conference (EWTEC'19)*, Napoli, Italy, 2019, ISSN 2309-1983, pp. 1451-1-6.
- F. Wani, J. Dong, A. Yadav and H. Polinder, "Fast Rotor Loss Calculations in Fractional-Slot Permanent Magnet Machines," in *13th International Conference on Electric Machines (ICEM'18)*, Alexandroupolis, Greece, 2018, pp. 1201–1206.

Abstract

The main point of difference between a flooded and a conventional airgap generator is the presence of water instead of air in the stator-rotor gap of the generator. This necessitates the presence of stator and rotor sleeves in the flooded generator. In case either or both of these sleeves are electrically conductive, the generator performance may significantly differ from a similarly sized airgap generator. This chapter presents the electromagnetic model for the flooded generator. The focus is primarily on the estimation of additional electromagnetic losses, if any, in the stator and rotor sleeves. An insight into these losses is indispensable in selecting the materials for the stator and the rotor sleeves. In this context, eddy current losses in the rotor sleeve are identified as an important component of the total loss. Consequently, the bulk of this chapter is allocated to calculating these losses, and especially developing faster methods to do so, which can be employed in design optimization studies.
This chapter ends with a brief description of the prototype flooded generator. The prototype generator was developed as part of the TiPA project, to which this thesis also contributed.

6.1 Introduction

Generators for tidal turbines are usually placed in a nacelle sealed by a high pressure rotary mechanical seal. Over time the leakage from the mechanical seals may cause generator malfunction due to corrosion, insulation failure, etc. To avoid such failures, some tidal turbines employ a bilge pump inside the nacelle, which is accompanied by dehumidifying systems. This adds to the cost, and potentially introduces additional reliability issues, for the power take-off (PTO) system. In order to minimize failure modes, a flooded permanent magnet (PM) generator has been proposed in literature [1, 2]. A flooded generator—also known as the wetgap generator—is where the stator-rotor gap of the generator is filled with sea water. To further improve the efficiency and reliability, direct-drive PM generators are preferred over other generator types [3].

Figure 6.1 shows a representation of a flooded generator. Figure 6.2 compares a conventional airgap generator with the flooded generator. In flooded generators, protective sleeves (or *cans*) on the rotor and the stator surfaces in the watergap[1] are necessary to prevent corrosion in magnets and iron, and insulation failure in the stator winding. The presence of stator and the rotor sleeves is mainly what distinguishes a flooded generator from a conventional generator.

The sleeve materials must ideally be corrosion resistant, have low electrical and high thermal conductivity, along with strong water-repellent properties. In literature, examples of both metallic and non-metallic materials for stator and rotor sleeves can be found [1, 2, 4, 5].

If electrically conductive, stator sleeve would experience losses due to the magnets as well as the stator currents, whereas rotor sleeve loss would be predominantly because of the stator currents. Furthermore, sleeve overhang is more on the stator side due to the end-windings, which may also increase losses in the stator sleeve [6]. This does not mean that designs with metallic stator

[1] because the gap is filled with water in lieu of air

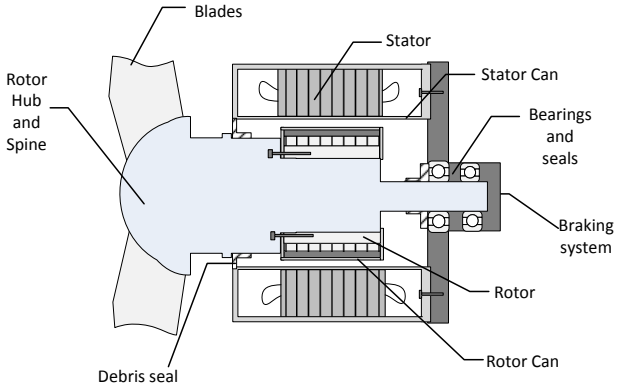

Figure 6.1 A representative figure of a flooded generator; only necessary details for discussion are shown here.

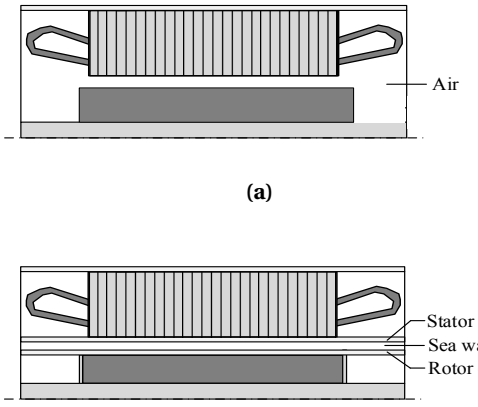

Figure 6.2 Axial cross-section of (a) a sealed airgap generator , and (b) a flooded generator with stator and rotor sleeves.

sleeves are never used. In fact, canned motors have in the past invariably used metallic materials on the stator sleeve. In some applications, materials such as 316 Stainless steel or Hastealloy 276, still continue to be used [7]. However, these days materials such as carbon fibre or glass fibre can offer adequate protection against water ingression, albeit at the cost of making the stator sleeve thicker compared to a metallic sleeve.

On the other hand, if the rotor sleeve is made of an electrically conductive material, this may give rise to losses in the rotor sleeve due to the space and time harmonics of the stator magnetomotive force, and the harmonics arising from the slotted geometry of the stator[2]. Space harmonics arise from non-sinusoidal winding distribution in the stator. The magnitude of space harmonics is a function of the winding layout (number of slots/pole/phase). In contrast, the time harmonics originate from the pulse-width modulated inverter used to control the torque (or speed) of the generator.

Unlike stator sleeve, the choice of the rotor sleeve material is more flexible due to potentially lower losses on the rotor side. In other words, the increased thickness of the stator sleeve on account of using a glass fibre sleeve is more justified than the corresponding increase in the rotor sleeve thickness. In yet other words, using a metallic sleeve on the rotor side might actually prove to be a cost-effective solution. A detailed discussion on the choice of sleeve materials is postponed to the next chapter.

From the above discussion, it follows that both electrically conductive as well as non-conductive materials may be used in the protective sleeves. However, using a conductive material on the stator side causes excessive eddy current losses [8]. Therefore, in this thesis we analyze an intermediary design which uses the glass fibre coating on the stator side, while keeping the choice of rotor sleeve material flexible. This choice eliminates eddy current losses in the stator sleeve.

The magnitude of the rotor eddy current losses depends on the winding layout in the stator, wetgap dimensions, thickness of stator and rotor sleeves, conductivity of the material and current loading in the stator. A PM machine with integer-slot distributed winding usually results in very low rotor losses for the low-speed direct drive generators, even with a conductive rotor sleeve [9]. However, same cannot be said unequivocally for machines with fractional-slot windings. Therefore, it becomes imperative to have a good estimate of the rotor eddy current losses. This is done so as to lay a foundation for the discussion on selection of sleeve materials in the next chapter.

The bulk of this chapter is dedicated to estimating the eddy current losses in the rotor sleeve of the flooded generator. In the next section, parameters of a baseline flooded tidal turbine generator are presented for the analysis in this and the next chapter. Section 6.3 briefly presents the methodology adopted to calculate the copper and iron losses in the PM generator. Sections 6.4 to 6.8 cover the methodology to calculate the rotor eddy current losses from the space and time harmonics of the stator MMF. A brief description of the flooded generator prototype built under the TiPA project (of which this thesis is a part) is given in Section 6.9. Finally, conclusions from this chapter are given in Section 6.10.

6.2 System description: Baseline generator

For the purpose of analysis, we shall consider a 300 kW tidal turbine power take-off system with a PM generator. Further, we assume that the turbine is operated at a constant speed of 30 rpm. The

[2] In low speed direct-drive generators with relatively large magnetic airgaps, this loss is usually negligible.

generator design parameters are listed in Table 6.1.

PM machines with integer-slot windings have negligible losses in the rotor due to the space harmonics. Hence, the choice of the material for the rotor sleeve is not as critical in these machines [9]. However, same cannot be asserted about the PM machines with fractional-slot concentrated windings as they contain significant spatial harmonics in their stator magnetomotive force. The spatial harmonic spectrum corresponding to this slot-pole combination is depicted in Figure 6.3.

The reason for considering fractional-slot windings is that they offer certain advantages over integer-slot windings (e.g. shorter end-windings, high efficiency, low cost and ease of manufacturing) compared to the integer-slot windings [10]. Accordingly, a fractional-slot PM machine with a base winding of 12/10 (slots/poles) is analyzed in this thesis. This slot-pole combination is frequently used in the design of PM machines.

Table 6.1 Flooded Generator Parameters

Symbol	Parameter	Value
P	Rated Power	300 kW
B_r	Remanent flux density in PM	1.25 T
ω_m	Rated Speed	30 rpm
σ_{PM}	Magnet conductivity	5.56×10^5 S/m
R_s	Watergap radius	1.2 m
c_{tr}	Rotor sleeve thickness	2 mm
c_{ts}	Stator sleeve thickness	3 mm
g	Watergap radial length	8 mm
α_m	Magnet-arc to pole-pitch ratio	0.7
h_m	Magnet height	24 mm
p	No. of pole pairs	55
Q_s	No. of stator slots	132
h_s	Stator slot depth	80 mm
b_s	Stator slot width	39 mm
L	Stack length	0.7 m
h_{yoke}	Stator and rotor yoke heights	20 mm
k_{sff}	Slot fill factor	0.5
$J_{s,max}$	Max current density in the stator slot	2.7×10^6 A/mm^2
p_{Fe0h}	Specific hysteresis loss at 1.5 T and 50 Hz	2.0 W/kg
p_{Fe0e}	Specific eddy current loss at 1.5 T and 50 Hz	0.5 W/kg

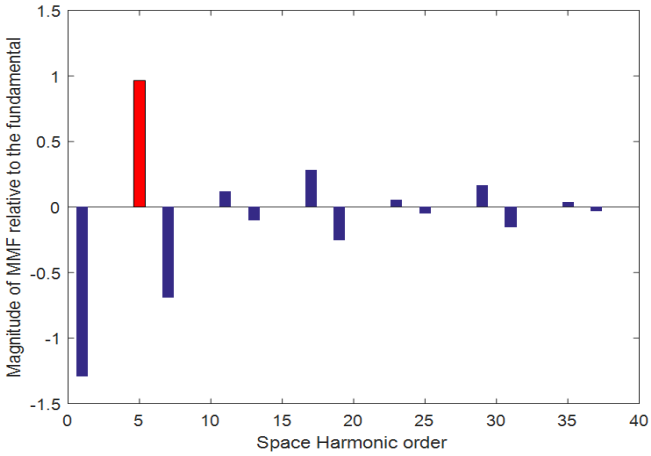

Figure 6.3 Three-phase MMF spectrum for fractional-slot concentrated winding (12/10 single layer). Red bar represents the fundamental spatial harmonic with winding factor of 0.95.

6.3 Electromagnetic model

The main quantities of interest derived from an electromagnetic model are induced emf, inductances and electromagnetic losses (iron and copper) in the generator. These can either be determined by analytical equations [11, 12] or using finite element methods [13, 14], or a combination of both [15, 16]. In any case, the goal is to determine magnetic flux densities in the airgap (or watergap), stator and the rotor iron. Since derivation of these quantities is comprehensively addressed in the literature, we do not repeat them here. However, a brief description of losses is given below as they are instrumental in the selection of the sleeve materials, as shall become evident in the next chapter.

6.3.1 Losses in the stator

Total loss in the stator comprises of iron loss (hysteresis and eddy current) and copper loss. Copper loss density in the stator slots is calculated as,

$$p_{Cu} = \int \frac{J_s^2}{\sigma} dV, \tag{6.1}$$

where J_s is the current density in the stator slots; the integral is evaluated over the volume of stator slots. Corresponding to 300 kW power at 30 rpm, the maximum current density required in the stator slots of the baseline generator is approximately 2.7×10^6 A/mm^2.

In contrast, the iron loss density in the stator is calculated using the Steinmetz equation [17]:

$$p_{Fe} = 2p_{Fe0h}\left(\frac{f_e}{f_0}\right)\left(\frac{\hat{B}_{fe}}{\hat{B}_0}\right)^2 + 2p_{Fe0e}\left(\frac{f_e}{f_0}\right)^2\left(\frac{\hat{B}_{fe}}{\hat{B}_0}\right)^2, \tag{6.2}$$

where, f_e is the frequency of the field in the iron, $\hat{B}_{Fe}$ is the magnetic flux density in the iron; p_{Fe0h} and p_{Fe0e} are the specific hysteresis and the eddy current losses (W/kg) at magnetic flux density, $\hat{B}_0$ of 1.5 T and frequency, f_0 of 50 Hz. This loss density is calculated separately for the stator teeth and the yoke. The total iron loss is then calculated by multiplying the volume of the stator teeth and the stator yoke with their corresponding iron loss densities.

6.3.2 Losses in the rotor

Losses in the rotor can occur in the magnets, rotor sleeve and the rotor iron. In case the latter is laminated, we can assume negligible losses in the rotor iron.

As already mentioned, fractional-slot machines contain a higher magnitude of the space harmonics in their stator magnetomotive force (MMF). The space harmonic component arises from the non-sinusoidal distribution of the stator windings. The stator MMF also has a time harmonic component arising from currents of multiple frequencies in the stator, which is generally the case when machines are driven by a power electronic converter.

Both space and time harmonic MMFs may cause significant eddy current losses in the rotor magnets. In case of a flooded generator, losses in rotor sleeve would be more significant than the losses in the magnets, provided rotor sleeve is made of metallic material. A good estimation of the rotor losses is thus necessary for a good design of a PM machine with fractional-slot windings.

Various analytical, finite element (FE), and a combination of analytical and FE models have been proposed for the eddy current loss modeling in PM machines. A detailed survey of these loss calculation methods is given in [18].

Analytical models are fast and provide a good insight into the loss characteristics and trends. However, analytical models are difficult to formulate and have limited accuracy. The latter usually arises due to the non-linear behavior of the materials, complex geometry of the machine (e.g. stator slotting, circumferential segmentation of the magnets), and various other assumptions that are made to simplify the model [18–21].

On the other hand, FE models are easy to setup, can deal with complex geometries, segmentation of the magnets, and non-linear permeability of the iron, etc. [22–24]. The main drawback of the FE models is that they are time-consuming [18]. Computing memory is no longer an issue, unless large scale 3D modeling is necessary [25]. A time-stepped FE simulation, solved over both the stator and the rotor domains, is considered to be the most accurate method to calculate the rotor losses. Such models are time-consuming, which makes them undesirable in situations where speed is preferred over high accuracy; for instance, in a machine design optimization problem.

A good approach to speed up the loss calculation is to model only the rotor domains and the airgap, and impose a linear current density or a magnetic field boundary condition on the stator

inner radius, as shown in Figure 6.4. This template has been adopted widely both in analytical as well as FE methods [19, 20, 26, 27]; consequently, these models are referred to as 'rotor-only' models.

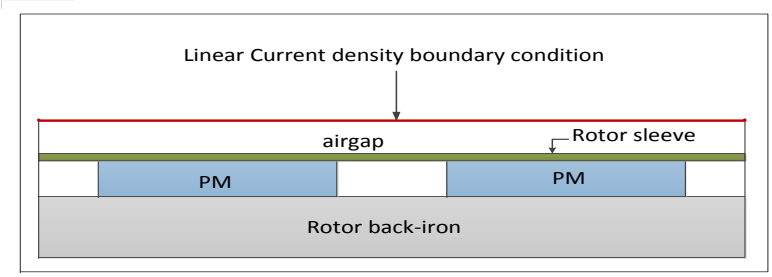

Figure 6.4 Imposing a linear current density boundary condition on the stator inner radius.

Following assumptions are commonly employed in the rotor-only models.

- Stator and rotor irons are assumed to have a linear BH-curve.
- Rotor iron is laminated, and has negligible losses. Nonetheless, the models presented in this paper can also predict losses in the solid rotor iron, provided accurate values of the permeability in the iron are known.
- Eddy current loss in the rotor owing to the airgap permeance variations because of the stator slotting is neglected. Normally, this gives rise to losses in the rotor even under no-load conditions. However, these losses are usually significant only in high-speed machines or machines with small airgap.
- End effects in the permanent magnets and the rotor sleeve are neglected. Induced currents only have an axial component.
- Eddy current field in the rotor does not influence the stator field at the stator inner radius.

The main advantage of the rotor-only models is their faster speed because of the reduced mathematical complexity, which is further augmented by smaller problem size. However, these models require some prior analytical or FE calculations to appropriately define the boundary conditions. As mentioned earlier, the boundary condition at the stator inner radius can be of different types (e.g. current density or magnetic field intensity). Magnetic field boundary conditions may yield more accurate results under certain conditions, such as when including saturation or stator slotting effects [22, 28].

Analytical calculation of magnetic field or potential boundary conditions is rather difficult, and may require some sort of magnetostatic FE calculations [22]. For linear iron, a current density boundary condition is sufficiently accurate, and easy to calculate analytically. For these reasons, we employ a current density boundary condition in this thesis.

In the following sections, we shall compare three different approaches to solve a rotor-only model, using time domain and frequency domain analyses. The results from these three models are compared to the benchmark model. The benchmark model comprises a full 2D cross-section (including the stator) of the PM machine solved using a time-stepped finite element model. The main drawback of the benchmark model is its time cost.

We shall demonstrate that frequency domain models can yield nearly the same results as the time domain models within a fraction of a time taken by the latter. Two different frequency domain methods are presented. First, a commonly applied frequency domain analysis in the rotor frame with rotor frequency is explained. This is followed by a more novel frequency domain analysis in the rotor frame with stator frequency, using the Lorentz force term. The latter of the frequency domain methods, proposed in this chapter, is shown as the fastest method to compute the rotor losses.

Sections 6.4 to 6.5 detail the mathematical formulations regarding the time domain and frequency domain models for eddy current loss calculations in the rotor, respectively. These sections only address the rotor losses due to the space harmonics in the stator MMF, assuming the current in the stator windings is known a priori. Section 6.6 compares the results from all the time domain and frequency domain methods presented here. In the later part of this chapter (section 6.7 onwards), the rotor loss model is extended to include the time harmonic losses as well. These time harmonics originate from the pulse-width modulated (PWM) inverter controlling the tidal turbine generator.

6.4 Time domain models

This section presents two time domain models. The first, full 2D cross-section transient model, is designated as the benchmark model. And the second model is a rotor-only model. The mathematical formulations for each of these models is presented below.

6.4.1 Full transient model: Benchmark model (TD-FU)

A more accurate calculation of the eddy current losses usually involves a time-stepped finite-element analysis involving mesh coupling in the airgap to model the rotor motion [28, 29]; see Figure 6.5. Following equations are used in this model:

$$\begin{aligned} \nabla \times \left(\frac{1}{\mu}\nabla \times A_z\right) + \sigma \frac{\partial A_z}{\partial t} &= J_{ext,z,u}, \\ \nabla \cdot \left(-\sigma \frac{\partial A_z}{\partial t} + J_{ext,z,u}\right) &= 0, \end{aligned} \tag{6.3}$$

$$\oint \lambda (A_{st} - A_{rt}) \cdot dl = 0. \tag{6.4}$$

Here, μ is the magnetic permeability, A_z is the magnetic vector potential along z-axis, σ is the electrical conductivity, and $J_{ext,z,u}$ is the u^{th} order time harmonic component of the externally

imposed current density along z-axis[3]. A_{st} and A_{rt} represent the vector potential on the stator and rotor side of the airgap interface respectively, and λ is the Lagrange multiplier.

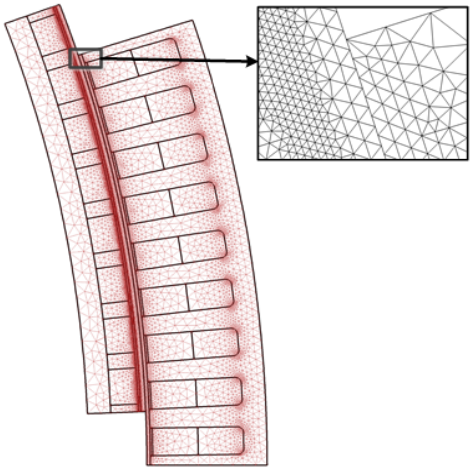

Figure 6.5 Full transient model with mesh coupling in the airgap: if moving mesh does not match exactly at the airgap, interpolation is required.

Equation 6.3 is the quasi-static Ampere-Maxwell equation, coupled with the current conservation over each domain which is electrically insulated from other domains. In other words, it is used to ensure that the total current in each magnet segment adds up to zero at all time instants. Equation 6.4 is used for mesh coupling in the airgap, and ensures that the magnetic vector potential is continuous across the stator-rotor interface in the airgap. A simple periodic boundary condition at the edges of the 2D sector, and magnetic insulation boundary conditions at the rotor inner and stator outer radius suffice for this model.

Once A_z is determined, the rotor loss is calculated as follows,

$$P_{eddy} = \int \frac{J_z^2}{\sigma} dV, \tag{6.5}$$

where σ is the electrical conductivity of the material. The integral is evaluated over the volume of the material where the loss occurs. The induced current density itself is calculated from the

[3] z-axis is normal to the plane of modeling. The current density, $J_{ext,z,u}$ is calculated from the knowledge of stator phase current (I_{ph}), number of conductors per slot (n_{cs}), slot filling factor (k_{sff}) and the area of the slot (A_{slot}) . For a single-layer winding,
$J = \frac{n_{cs} I_{ph}}{A_{slot} k_{sff}}$

induced electric field E_z such that,

$$\begin{aligned} J_z &= \sigma E_z + J_{ez} \\ E_z &= -\frac{\partial A_z}{\partial t}, \end{aligned} \tag{6.6}$$

where J_{ez} is the circulating current because of the additional current constraint in (6.3).

This model yields time-variant rotor losses, which converge about the steady state value after some time. A case example is shown in Figure 6.6. Thus, some sort of judgement is necessary to determine if the model has converged satisfactorily after certain time. This time is sensitive to the machine design parameters, operating point, and material properties; hence, undesirable from the viewpoint of automated calculations [30]. However, the time to convergence could be reduced by a good initial solution. Full transient model includes the modeling of the stator domains as well. Consequently, if finer mesh is to be used, the problem size increases much more compared to the rotor-only models.

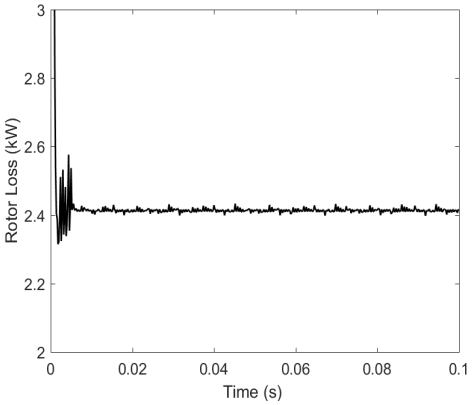

Figure 6.6 Typical convergence of a full transient model.

The advantages of this model include implicit inclusion of the stator slotting, saturation of iron, and the simplicity of its boundary conditions. In addition to this, the beauty of this method lies in its ability to simultaneously include all the space as well as time harmonics. For these reasons, despite its aforementioned drawbacks, full 2D transient model is used as a benchmark for the rest of the models described in this chapter.

6.4.2 Time-stepped rotor-only model (TD-RO)

The model is based on (6.3) as the previous model. Since it is a rotor-only model, there is no need for any mesh-coupling in the airgap. This model uses the linear current density boundary

condition at the stator inner radius, as shown in Fig. 1. The current density is given by [19] :

$$K_{s,u} = \frac{3N_{ph}}{\pi R_s} \sum_u I_u \sum_v K_{sov} K_{wv} sin(up\omega_r t \pm v\theta_s + \theta_u), \tag{6.7}$$

where, R_s is the stator inner radius. The equations for calculating the slot opening and winding factors can be found in [31]. When slot opening width is negligible compared to the airgap diameter, then K_{sov} approaches 1. The corresponding boundary condition is then given by [32]:

$$n \times H = K_{s,u}, \tag{6.8}$$

where, n is the normal at the boundary, and H is the magnetic field intensity just inside the airgap. Besides this boundary condition, the rest of the boundary conditions remain the same as in the TD-FU model. Because the rotor is kept stationary, the boundary condition needs to be transformed from the stator frame to the rotor frame using the following transformation in (6.7):

$$\theta_s = \theta_r + \omega_r t, \tag{6.9}$$

The model just like the previous time domain model can include all the time harmonics as well as space harmonics simultaneously. Normally, only a few dominant space harmonics need to be included. A quick analytical calculation of the relative magnitudes of the MMF due to different space harmonics can be calculated. From this, it is possible to predict which harmonics should be included for a good enough rotor loss estimation.

This model is much faster than the TD-FU model, and the time-variant rotor losses also converge faster to the steady state value. Speed enhancement is thus twofold: due to the smaller problem size and shorter time to convergence. Just like the previous model, the total time cost and the solver time step-size depends on the material properties and speed of the rotor. Higher frequencies demand smaller time steps, whereas low frequencies need to be modeled for longer time to transcend the transient period.

6.5 Frequency domain models

6.5.1 Frequency domain—rotor-only in rotor frequency (FD-RORF)

Eddy current loss calculation using the frequency domain analysis is much faster than using the time domain models. For a single frequency and a linear system, both analyses should in principle give identical results. Contrary to the time domain analysis which has to wait for transients to die down, frequency domain analysis straightaway provides with the steady state results. These models are preferable when dealing with a single frequency component. For systems where the superposition principle holds, the total eddy current loss is obtained by summing up the contributions from each frequency component. Since the assumption of linear BH-curve has been made for the iron, the superposition principle is applicable.

Utilizing the speed advantage of the frequency domain analysis, the time domain rotor-only models can be easily transferred to the frequency domain to speed up the rotor loss calculation.

In this section, two frequency domain models—in the rotor-frequency frame and in the stator-frequency frame—are explained.

In literature, frequency domain models are also referred to as the 'time-harmonic' model. Space harmonics corresponding to the same time harmonic of the stator current induce eddy currents of different frequencies in the rotor. As a result, an independent frequency domain analysis is required for each frequency component. The time cost for each frequency domain analysis is almost independent of the frequency. Thus, the total time cost is the time cost of a single frequency domain analysis times the number of frequency components.

However, it is possible to solve for each frequency component in parallel, which can significantly reduce the total time-cost, albeit at the expense of more computing resources or complexity. The governing equations remain the same as in TD-RO model, which are expressed in the frequency domain as:

$$\begin{aligned} \nabla \times \left(\frac{1}{\mu}\nabla \times A_z\right) + j\sigma\omega_u A_z = J_{ext,z,u}, \\ \nabla \cdot \left(-j\sigma\omega_u A_z + J_{ext,z,u}\right) = 0, \end{aligned} \tag{6.10}$$

The boundary conditions also remain exactly the same as in TD-RO model. The frequency associated with the space harmonic of order 'n' in the rotor frame is given by the following equation:

$$\omega_\nu = \omega_{e,u}\left(1 - sgn(\nu)\frac{\nu}{p}\right), \tag{6.11}$$

where, $\omega_{e,u}$ is the fundamental electrical frequency associated with the time-harmonic in the stator; '$sgn(\nu)$' should be taken as either '+1' or '-1', depending upon whether the MMF wave corresponding to 'nth' harmonic is moving in the same or opposite direction compared to the main field, respectively. The total eddy current loss is then given by:

$$P_{ed,total} = \sum_\nu P_{ed,\nu}, \tag{6.12}$$

where, $P_{ed,\nu}$ is the loss corresponding to the each space harmonic.

6.5.2 Frequency domain—rotor-only in stator frequency (FD-ROSF): Proposed method

In the stator frame, space harmonics of the MMF have the same electrical frequency, therefore, if the loss calculation is performed in the stator frame then a single frequency domain analysis should suffice. The following method is based on this principle. To model the rotor motion, the rotating domains equations are modified with the Lorentz force term ($v \times B$), as shown below:

$$\begin{aligned} \nabla \times \left(\frac{1}{\mu}\nabla \times A_z\right) + j\sigma\omega_u A_z - \sigma v \times (\nabla \times A_z) = J_{ext,z,u}, \\ \nabla \cdot \left(-j\sigma\omega_u A_z + \sigma v \times (\nabla \times A_z) + J_{ext,z,u}\right) = 0, \end{aligned} \tag{6.13}$$

where, $v = r \times \omega$ is the linear velocity at any point in the rotor domain, and $B = \nabla \times A_z$. Clearly, the velocity term is zero for any stationary domain. Even in the presence of multiple dominant rotor frequencies, only one frequency domain analysis is necessary to calculate the eddy current losses in the rotor. If other time harmonics are included, then the total time cost gets multiplied by the number of dominant stator time harmonics, irrespective of the number of dominant rotor frequencies. Again parallel computing will bring down the total time cost. Furthermore, this method neither requires any transformation of the current density boundary condition from the stator to the rotor frame, nor does it require calculation of the rotor frequencies.

6.6 Comparing results from different rotor loss models

The eddy current losses in the flooded generator rotor calculated from the time domain and the frequency domain models are compared in this section. The full transient model with moving rotor (TD-FU) forms the benchmark on which the results from other models, namely, time domain rotor-only (TD-RO), frequency domain rotor-only in rotor frequency (FD-RORF) and frequency domain rotor-only in stator frequency (FD-ROSF), shall be judged. To verify the accuracy of the rotor-only models, results are compared over a range of rotor sleeve conductivity values and rotor speeds[4].

Eddy current losses for the PM generator as a function of speed is shown in Figure 6.7. It is evident that rotor-only models give reasonably accurate results over a wide range of speeds. At higher speeds, the current loading is assumed to be the same as at the lower speeds, and thus, the actual power rating is assumed to vary linearly with the speed. It is observed that the eddy current losses predicted from the TD-FU models is lower than what is predicted from the rotor-only models. A possible reason is that in the TD-FU model, some of the MMF does not cross into the rotor because of the slot leakage. Some inaccuracies also occur because of the tolerances set in the time domain models, especially in the current conservation equation, in order to hasten the convergence towards the steady state solution.

In Figure 6.8, the accuracy of the rotor-only models is shown with different values of the rotor sleeve conductivity. Slight disagreement between the models is seen as the conductivity increases. This is because the Lorentz force term is multiplied by the conductivity, and any slight error in the estimation of the magnetic field is reflected in the results. Same happens when higher speeds are involved. PM losses are seen to decrease at higher rotor sleeve conductivity values because of the shielding effect of the sleeve, as shown in Table 6.2. The effect is seen in all four models, although for illustration, only the results from TD-RO model are shown. Although it is unlikely that a rotor sleeve with electrical conductivity of the order of 10^9 (S/m) will be used, Figure 6.8 shows that models work nicely even at extremely high conductivity values.

[4]This chapter only compares the results for 12/10 (slot/pole) single-layer winding. However, the methods were also compared for 9/8 (slot/pole) double-layer winding in another published article by the author, mentioned on the front page of this chapter. The reason for comparing the methods for 9/8 configuration too is because more than one space harmonic contributes significantly to the rotor eddy current losses. In contrast, in a 12/10 winding loss from only one space harmonic is dominant.

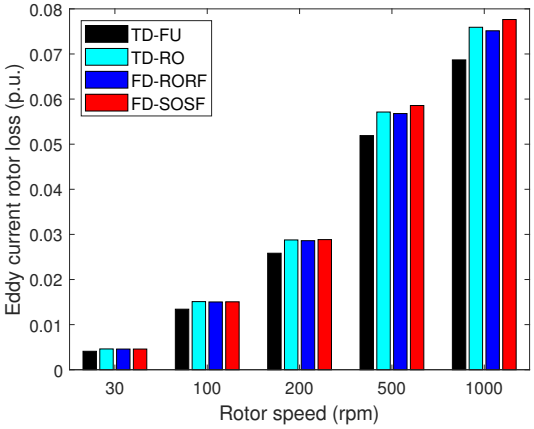

Figure 6.7 Eddy current loss in the rotor (sleeve and PM) as a function of the rotor speed.

Table 6.2 Rotor eddy current loss as a function of rotor sleeve conductivity (from TD-RO model)

Rotor sleeve conductivity (S/m)	Sleeve loss (p.u.)	PM loss (p.u.)	Total loss (p.u.)
1.4×10^{6}	0.33×10^{-2}	0.124×10^{-2}	0.45×10^{-2}
1.4×10^{7}	3.07×10^{-2}	0.118×10^{-2}	3.19×10^{-2}
1.4×10^{9}	1.43×10^{-2}	4×10^{-6}	1.43×10^{-2}

It is well known that frequency domain models take far less time than equivalent time domain models to be solved. Also, for time domain models, the time cost depends on the time for which simulation is carried out, that is, until transient effects almost die out. Therefore, some sort of definition needs to be adopted to determine the time cost of the time domain models. Here, we define the time cost of the time domain models as the time it takes to model 5 electrical cycles of the lowest frequency induced in the rotor. Clearly, this is an arbitrary definition, but it is hardly relevant to the time cost trend observed. Table 6.3 shows the time cost of the four methods analyzed here. The simulations were performed on Intel Xeon 3.5 GHz processor with 32 GB RAM, using the COMSOL Multiphysics software. The trend for the time cost is as follows:
TD-FU (minutes) > TD-RO (seconds/minutes) > FD-RORF (seconds) > FD-ROSF(seconds).

To summarize, the proposed method in frequency domain with the stator frequency (FD-ROSF) was shown to be the fastest method to calculate rotor eddy current losses. Despite being a rotor-only model, and involving no rotor motion using the moving mesh, this model required no transformation of the current density boundary condition to the rotor frame, and no prior calculation of the induced rotor frequencies. Furthermore, this model calculated losses from all space harmonics simultaneously using a single frequency domain analysis. Rotor losses due to the time harmonics (e.g. in a pwm-controlled generator) can be easily obtained by employing the same models, albeit with different frequencies. For these reasons, FD-ROSF was chosen as the

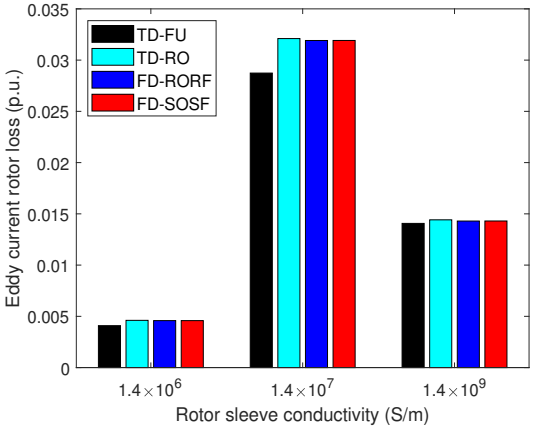

Figure 6.8 Eddy current losses in the rotor (sleeve and PM) as a function of the rotor sleeve conductivity (TD-RO model). Maximum rotor eddy current losses occur around a conductivity of 1×10^8 (S/m), after which the rotor losses start decreasing because of the shielding effect. This clearly illustrates that using a material of very high conductivity will actually decrease losses rather than increase them.

Table 6.3 Time Cost for Eddy Current Loss Calculation Methods

Model type	Time Cost
Time domain full transient (TD-FU)	8m 10s
Time domain rotor-only (TD-RO)	1m 50s
Frequency domain rotor-only in rotor frequency (FD-RORF)	12s
Frequency domain rotor-only in stator frequency (FD-ROSF)	4s

method of choice for calculating the rotor eddy current losses in this thesis.

6.7 PWM-induced rotor losses

This section presents the methodology to compute the losses in the rotor due to the time harmonics in stator currents. Because of the switching nature of the converter, the voltages and currents in the generator are not purely sinusoidal, and contain several higher order time harmonics. The stator MMF wave setup by these higher order harmonics are asynchronous with the rotor speed, resulting in eddy current losses in the rotor.

The following approach is adopted in order to calculate the rotor eddy current losses from time harmonics. First, the speed and torque inputs to the generator electromagnetic model are estimated from the turbine model. Afterwards, the stator phase currents are calculated from the generator model. Subsequently, a time-domain fast fourier transform is used to calculate higher order frequency components in the current. The rotor eddy current losses from each time harmonic component is calculated using the FD-ROSF method explained above. A flow chart of the process is shown in Figure 6.9.

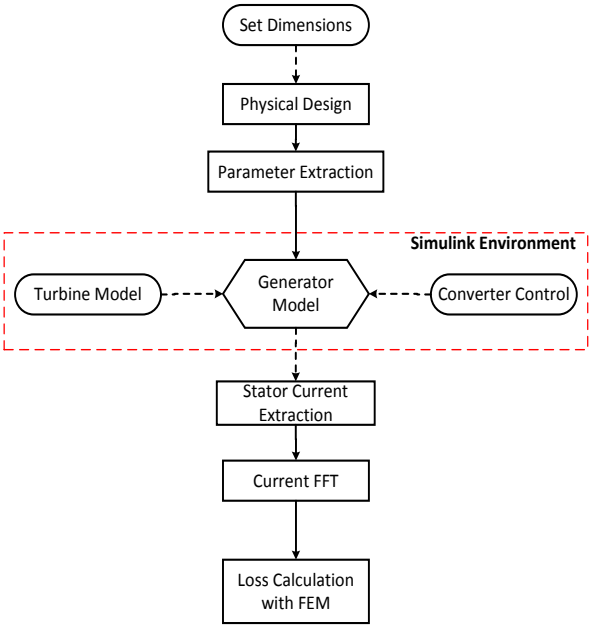

Figure 6.9 Flowchart to illustrate the calculation of PWM-induced eddy current losses in the rotor-can of the flooded PM generator.

The turbine, PM generator and a two-level voltage source converter are modeled using in-built modeling blocks in MATLAB Simulink environment. The turbine is modeled using the following

Table 6.4 Generator Electromechanical Parameters

Symbol	Parameter	Value
P	Rated Power	300 kW
R	Resistance per phase	0.01 p.u. (1.3 mΩ)
L_d or L_q	Inductance (d and q) axes	0.72 p.u. (0.50 mH)
V_{dc}	DC-link voltage	660 V
λ_s	Flux-linkage per phase	0.89 V.s
J	Moment of Inertia	17580 kg.m^2

equations:

$$P = \frac{1}{2} C_p \rho U^3 A, \tag{6.14}$$

$$J_m \frac{d\omega_m}{dt} = T_m - T_e, \tag{6.15}$$

where, P is the power generated by the blades, C_p is the power coefficient of the turbine, ρ is the mass density of water, U is the tidal velocity, A is the swept area of the turbine, J_m is the moment of inertia, ω_m is the rotational velocity, and T_m and T_e are the mechanical and electrical torques, respectively.

Assuming that the rotor eddy current field has negligible effect at the stator bore, the stator current is calculated from the following differential equations (in dq-frame):

$$\frac{di_d}{dt} = \frac{1}{L_d} v_d - \frac{R}{L_d} i_d, \tag{6.16}$$

$$\frac{di_q}{dt} = \frac{1}{L_q} v_q - \frac{R}{L_q} i_q - \frac{L_d}{L_q} p\omega_m i_d - \frac{\lambda_m}{L_q} p\omega_m, \tag{6.17}$$

$$T_e = 1.5p[\lambda_m i_q - (L_d - L_q) i_d i_q] \tag{6.18}$$

where, i_d, v_d, L_d are the direct axis components of the stator quantities. Similarly i_q, v_q, L_q are the quadrature axis quantities. Also, p is the number of pole-pairs of the generator and λ_m is the flux linkage contributed from magnets. The electrical parameters for the machine are listed in Table 6.4. The parameters correspond to the PM generator dimensions given in Table 6.1.

The assumption that eddy current field of the rotor sleeves has negligible effect on the stator current could only be valid if the eddy current in rotor sleeve is resistance limited rather than inductance limited. In other words, we assume that the machine inductance is independent of the frequency [13].

The gate signal inputs to the inverter switches are obtained from the sine wave pulse width modulation technique for a speed reference of 30 rpm, which is the rated speed of the generator. A simple PI-controller for the speed (outer loop) and current controller (inner loop in dq-frame) is used to control the machine.

An active speed stall-controlled turbine implies that the converter and the generator need to be overrated to account for sudden surges in speed [33]; details given in Chapter 4. Here we estimated an overrating of 40% in the kVA rating of the converter (over the rated power of the generator). This overrating is calculated from assuming a surge of 0.7 m/s in speed at cut-out speed of 3.3 m/s. The outer speed control gains (PI-controller) and the inner current control gains (again PI) are tuned to achieve fast response and not to let the turbine over-speed for a temporary surge in tidal velocity [33]. Since the electrical time constant of the converter-generator is smaller than its mechanical time constant, the variations in current due to speed fluctuations about the reference speed are not considered to have significant impact on the pulse-width modulated eddy current losses in the generator. For this reason, speed fluctuation in the generator due to turbulence, etc. is not considered here.

6.8 Results and discussions

The analysis is carried out for a mean tidal velocity of 3 m/s, at which the generator rotates at a speed of 30 rpm and delivers around 300 kW of power. The rotor eddy current losses are calculated at two different switching frequencies: 2 kHz and 4 kHz. For this chapter, we assume that the rotor sleeve is made of non-magnetic stainless steel 304L.

The induced eddy current loss density in the rotor sleeve and two magnets is shown in Figure 6.10. The losses are higher in the rotor sleeve because of its higher conductivity and non-segmented geometry.

The total eddy current loss (from all space and dominant time harmonics) in the rotor sleeve is 10.994 kW, whereas the loss in the magnets is 765.92 W, at a switching frequency of 2 kHz. The corresponding losses at 4 kHz are 10.965 kW and 759.75 W respectively. A small decrease in the loss on increasing the switching frequency is noticed. This is a consequence of higher harmonic distortion at 2 kHz compared to 4 kHz. Time harmonic components of the stator current at 2 kHz and 4 kHz switching frequency are shown in Figures 6.11 and 6.12. The corresponding rotor eddy current losses due to each time harmonic component are presented in Figures 6.13 and 6.14.

It is clear that time harmonic components near the switching frequency have negligible magnitude, and hence make no perceptible contributions to the total rotor loss. In other words, rotor eddy current losses are mainly due to the space harmonics of the fundamental current component. The substantial space harmonic components are a consequence of the fractional-slot concentrated winding layout.

It can thus be concluded that for design purposes the converter induced losses in the rotor could be neglected, and focus should be more on the space harmonic induced losses. Because the

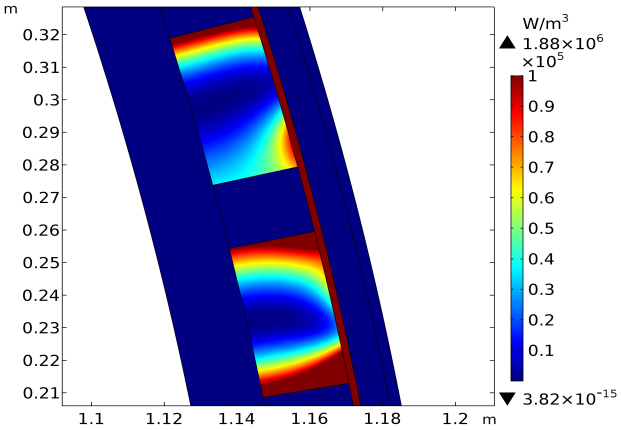

Figure 6.10 Eddy loss density distribution in the rotor can and a single permanent magnet (Rotor sleeve material: Stainless Steel 304L). Finite element simulation software: COMSOL Multiphysics.

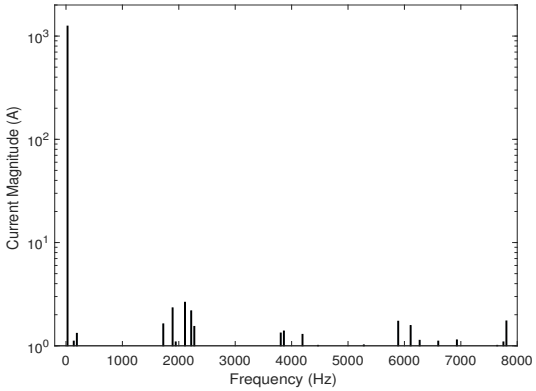

Figure 6.11 Time harmonic components of stator current at switching frequency of 2 kHz.

time harmonic losses near switching frequency and skin effects are negligible, their eddy current reaction field effect is negligible. This assumption was made in the beginning and is validated by the loss results.

In the next chapter, thermal model for the flooded generator is described. The electromagnetic and thermal models together give a strong indication about the type of materials to be used in the sleeves for the flooded generator. However, before that a brief description of the prototype flooded generator is given in the next section.

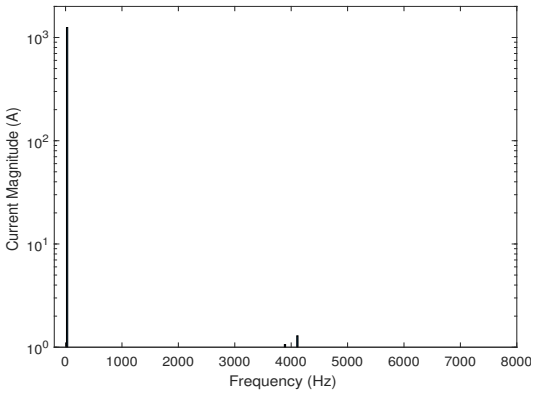

Figure 6.12 Time harmonic components of stator current at switching frequency of 4 kHz.

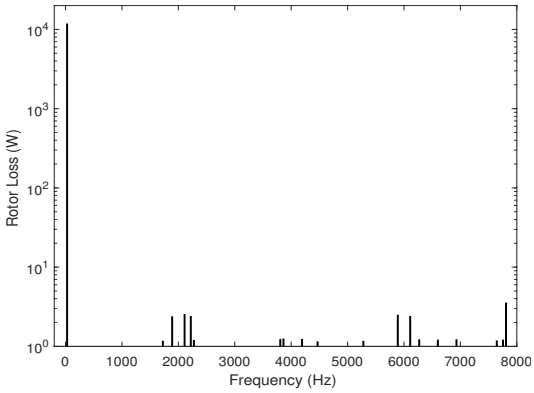

Figure 6.13 Rotor eddy current loss in the stainless steel rotor sleeve and magnets as a function of time harmonic components of stator current at switching frequency of 2 kHz.

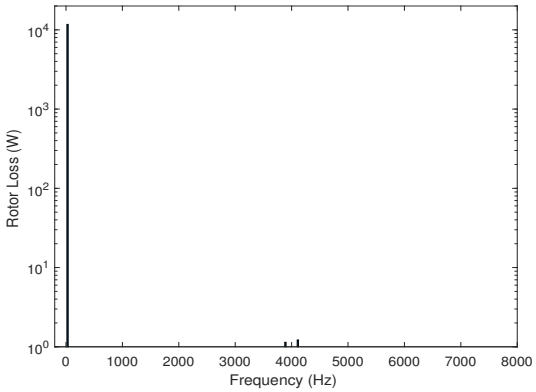

Figure 6.14 Rotor eddy current loss in the stainless steel rotor sleeve and magnets as a function of time harmonic components of stator current at switching frequency of 4 kHz.

6.9 Prototype generator : TiPA project

As mentioned in Chapter 1, this thesis is a part of a larger consortium called the TiPA project. As a part of the project, a flooded generator prototype was developed for Nova Innovation's 100 kW turbine.

The flooded generator was assembled at NOVA Innovation Limited facility in Edinburgh, Scotland. As a proof of concept, the TiPA power take-off (PTO) system underwent a rigorous testing regime developed by Nova Innovation and RWTH Aachen University (Germany) to test the performance and survivability of the novel system. Initially, the PTO system was tested at RWTH Aachen, followed by in-sea testing. A picture from the RWTH test facility is shown in Figure 6.15.

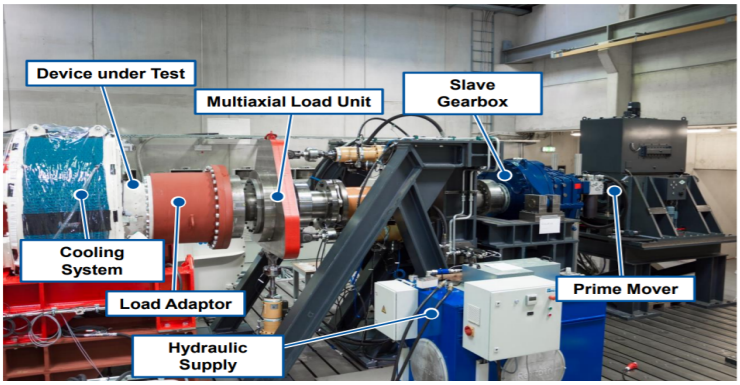

(a)

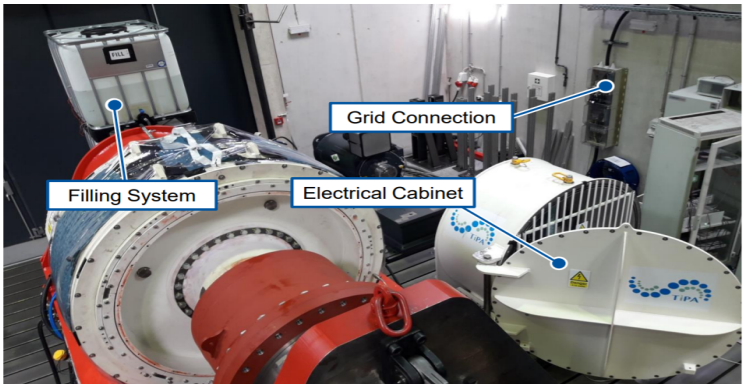

(b)

Figure 6.15 PTO testing at RWTH Aachen test facility, Germany; (a) side-view, and (b) top view.

In the lab facility, sea water cooling on the generator external surface was emulated by means

of a cooling blanket attached on the external frame of the generator. Inside the generator, a pump-operated filling system maintains the desired water pressure. Besides torque application, thrust and bending moments were also applied on the PTO by the hydraulic systems present on the test rig. The purpose of conducting these tests include checking the shaft deflections remain within limits, and non-torque loads have little to no impact on electrical conversion capability of the PTO.

In the subsequent phase, in-sea testing was conducted in the beginning of 2019 at Babcock's Rosyth site; see Figure 6.16. After running the PTO for more than two months, the PTO was retrieved from the sea. The PTO later underwent detailed forensic inspection at Nova Innovation's facility in Edinburgh. Key findings from the tests, on the test rig and in-sea operation, shall be used in subsequent designs to further optimize or improve the PTO design.

Figure 6.16 In-sea testing of TiPA PTO at Babcock's Rosyth site.

The contribution of this thesis towards the TiPA project is as follows. The conclusions drawn from the analysis of sleeve losses presented in the next chapter seemed to agree with the test results. As a result, the work conducted in this thesis shall inform the choice of sleeve materials, winding layout, etc. of the flooded generator in future. For confidentiality reasons, true dimensions and parameters of the prototype generator, as well as test results, could not be disclosed in this thesis.

Electromagnetically speaking, a key learning from the prototype testing was that a conductive stator sleeve leads to excessive eddy current losses in the generator, and hence must be avoided at all costs. Consequently, this means that materials such as glass or carbon fibers are more suitable as stator sleeves. Clearly, these materials have to be thicker than a corresponding metallic alloy sleeve, and hence affect the power density of the machine. Moreover, glass or carbon fibers on the stator sleeve should be rigorously tested in practical (in-sea) conditions to ascertain whether they can survive for the desired time period.

In a nutshell, the results obtained during the testing of the prototype PTO were along the same lines as expected from the modeling presented in this thesis—for the generator and the converter.

This thesis then proposed changing of sleeve materials and introduction of passive cooling system for the converter, which could be implemented in future designs for improved reliability.

6.10 Conclusion

Flooded generators have been proposed as a means of increasing the reliability of tidal turbine generators. Flooded generators mainly differ from conventional generators in having a protective stator and a rotor sleeve. These sleeves are meant to protect the stator and rotor parts of the generator from the sea water in the flooded gap. In order to ascertain the suitability of different materials for the stator and the rotor sleeves, their influence on the electromagnetic and thermal performance of the generator becomes imperative. From electromagnetic viewpoint, we are primarily interested in the losses in the sleeve, if the sleeve material is conductive. At the outset, we reasoned that a metallic stator sleeve would be a poor choice as it will compromise the generator efficiency significantly on account of the excessive eddy current losses. On the other hand, the choice of rotor sleeve remains flexible. However, the calculation of rotor eddy current losses requires more attention.

Compared to the losses in the stator, rotor eddy current losses are more challenging and time consuming to compute. For this reason, this chapter compared different methods for calculating the rotor eddy current losses in permanent magnet rotors—in sleeve and magnets. The methods were especially customized for optimization studies, and in general, do compromise some accuracy for speed. Of the four investigated methods, frequency domain analysis of a rotor-only model with stator frequency (FD-ROSF) was shown to be the fastest. This model—though not the most accurate—is good enough for making preliminary design choices.

Subsequently, on analyzing the rotor current losses in the machine, majority of the rotor eddy current losses were found to arise from the space harmonics—rather than time harmonics—of the stator MMF. This conclusion does not change with the converter switching frequency, and possibly the winding layout of the generator.

Bibliography

[1] L. Drouen, J. F. Charpentier, E. Semail, and S. Clement, “Study of an innovative electrical machine fitted to marine current turbines," in *OCEANS 2007-Europe*, IEEE, 2007.

[2] O. Krovel, R. Nilssen, S. Skaar, E. Lovli, and N. Sandoy, “Design of an Integrated 100kW Permanent Magnet Synchronous Machine in a Prototype Thruster for Ship Propulsion,” in Proceedings of ICEM, 2004, pp. 4–9.

[3] S. Djebarri, J. F. Charpentier, F. Scuiller, and M. Benbouzid, “Comparison of direct-drive PM generators for tidal turbines,” in *International Power Electronics Applications Conference and Exposition*, IEEE, 2014, pp. 474–479.

[4] Y. Burkhardt, G. Huth, and S. Urschel, “Eddy current losses in PM canned motors,” in *19th International Conference of Electrical Machines*, 2010, pp. 1-7.

[5] Q. Yu, X. Wang, and Y. Cheng, “Electromagnetic calculation and characteristic analysis of can effect of a canned permanent magnet motor,” *IEEE Transactions on Magnetics*, vol. 52, pp. 1-6, 2016.

[6] A. C. Smith, and E. Peralta-Sanchez, “Containment can losses in permanent-magnet pump drives”, *Journal of Applied Physics*, 99(8), 08R314, 2006.

[7] C. Scott. Considerations for a Canned Motor Pump. World Pumps. 2004 Dec 1;2004(459):22-5. [Online] https://www.sciencedirect.com/science/article/pii/S0262176204004195 [Accessed: 23 May 2019].

[8] A. Yadav, “Finding suitable material for the retaining sleeves in tidal generators,” Master Thesis, Delft University of Technology, Netherlands, 2017.

[9] F. Wani, U. Shipurkar, J. Dong, and H. Polinderr, “Calculation of PWM-induced rotor-can losses in flooded generators,” in *Proceedings of the 13th European Wave Energy and Tidal Conference (EWTEC 2019)*, Naples, Italy, 2019.

[10] A. M. EL-Refaie, “Fractional-slot concentrated-windings synchronous permanent magnet machines: Opportunities and challenges,” *IEEE Transactions on Industrial Electronics*, vol. 57, no. 1, pp. 107–121, 2010.

[11] A. Grauers, “Design of direct driven permanent magnet generators for wind turbines,” PhD Dissertation, Chalmers University of Technology, 1996.

[12] J. Pyrhonen, T. Jokinen and V. Hrabovcova, “*Design of rotating electrical machines, 2nd edition*,” John Wiley & Sons, 2013.

[13] M. van der Geest, “Design and modeling of high performance permanent magnet synchronous generator,” PhD Dissertation, Delft University of Technology, 2015.

[14] H. Jianhui, Z. Jibin and L. Weiyan, "Finite element calculation of the saturation DQ-axes inductance for a direct drive PM synchronous motor considering cross-magnetization", in *the Fifth International Conference on Power Electronics and Drive Systems*, IEEE, 2003, pp. 677-681.

[15] H. Vu Xuan, “Modeling of exterior rotor permanent magnet machines with concentrated windings,” PhD Dissertation, Delft University of Technology, 2012.

[16] A. EL-Refaie, Z. Q. Zhu, T. Jahns and D. Howe, "Winding inductances of fractional slot surface-mounted permanent magnet brushless machines", in *2008 IEEE Industry Applications Society Annual Meeting*, 2008, pp. 1-8.

[17] H. Li, Z. Chen and H. Polinder, “Optimization of multibrid permanent-magnet wind generator systems,” IEEE Transactions on Energy Conversion, vol. 24, no. 1, pp. 82-92, 2009.

[18] A. Jassal, H. Polinder, and J. A. Ferreira, "Literature survey of eddycurrent loss analysis in rotating electrical machines," *IET Electric Power Applications*, vol. 6, no. 9, p. 743, 2012.

[19] Z. Q. Zhu, K. Ng, N. Schofield and D. Howe, "Improved analytical modelling of rotor eddy current loss in brushless machines equipped with surface- mounted permanent magnets," *IEE Proceedings-Electric Power Applications*, vol. 151, no. 6, pp. 641–650, 2003.

[20] D. Ishak, Z. Q. Zhu, and D. Howe, "Eddy-current loss in the rotor magnets of permanent-magnet brushless machines having a fractional number of slots per pole," *IEEE Transactions on Magnetics*, vol. 41, no. 9, pp. 2462–2469, 2005.

[21] H. Polinder and M. J. Hoeijmakers, "Eddy-current losses in the segmented surface-mounted magnets of a PM machine," *IEE Proceedings- Electric Power Applications*, vol. 146, no. 3, p. 261, 1999.

[22] M. van der Geest, H. Polinder, and J. A. Ferreira, "Efficient finite element based rotor loss calculation for permanent magnetsynchronous machines," in *Proceedings of International Conference on Electric Machines (ICEM) 2014*, pp. 1133–1138, 2014.

[23] C. Mi, G. R. Slemon and R. Bonert, "Modelling of iron losses of permanent magnet synchronous motors," *IEEE Transactions on Industry applications*, vol. 39, no. 3, pp. 2585-2591, 2001.

[24] J. Wang, K. Atallah, R. Chin, W. M. Arshad, and H. Lendenmann, "Rotor eddy-current loss in permanent-magnet brushless AC machines," *IEEE Transactions on Magnetics*, vol. 46, no. 7, pp. 2701–2707, 2010.

[25] M. van der Geest, H. Polinder and J. A. Ferreira, "Computationally efficient 3D FEM rotor eddy-current loss calculation for permanent magnet synchronous machines," in *Proceedings of Electric Machines & Drives Conference (IEMDC) 2015*, pp. 1165–1169.

[26] M. R. Shah and S. Bin Lee, "Rapid analytical optimization of eddycurrent shield thickness for associated loss minimization in electrical machines," *IEEE Transactions on Industrial Applications*, vol. 42, no. 3, pp. 642–649, 2006.

[27] N. Bianchi, S. Bolognani, and E. Fornasiero, "An overview of rotor losses determination in three-phase fractional-slot PM machines," *IEEE Transactions on Industrial Applications*, vol. 46, no. 6, pp. 2338–2345, 2010.

[28] K. Yamazaki and Y. Kanou, "Rotor loss analysis of interior permanent magnet motors using combination of 2D and 3D finite element method," *IEEE Transactions on Magnetics*, vol. 45, no. 3, pp. 1772–1775, 2009.

[29] Y. Huang, J. Dong, J. Zhu, and Y. Guo, "Core loss modeling for permanent-magnet motor based on flux variation locus and finiteelement method," *IEEE Transactions on Magnetics*, vol. 48, no. 2, pp. 1023–1026, 2012.

[30] F. Luise, A. Tessarolo, F. Agnolet, and M. Mezzarobba, "Use of time-harmonic FE analysis to compute rotor eddy-current losses in synchronous machines subject to distorted stator currents," in *Proceedings of 20th International Conference on Electric Machines (ICEM)*, pp. 1503–1509, 2012.

[31] Z. Q. Zhu and D. Howe, "Instantaneous magnetic field distribution in brushless permanent magnet DC motors, Part II: Armature-Reaction field," *IEEE Transactions on Magnetics*, vol. 29, no. 1, pp. 136–142, 1993.

[32] K. Atallah, D. Howe, P. Mellor and D. Stone, "Rotor loss in permanent-magnet brushless AC machines," *IEEE Transactions on Industrial Applications*, vol. 36, no. 6, pp. 1612-1618, 2000.

[33] H. Polinder, D. Bang, R. P. J. O. M. Van Rooij, A. S. McDonald, and M. A. Mueller, "10 MW wind turbine direct-drive generator design with pitch or active speed stall control," in *Proceedings of International Conference on Electric Machines (ICEM 2007)*, vol. 2, pp. 1390–1395, 2007.

CHAPTER 7

Flooded Generator Design-II : Thermal Model and Selection of Sleeve Materials

This chapter concludes the design of the flooded generator in this thesis. The beginning of this chapter is dedicated to thermal modeling of the flooded generator. Together with the electromagnetic model presented in the previous chapter, thermal model forms an important tool-kit to provide an insight into the selection of the sleeve materials. The later part of this chapter compares different sleeve materials for the rotor sleeve.

Based on:

- F. Wani, J. Dong, A. Yadav and H. Polinder, "Comparing Different Materials for Rotor-Can in Flooded Generators," in *2018 13th International Conference on Electric Machines (ICEM'18)*, Alexandroupolis, Greece, 2018, pp. 2572–2578.
- F. Wani, J. Dong and H. Polinder, "Tidal Turbine Generators," in Clean Generators - Advances in Modelling of Hydro and Wind Generators, IntechOpen Books, London, 2020.

This chapter contains updated results.

Abstract

This chapter compares different rotor sleeve materials based on the electromagnetic and thermal performance of the generator. This is done by first presenting a thermal model for the flooded generator, which complements the electromagnetic model presented in the preceding chapter. Subsequently, different materials for the rotor sleeve are compared based on the rotor eddy current losses and the corresponding temperature distribution in the flooded generator. It is clear that materials with high electrical conductivity exhibit higher losses, and consequently higher temperature of the magnets. However, the magnitude of temperature rise is mitigated by the water present in the flooded gap, which augments the heat transfer from the rotor to stator. The main highlights of this chapter include:

- *selection of the rotor sleeve materials for the flooded generator; and*
- *understanding the effect of flooding the stator-rotor gap on the temperature distribution inside the generator.*

7.1 Introduction

The chapter begins with presenting a thermal model for the flooded generator. The objective of developing a thermal model is to aid in the selection of the sleeve materials in the flooded generator. However, before we dive into the details of the thermal model, it is imperative to briefly recap the necessary properties of the sleeve materials and the thermal limitations inside a flooded generator.

The sleeve materials must ideally be corrosion resistant, have low electrical and high thermal conductivity, along with strong water-repellent properties. However, it is difficult to find a material which possesses all these properties, and thus a study of different materials becomes necessary. Consequently, selecting the materials for the stator and the rotor sleeve forms the focal point of this chapter. Although the sleeve material must be acceptable on multiple paradigms, such as electromagnetic, thermal, structural, environmental, this thesis only considers the electromagnetic and the thermal aspects.

Protective sleeve can be made from either metallic or non-metallic materials. Non-metallic materials such as epoxy, glass fiber reinforced plastic (GFRP), and other carbon fibers have been used in some cases [1, 2]. GFRP could be an excellent candidate for protective sleeve as it is non-corrosive and electrically non-conducting, has good fatigue resistance and can be molded into complex shapes without machining. However, GFRP composites are susceptible to mechanical and electrical failure in the long term due to water ingression [3]. Thus, to provide adequate protection against water ingression, it is usually recommended to use a higher thickness of the GFRP than would be necessary for metallic materials.

However, it must be kept in mind that the effective magnetic reluctance increases with increase in the thickness of the coating material. This implies that for the same power density, volume

of magnets used increases, which increases the cost of the generator. Moreover, a relatively poor thermal conductivity of a non-conductive sleeve material might negatively influence the maximum temperature inside the generator.

On the other hand, metallic materials such as non-magnetic steels (e.g. 304L austenitic stainless steel), Inconel, and Titanium are also good candidates. Furthermore, they may also partially shield magnets from the spatial and the time harmonics of the stator field, thereby reducing the losses in the magnets. But because of their electrical conductivity, these materials add to the overall eddy current losses in the machine [4,5].

In the previous chapter, it was mentioned that using a conductive material on the stator side would result in extremely poor efficiency of the generator [6]. Therefore, it is better to select non-conductive materials for the stator sleeve[1]. In contrast, because of the potentially lower losses on the rotor side, choice of the rotor sleeve material is more flexible. Therefore, in this chapter we limit ourselves to only comparing materials for the rotor sleeve.

Different rotor sleeve materials are evaluated by comparing the eddy current losses in the rotor—sleeve as well as magnets—and the consequent temperature distribution in the generator. The temperature rise in the magnets resulting from the eddy current losses in the rotor not only reduces their remanent flux density, but may also cause irreversible demagnetization, as shown in Figure 7.1. At the other end, high temperature in the stator slots negatively influences the lifetime of the winding insulation.

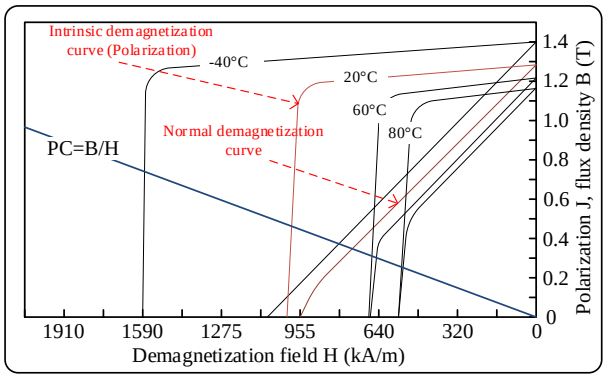

Figure 7.1 BH-curve for a NdFeB (N38) type permanent magnet (Source: Arnold magnetic technologies [7]). Permeance coefficient (PC) is the slope of the line from the origin to the operating point of the magnet on the normal demagnetization curve (BH-curve). Among other things, PC is a function of magnet and airgap dimensions.

[1] Unless non-conductive materials, such as glass fibre, fail to provide long term protection against water ingression.

Although flooded generator topology may result in a design with higher losses, it also offers an opportunity for better cooling. To understand the effect of flooding the stator-rotor gap, flooded generator is compared with a hypothetical airgap generator[2], shown in Figure 7.2. Results from this comparison, presented later in this chapter, provide a valuable guideline in the design of flooded generators.

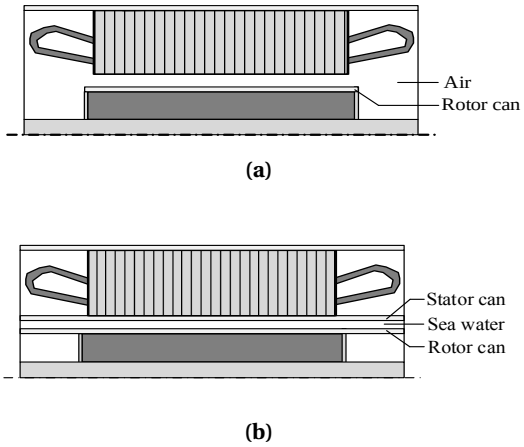

Figure 7.2 Axial cross-section of (a) a sealed airgap generator (hypothetical) , and (b) a flooded generator with stator and rotor sleeves.

Despite the potential for increased losses in the flooded generator, there is also an added advantage of having a watergap. Presence of water in the stator-rotor gap augments the heat transfer between the stator and the rotor. This happens even if the water in the gap is not continuously replenished with the ambient sea water. Whether the flow of heat is from the rotor to the stator or vice-versa depends on the temperature in the stator and the rotor, which in turn is dependent on the stator losses, rotor losses, thermal resistance in the stator-to-ambient and rotor-to-ambient (via bearing, shaft, etc.) paths.

In the next section, electrical and thermal properties of different rotor sleeve materials are presented for comparison purposes. Section 7.3 gives an abridged description of the thermal model used for the flooded generator in this thesis. In section 7.4, results from the comparison of different rotor sleeve materials are shown. Conclusions from this chapter are given in section 7.5.

[2]More like a thought experiment: we construct a hypothetical airgap machine with a rotor sleeve, although it might not be necessary in practice. This was done to highlight the cooling effect of having water rather than air in the stator-rotor gap.

7.2 Properties of different sleeve materials

Following materials for the rotor sleeve are compared in this thesis:

- Non-magnetic Stainless steel 304L
- Inconel Alloy 718
- Titanium SP 700
- GFRP C-glass

The materials chosen here have been previously considered in PM canned motors [4], and cover a wide range of thermal and electrical properties. These materials also satisfy the basic criterion of being water-proof and corrosion resistant. Their relevant electrical and thermal properties are listed in Table 7.1. As is the case usually, materials with good thermal conductivity also have higher electrical conductivity.

The materials are compared in the same 300 kW tidal turbine power take-off system with the flooded PM generator as used in the preceding chapter.

Table 7.1 Electrical and thermal conductivities for rotor sleeve materials

Material	Electrical conductivity (MS/m)	Thermal conductivity (W/mK)
Non-magnetic Stainless steel 304L	1.30	16.20
Inconel Alloy 718	0.80	11.40
Titanium SP 700	0.61	7
GFRP C-glass	0	1

7.3 Thermal models

In this section, the lumped parameter model used in the thermal analysis of the flooded PM generator is briefly outlined. The objective of this analysis is to check the effect of changing the rotor sleeve material on the magnet temperature, and also on the temperature in the stator slot.

First, a lumped element thermal network is developed for the flooded PM generator. For the airgap generator, modifications are made in the airgap. Various thermal nodes in the machine are connected by means of the thermal resistances, either determined by conduction or by convection, radiation is mostly neglected. However, some empirical convective heat transfer coefficient equations do contain some contribution due to the radiation. Later, some empirical equations are given to estimate the various heat transfer coefficients required to determine the convective thermal resistances in the thermal network model.

The thermal model presented here is based on the following premises. The main consequence of the below assumptions (except the last one) is that the heat flow in the radial and the axial directions are independent of each other.

- No axial velocity of water in the flooded gap is assumed. That is, the flow in the watergap is Taylor-Couette [8].
  In other words, the water in the stator-rotor gap is not assumed to flow freely in and out of the gap. This is because in most flooded designs some sort of debris seal would be present to prevent marine life from getting into the watergap, and/or to prevent any loss of material (or fluid) into the ocean from the machine [9].
- No heat flow in the axial direction is assumed in the stator/rotor iron because of the laminated structure.
- No axial heat flow is assumed in the stator-rotor gap as the axial fluid flow is restricted. This is a reasonable assumption to make in direct-drive low speed machines [10]. Under this assumption, the convective heat transfer coefficient is underestimated.
- Internal heat generation in regions inside the PM generator, wherever it occurs, is treated as uniform. Whereas this is more or less always true for windings, in magnets it may not be true. Eddy current losses inside the magnet, especially the ones caused by the switching harmonics, may only occur over a part of the magnet volume [11].

7.3.1 Thermal network

A highly accurate thermal modeling of electrical machines requires complex methods, such as finite element analysis and computational fluid dynamics. But for most practical purposes, a lumped element thermal network gives reasonable enough results to compare different designs/materials. Detailed lumped element thermal network model for PM machines can be found in multiple references such as [10, 12]. In this thesis, only a brief overview is presented, with appropriate modifications made for the flooded generator wherever necessary.

An example of the thermal network in the stator slot is shown in Figure 7.3. In a flooded generator, there are two additional nodes compared to an airgap generator. The additional nodes correspond to the stator and the rotor sleeves. The rotor thermal network is illustrated in Appendix A.1.

7.3.2 T-equivalent block

Some parts of the PM generator act both as a thermal resistance and a heat source, e.g. copper coil and stator iron. Thermal network nodes corresponding to these parts are modeled using a T-equivalent block [10, 12]. It must be noted that T-blocks are only good for low-level discretization. The benefits of having additional nodes (from T-block) decrease with the increase in discretization; thus reverting to conventionally defined thermal resistances is preferred in highly discretized thermal networks [10]. A brief explanation for the T-equivalent blocks is given below.

Consider a block of material as shown in Figure 7.4. If this material has no internal heat generation, then the average temperature is the mid-point temperature of the block. However, with internal heat generation, the average temperature obtained by adding a current source at node T_{mid} alone does not suffice. The average temperature is more accurately represented by the T-block, where

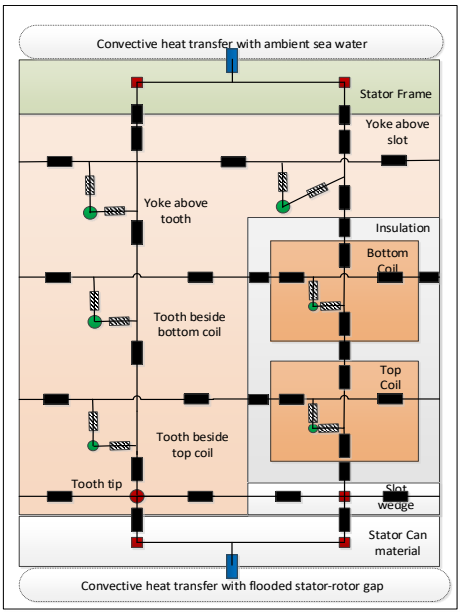

Figure 7.3 Lumped element thermal network (condensed form) representing the radial flow of heat in the slot of the PM generator with a double-layer winding. This can be modified to accommodate single-layer winding. Green dots represent the nodes where heat loss occurs; red dots represents a node with no heat generation. Thermal resistances corresponding to the conduction and convection heat transfer are represented by black and blue boxes respectively. Boxes filled with inclined black lines represent the hypothetical thermal resistance, which follows from the T-equivalent model. This figure does not show any axial thermal resistances. Parameterized values for the thermal resistances in this network can be found in [12].

the current (heat) source is connected to T_{mid} via a hypothetical resistance R_3. For proof of the T-equivalent block, see [11].

7.3.3 Convective heat transfer coefficients

When a solid surface is in contact with a fluid, the thermal resistance at the interface is calculated using the heat transfer coefficients. Accurate estimation of these heat transfer coefficients is perhaps the most difficult task in the thermal modeling of electrical machines. In this thesis, however, it suffices to adhere to the empirically derived equations to calculate these coefficients.

For a flooded PM generator, heat transfer coefficients are used at the following interfaces.

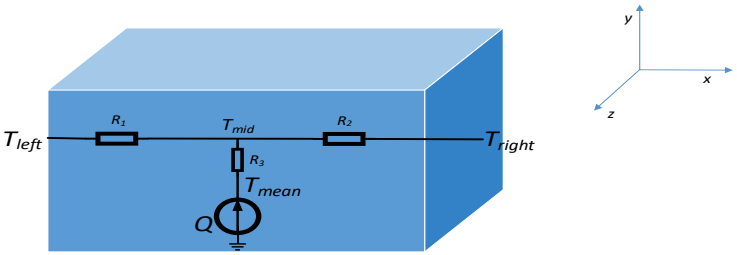

Figure 7.4 T-equivalent model for a block with internal heat generation. The figure only illustrates one-dimensional heat conduction. Similar T-blocks must be made for all three dimensions independently, if applicable. T_{left} and T_{right} represent the temperatures at the left and the right face of the block respectively. With internal heat generation, Q, mean temperature, T_{mean}, is given by the temperature at the node between the current source and hypothetical thermal resistance, R_3. For a rectangular block, $R_3 = -\frac{1}{3}R_1$, where $R_1 = R_2$ [12].

In the watergap

In low speed generators with no forced cooling, heat from the rotor is mostly evacuated from the stator housing via the watergap, unless the rotor shaft provides a low resistance path. The heat transfer coefficient in the watergap, α_g is a function of the Nusselt number (Nu) such that,

$$\alpha_g = \frac{Nu \cdot \lambda}{d_h}, \tag{7.1}$$

where λ is the thermal conductivity of the water in the watergap and d_h is the hydraulic diameter. Nusselt number is a function of the fluid properties as well as the physical dimensions related to the fluid flow. The equations to determine the Nusselt number in (7.1) are based on the Taylor number; details are mentioned in [10].

Stator housing to ambient water

In a pod-type tidal turbine shown in Figure 1.2, the velocity of the water on the stator housing surface of the generator is different from that of the free flow tidal velocity. The heat transfer coefficient at the outer surface increases with the fluid velocity. As a conservative approach, we determine the heat transfer coefficient assuming natural convection[3] at the stator housing surface. In any case, this thermal resistance is much lower than the other thermal resistances in the radial direction inside the machine. Thus, assuming natural, rather than forced, convection does not make significant difference in the temperature estimation inside the machine.

The heat transfer coefficient at the outer surface of the stator housing is again found using the

[3] assuming stationary water

Table 7.2 Heat transfer coefficients used in the generator thermal models

Interface	**Heat transfer coefficient (W/m^2·K)**
In watergap	570
Stator outer frame to Ambient water	280
End shield to ambient water	60
In the airgap (when watergap is replaced with airgap)	20

Nusselt number as follows,

$$\alpha_{so} = \frac{Nu \cdot \lambda}{D_{ext}}, \tag{7.2}$$

where D_{ext} is the external diameter of the stator housing [13]. The Nusselt number calculation in (7.2) is different from the one used in (7.1), because of the different nature of fluid flow. In (7.2), Nu is calculated from the Grashof and the Prandtl numbers given in [14].

Calculation of the heat transfer coefficients at the end shields to the ambient water interface can be determined using the similar approach as in (7.2). However, the equations for the Grashof and the Prandtl numbers would be different for the end-shields. Again, the appropriate equations can be found in any heat transfer textbook, such as [13]. Heat transfer coefficients calculated for the PM generator in this chapter are listed in Table 7.2.

End-winding to end-shield

In a flooded generator, the airflow around the end windings due to the rotor motion is blocked by the protective sleeves, see Figure 6.2. Therefore, the heat transfer coefficient near end windings is rather small. For this reason a conservative heat transfer coefficient value of 6 W/m^2·K has been used[4]. In conventional airgap machines, without sleeves, this value is normally between 15-40 W/m^2·K [13, 15]. Knowing all these heat transfer coefficients, the thermal resistances R_{th} at the corresponding interfaces, with surface area, A is calculated using the equation,

$$R_{th} = \frac{1}{\alpha A} \tag{7.3}$$

In the thermal model, an ambient water temperature of 20°C has been assumed. Other parameters used in the thermal model have been listed in Appendix A.2 at the end of this chapter.

7.4 Results

The eddy current losses in the rotor sleeve and the magnets for different rotor sleeve materials are listed in Table 7.3. As an example, the induced eddy current loss density in the stainless steel rotor

[4] End-windings in flooded generators may be immersed in pressure compensating fluids, such as oil, which may facilitate heat transfer to end-shields. However, we have not taken that into account in this thesis to simpify calculations.

sleeve and the magnet is shown in Figure 7.5. It is observed that the eddy loss density in the rotor sleeve is about two orders of magnitude higher than that of the PM. Furthermore, we see that for higher rotor sleeve conductivities magnet losses decrease (albeit slightly), as seen in Table 7.3. This is because of the shielding effect of the rotor sleeve. The permanent magnet temperatures corresponding to different rotor sleeve materials are shown in Figure 7.6. The temperatures corresponding to the stainless steel rotor sleeve is the highest because of higher losses in this case.

Table 7.3 Rotor eddy current loss for the 300 kW generator

Material	**Loss in rotor sleeve (kW)**	**Loss in magnets (kW)**
Non-magnetic stainless steel 304L	10.9	0.757
Inconel alloy 718	7.78	0.770
Titanium SP 700	5.39	0.773
GFRP C-glass	0	0.777

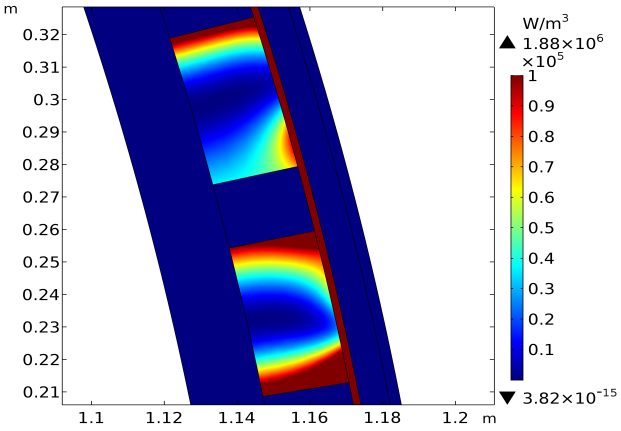

Figure 7.5 Eddy loss density distribution in the rotor sleeve and one pole-pair permanent magnet (Rotor sleeve material: stainless steel 304L). Figure is repeated here from the previous chapter.

To assess the impact of the watergap on the magnet temperatures, the watergap was replaced with an equivalent airgap, and the temperatures were re-evaluated. It was assumed that under both these cases, the losses in the PM generator remained the same. However, in the airgap generator no stator GFRP coating was deemed necessary, and so was eliminated from the thermal model, replacing it with an equal thickness of the airgap. It is estimated that in the absence of flooding, the temperature rise in the magnets would be much higher, as is seen in Figure 7.6.

Interestingly, a deviation from this trend was observed in the case of the GFRP rotor sleeve. In

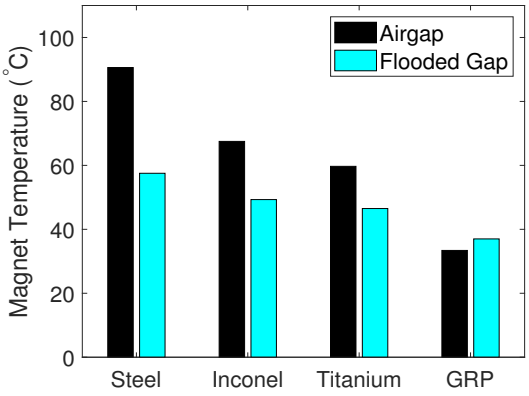

Figure 7.6 Temperature inside Permanent Magnet for different rotor sleeve materials. Cooling effect of flooded gap is clearly evident.

other words, when the rotor is covered with a GFRP coating, the magnet temperature increases rather than dropping on flooding the gap with sea water. This counterintuitive behavior can be explained as follows.

The watergap is partly responsible for evacuating the heat from the stator through the rotor, thereby resulting in a slight increase of the temperature in the magnets. This is because of the better heat transfer coefficient in the watergap compared to the airgap, see Table 7.2. However, there are other factors also at play here. The amount of heat that will be transferred to the rotor from the stator will also depend on overall thermal resistance from the rotor to the ambient sea water(including bearings and shaft), and the total rotor losses. For instance, if for the same thermal resistances in the rotor, magnet losses were higher (almost similar to losses in sleeve), in that case too the magnet temperature would have dropped upon flooding. This is shown in Figure 7.7, where a sensitivity analysis is performed with respect to the magnet conductivity for the GFRP coating. The point of inflection in temperature reversal depends on the total rotor losses and the thermal resistances in the rotor-to-ambient path.

As far as the temperature in the stator slots is concerned, the effect is opposite to that in the magnets, as seen in Figure 7.8. That is, in the flooded case the temperature in the slot is slightly higher than that of the airgap case. Again this is because of the better heat transfer capability of the watergap, which transfers rotor losses more effectively to the stator. As expected, for the GFRP case, where the heat flows from the stator to the rotor, the trend is reversed for the same reason as above.

As illustrated from Figures 7.6 and 7.8, the difference in the stator slot and the rotor magnet temperature is lower in the flooded generator as compared to the airgap generator (with the same rotor sleeve material). While magnet temperatures drop significantly on flooding, the slot temperature increases only slightly. This is because the primary heat evacuation path from the stator slot is via the stator iron and the stator housing to the ambient sea water. Thus, the presence

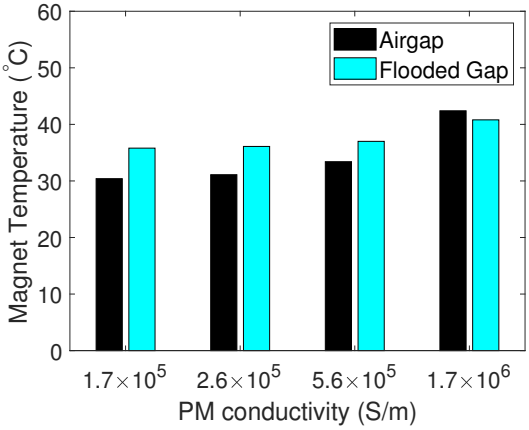

Figure 7.7 Temperature of Permanent Magnet for different PM conductivities, under flooded gap and airgap, with GFRP coating on the rotor.

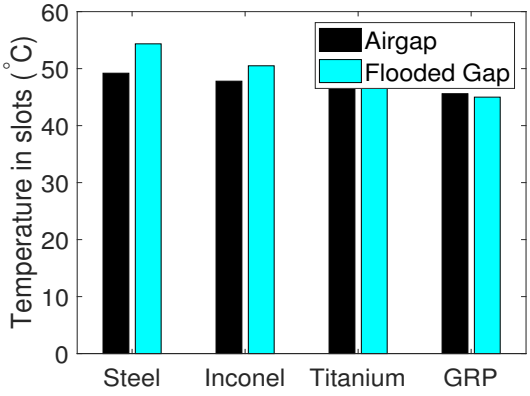

Figure 7.8 Temperature in the stator slots for different rotor can materials.

of water in the stator-rotor gap may result in either the increase of average temperature of the stator or rotor. This is provided that all the external thermal impedances remain the same.

The results presented in this chapter are based on the assumption that water in the stator-rotor gap is not exchanged with the sea water. If this is made possible, it will likely reduce the temperature of both the stator and the rotor in a flooded gap generator. However, such a design might compromise reliability of the generator.

Please note that the values given in this section correspond to a particular machine design, which is unlikely to be the 'optimal' design. It is possible to design machines with different dimensions, where the rotor losses can be further minimized with same materials. On the other hand, the

conclusions drawn regarding the choice of the materials, and the flooded gap are likely to hold in other designs as well, albeit with different values and points of inflection.

For the correct choice of the rotor sleeve material, studies should be conducted based on water-proofing properties of different materials, required sleeve thickness, structural integrity of the material, and the ease of manufacturing together with the rotor of the generator.

7.5 Conclusion

This chapter began with briefly outlining the thermal model for the flooded generator. The objective of the thermal model was to aid in the selection of rotor sleeve materials. Materials with higher conductivity exhibited higher eddy current losses. However, the corresponding temperature rise in the magnets was less than expected because of the flooded stator-rotor gap. In a corresponding airgap machine, the temperature rise in the magnets because of the rotor losses would have been much higher. This means that from the thermal viewpoint, magnets are at a lower risk of demagnetization in a flooded generator. The lowering of the demagnetization risk can be ascertained by following the knee-point in the magnet BH-curve at different operating temperatures, as shown in Figure 7.1.

Results also indicate that the temperature in the flooded PM generator is more evenly distributed than in a similar airgap PM generator. However, similar analysis must be made for machines of different ratings and sizes, for this conclusion to be generalized. Flooding of the gap might actually increase the temperature inside the stator slots, as more heat from the rotor is evacuated via the stator than from the rotor shaft. Ideally, if sufficient water ingress protection and mechanical robustness is assured over the lifetime of the flooded PM generator, it is better to use materials such as glass or carbon fibers as sleeve material. Otherwise, a lifetime cost analysis must be carried out with respect to the thickness of the rotor sleeve material, and the associated eddy losses therein.

Appendix

A.1 Rotor thermal network

The rotor thermal network for the flooded generator with conductive rotor sleeve and surface permanent magnets is shown in Figure 7.9. This is very similar to the stator slot network shown in Section 7.3.1 . The main difference being that in the shaft heat is axially transported to the ends of the generator. The magnets are attached to the rotor iron by means of glue, whose thermal resistance must also be accounted for. In case the rotor sleeve is non-conductive, it must be represented by simple resistances without the need for T-equivalent blocks. Parameterized values for the thermal resistances shown in Figure 7.9 can be found in [12].

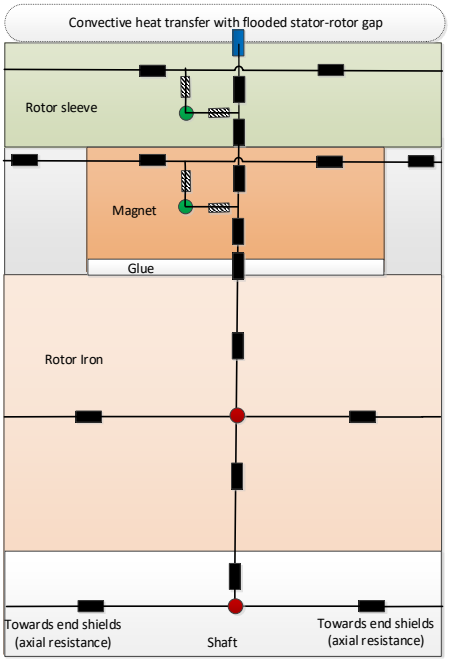

Figure 7.9 Lumped element thermal network (condensed form) mainly representing the radial flow of heat in the rotor of the PM generator with surface PMs and a rotor sleeve (with eddy current losses). Green dots represent the nodes where heat loss occurs; red dots represents a node with no heat generation. Thermal resistances corresponding to the conduction and convection heat transfer are represented by black and blue boxes respectively.

A.2 Parameters for thermal modeling

Table 7.4 Parameter values used in thermal modeling

Parameter	Value
Thermal conductivity of water	0.7 (W/m·K)
Thermal conductivity along the coil	400 (W/m·K)
Thermal conductivity through the coil	1.8 (W/m·K)
Thermal conductivity of magnets	7.6 (W/m·K)
Thermal conductivity of the magnet glue	0.7 (W/m·K)
Thermal conductivity of insulation	0.2 (W/m·K)
Thermal conductivity of iron in the lamination plane	28 (W/m·K)
Thermal conductivity of stator housing frame	205 (W/m·K)
Frame thickness	20 mm
Air-film contact thickness between stator frame and stator yoke	0.0015 mm

Bibliography

[1] L. Drouen, J. F. Charpentier, E. Semail, and S. Clement, “Study of an innovative electrical machine fitted to marine current turbines." OCEANS 2007-Europe. IEEE, 2007.

[2] O. Krovel, R. Nilssen, S. Skaar, E. Lovli, and N. Sandoy, “Design of an Integrated 100kW Permanent Magnet Synchronous Machine in a Prototype Thruster for Ship Propulsion,” in Proceedings of ICEM, 2004, pp. 4–9.

[3] L. Bian, J. Xiao, J. Zeng, and S. Xing, “Effects of seawater immersion on water absorption and mechanical properties of GFRP composites,” Journal of Composite Materials, vol. 46, pp. 3151-3162, 2012.

[4] Y. Burkhardt, G. Huth, and S. Urschel, “Eddy current losses in PM canned motors,” 19th International Conference of Electrical Machines, pp. 1-7, 2010.

[5] Q. Yu, X. Wang, and Y. Cheng, “Electromagnetic Calculation and Characteristic Analysis of Can Effect of a Canned Permanent Magnet Motor,” IEEE Trans. Magnetics, vol. 52, pp. 1-6, 2016.

[6] A. Yadav, “Finding suitable material for the retaining sleeves in tidal generators,” Master Thesis, Delft University of Technology, Netherlands, 2017.

[7] Arnold Magnetic Technologies, “Sintered Neodymium-Iron-Boron Magnets N38,” https://www.arnoldmagnetics.com/wp-content/uploads/2017/11/N38-151021.pdf, [Online; Last accessed 20-Sep-2020].

[8] M. Hosain, R. Fdhila and R. Kristian, “Taylor-Couette flow and transient heat transfer inside the annulus air-gap of rotating electrical machines,” Applied Energy, vol. 207, pp. 624-633, 2017.

[9] B. Holstein and N. Perner, “Submersible Power Generating Plant, Driven by a Water Flow,” United States Patent, US 8,410,626, Apr. 2013.

[10] J. Nerg, M. Rilla and J. Pyrhonnen, “Thermal Analysis of Radial- Flux Electrical Machines With a High Power Density,” IEEE Trans. Industrial Electronics, vol. 55, no. 10, pp. 3543–3554, 2008.

[11] A. Grobler, “Thermal modelling of a high speed permanent magnet synchronous machine,” PhD Dissertation, North-West University, 2011.

[12] A. Grauers, “Design of Direct Driven Permanent Magnet Generators for Wind Turbines,” PhD Dissertation, Chalmers University of Technology, 1996.

[13] A. Cengel and A. Ghajar, *Heat and Mass Transfer, Fundamentals & Application, Fifth Edition in SI Units*, McGraw-Hill, New York, 2014.

[14] D. Staton and A. Cavagnino, “Convection heat transfer and flow calculations suitable for electric machines thermal models,” IEEE Trans. Industrial Electronics, vol. 55, no. 10, pp. 3509–3516, 2008.

[15] A. Boglietti, A. Cavagnino, D. Staton, M. Shanel, M. Mueller, and C. Mejuto, “Evolution and Modern Approaches for Thermal Analysis of Electrical Machines,” IEEE Trans. Industrial Electronics, vol. 56, no. 3, pp. 871–882, 2009.

CHAPTER 8

Conclusions and Recommendations

This chapter is divided into two sections. The first section covers the conclusions from this thesis. This is followed by the section on the recommendations for future research in tidal stream turbines.

8.1 Conclusions

Major renewable sources of energy—wind and solar—are variable and less predictable. Unpredictability implies increasing the balancing costs in energy generation. Due to its predictability, tidal energy reduces the storage requirements in the system. Furthermore, tidal turbines are out of view which makes them less prone to public objection unlike solar panels and wind turbines.

To a certain extent there is a consensus on the type of technology (horizontal axis turbines) that should be used in tidal stream turbines. The main challenge is to reduce the levelized cost of energy (LCOE). Reducing the maintenance expenses and downtime have been identified as pivotal points of action to tackle this challenge. It is on this basis that this thesis was envisaged. The idea was to select the tidal stream turbine system with the highest technology readiness level, and identify ways to improve the reliability.

In this thesis we focused on improving the reliability of the power take-off system by proposing potentially more reliable solutions than the state-of-the-art systems. Unfortunately, the margin of reduction in LCOE—as a consequence of these proposed solutions—was beyond the scope of this thesis. However, other studies conducted under the TiPA project, of which this thesis is a part, did report/estimate that a cost reduction of 29% was possible with the flooded generator and submerged converter[1].

[1] See `https://www.tipa-h2020.eu/`

What approaches did this thesis suggest to improve the reliability of tidal stream turbine power take-off systems?

This thesis focused on the two main components of the power take-off system: the generator and the power converter. The objective was to identify ways to improve the reliability of these components to improve the overall reliability of the tidal stream turbine system. Below we describe these approaches, and answer the relevant questions posed in Chapter 1.

- *Power converter:* to improve the reliability of the converter, this thesis proposed the use of the passively cooled power electronic converter and investigated its feasibility assuming thermal cycling as a predominant failure mode.
- *Generator:* to analyze the benefits and challenges of using the flooded generator.

Under the ambit of these proposed solutions, we posed certain research questions in the Introduction chapter to define the scope of this thesis. The answers posited to each of those questions follow the corresponding question below.

Given the bulk of this thesis deals with the converter reliability, converter is dealt before the generator in the rest of this section. This outline is also consistent with the overall layout of the thesis.

8.1.1 Power converter

The diode on the generator side converter—in the two-level back-to-back converter—was found to be the most critical component in terms of lifetime. Consequently, the lifetime of the converter was defined as the lifetime of the generator side converter diode. The answers to the following questions must be seen in this context.

How important is the role of turbulence and waves in determining the converter lifetime?

Turbulence and surface waves were found to impart significant thermal loading on the IGBT modules, and thus contribute substantially to the reduction in lifetime. Although the fluctuations due to turbulence or surface waves do not add much to the annual losses, the temperature swing owing to these speed oscillations results in reducing the lifetime. In the case of a passively cooled converter in a 110 kW active speed stall-controlled turbine, IGBT module lifetime considering turbulence and waves was about four times lower than without turbulence and waves.

How does active speed stall control influence the converter lifetime?

Beyond the rated tidal speed, in the constant power region, the current loading on the converter is higher in the active stall-controlled turbine compared to the pitch-controlled one, for the same rated power and speed. This means losses in the IGBT modules of the active stall-controlled turbine are higher. Furthermore, similar oscillation in tidal stream speed cause higher generator speed fluctuations in the stall-controlled turbine. These reasons contribute to the higher junction temperature oscillations in the generator side converter diode. As a result, converters in active

stall-controlled turbines exhibit lower lifetimes than their counterparts in pitch-controlled turbines. For the 110 kW case study in this thesis—while assuming forced water cooling and 1200 V, 600 A IGBT module—IGBT lifetime with active stall control was about 500 times lower than with pitch-controlled turbine.

It must be noted though that the above statements are valid for the same IGBT module rating and technology used in both the turbines. Ideally, IGBT rating for the pitch-controlled turbine must be rated lower than the corresponding switch in the active stall-controlled turbine converter. For the 110 kW case investigated in this thesis, active stall-controlled turbine required an IGBT with a rating of 600 A, whereas 400 A IGBT would have sufficed for the pitch-controlled turbine.

Is passive cooling by ambient sea water a feasible option over active cooling in a submerged power converter?

It was shown that passively cooled converter modules can be designed to last beyond 25 years, which is considered a typical lifetime of tidal turbines. In a passive system, minimizing thermal spreading resistance is the key to reducing the net thermal resistance. Thus, the design of the mounting plate and the placement of modules inside the enclosure appear critical.

Active cooling methods—we mean forced water cooling here—provide lower sink-to-ambient thermal resistance and dynamic control compared to passive cooling systems. Besides high cooling efficacy, active cooling methods offer control variables, such as flow rate of the coolant, to further reduce thermal cycling by adaptively cooling the heat sink. This feature is especially useful for low frequency thermal cycling. In the context of tidal turbines, thermal cycling due to surface waves and turbulence can be further mitigated. The exact magnitude of the improvement in lifetime from adaptive methods would depend on pump control system, thermal parameters of the cooling system, etc. For instance, in the active stall-controlled 110 kW turbine investigated in this thesis, a lifetime improvement of 50% or more could be achieved[2].

Comparison of passive with active cooling systems corroborate that using active cooling systems will likely result in improvement of estimated IGBT module lifetime. This result is irrespective of whether the turbine is controlled by active speed stall or pitch mechanism.

The main disadvantage of the active cooling system involves breakdown of mechanical components such as pumps, coolant leakage, etc. Although driving a suitable coolant fluid using magnetohydrodynamic principle, without using conventional pumps, is also possible, such systems are rarely in application as of now.

Using overrated IGBT modules appears to be the simplest way of improving the lifetime, whether an active cooling or a passive cooling system is used.

[2] This figure of 50% was not calculated in this thesis, but is a guesstimate based on other studies conducted for wind turbines.

8.1.2 Generator

How does the design of flooded generators differ from that of airgap generators?

In terms of design, an additional layer of material (can or sleeve) is needed to protect the active generator parts from corrosion, insulation breakdown, etc. One such layer must be placed on the stator inner diameter encasing the windings and the stator iron. Another layer is placed on the rotor outer diameter engulfing the rotor iron and the magnets. Presence of sleeves has a two-fold effect, as far as electromagnetic aspects are concerned. Firstly, the effective magnetic arigap length increases. Secondly, if any one of these layers is electrically conductive, additional losses occur in the generator.

The free space between the stator core, winding overhang and the stator sleeve must be filled to minimize pressure stress on the stator sleeve. This can either be done by filling this space with oil or with material such as epoxy resin.

Due to the watergap, the effective heat transfer between the stator and the rotor improves. This means more even distribution of heat inside the flooded gap generator than airgap generator. However, this does not necessarily mean lower temperatures throughout the machine. In other words, in a flooded gap design with no free flow of water in/out of the generator, reduction in the rotor temperature will be accompanied by the rise in stator temperature or vice-versa.

What materials and winding configurations could be used in flooded generators?

The stator sleeve should ideally be made out of electrically non-conductive and non-magnetic material. It is also possible to use an electrically conductive material such as stainless steel. However, this choice is likely to compromise the generator efficiency significantly because of the eddy current losses. On the other hand, rotor sleeve needs to be non-magnetic (unless it is highly saturated). Eddy current losses in the rotor sleeve are much lower than in the stator sleeve. Furthermore, a proper selection of the stator winding layout can significantly reduce the possible rotor losses. For instance, distributed windings can cause lower losses than concentrated windings.

Briefly put, whereas it is possible to use a metallic material as the rotor sleeve, it should be avoided for the stator sleeve unless absolutely necessary.

8.2 Recommendations for future research

Recommendations for the future research are broadly proposed within two categories. The first category is concomitant to the studies done in this thesis. The other category mentions the unexplored areas; however, the list is by no means exhaustive.

8.2.1 From this thesis

- Little data is available on the failure causes of submerged power converters. Whereas moisture has been identified as one of the main failure modes in wind turbine converters, whether it will be the same in submerged converters needs to be investigated.

- It needs to be seen if the converter reliability can be improved by filling the converter enclosure with gases like nitrogen or dehumidified air instead of normal air.

- If indeed thermal cycling is the main failure mode in submerged converters, reliability of sintered power modules over bonded power modules should be examined.

- Magnetohydrodynamic (MHD) pump-driven forced liquid metal cooling systems should be probed to assess their feasibility over conventional pump-driven systems.

- Turbulence and surface waves were shown to reduce the IGBT module lifetime. It must be examined whether advanced control methods, like fractional-order PI control, which include disturbance rejection algorithms may prove helpful in improving the converter lifetime.

- Stall-related turbulence effects were neglected in this thesis. These effects may induce even more speed oscillations of the generator, and cause more thermal cycling in IGBT modules. This must be investigated in future.

- Lifetime models for power modules used in this thesis involved standard statistical models published in literature. Often components are selected by incorporating factors of safety which are generally based on rules of thumb. Further cost reductions or reliability improvement can be achieved if uncertainty analysis in loading and strength parameters is done.

- This thesis only considered the effects of waves and turbulence on converter lifetime. These effects must also be investigated in terms of blade/rotor lifetime. It is likely that a conjunction of such studies will help in identifying important design trade-offs.

- Practical studies must be conducted to evaluate the reliability improvement offered by flooded generator over the airgap generators. Only when the cost of reliability is known, can we truly say that flooded generators are a better solution in the long run.

- It remains to be seen if the reliability of seals and bearings in the tidal turbines can be assumed to be similar to that of marine propellers. Such studies will help in identifying the most critical component in terms of reliability for tidal turbine systems.

- An exhaustive study must be conducted on the impact of using pitch and stall control (both active and passive) on the LCOE. It is likely that one mechanism might be more suitable upto a certain power level, and the other beyond that level.

8.2.2 Other recommendations

- While reliability analysis of individual components is a worthwhile pursuit, it is even more important to do a system level reliability analysis to identify the most failure prone components. It is also plausible that the critical components might differ for an individual turbine and an array installation.
- Improving reliability is a valuable endeavor only as long as the cost of improving reliability (either monetarily or in terms of carbon emissions) is affordable. Therefore, it is imperative that future reliability studies provide the cost of reliability to a reasonable degree of confidence.
- Fault-tolerant designs for generators and converters must be studied, and their impact on LCOE quantified. For example, multi-phase topologies and modular designs could be a possibility.
- Deconstructing the maintenance costs into component replacement, labor, downtime and logistic costs could provide a good insight into minimizing LCOE.
- Identifying optimum turbine power rating, drive train topology and number of turbines for a particular tidal site could be an interesting study to undertake.
- Similar studies to the one conducted in this thesis may be done for floating tidal turbines. Floating turbines experience different loading paradigms, and probably have different contributions of O&M costs and capital costs towards the LCOE.

List of Publications

Thesis related publications

- F. Wani, U. Shipurkar, J. Dong and H. Polinder, "A Study on Passive Cooling in Subsea Power Electronics," in *IEEE Access*, vol. 6, pp. 67543–67554, 2018.
- F. Wani, U. Shipurkar, J. Dong, H. Polinder, A. Jarquin-Laguna, K. Mostafa and G. Lavidas, "Lifetime Analysis of IGBT Power Modules in Passively Cooled Tidal Turbine Converters," in *Energies*, vol. 13 (8), 2020.
- F. Wani, U. Shipurkar, J. Dong and H. Polinder, "Thermal Cycling in Converter IGBT Modules with Different Cooling Systems in Pitch and Active Stall-Controlled Tidal Turbines," *under review*.
- F. Wani, J. Dong and H. Polinder, "Tidal Turbine Generators," *Clean Generators - Advances in Modelling of Hydro and Wind Generators*, Intech Open, London, 2020.
- F. Wani, U. Shipurkar, J. Dong and H. Polinder, "Calculation of PWM-Induced Rotor-Can Losses in Flooded Generator," *2019 13th European Wave and Tidal Energy Conference (EWTEC'19)*, Napoli, Italy, 2019, ISSN 2309-1983, pp. 1451-1-6.
- F. Wani, J. Dong, A. Yadav and H. Polinder, "Comparing Different Materials for Rotor-Can in Flooded Generators," in *2018 13th International Conference on Electric Machines (ICEM'18)*, Alexandroupolis, Greece, 2018, pp. 2572–2578.
- F. Wani, J. Dong and H. Polinder, "Fast Rotor Loss Calculations in Fractional-Slot Permanent Magnet Machines," in *2018 13th International Conference on Electric Machines (ICEM'18)*, Alexandroupolis, Greece, 2018, pp. 1201–1206.
- F. Wani and H. Polinder, "A Review of Tidal Current Turbine Technology: Present and Future," *2017 12th European Wave and Tidal Energy Conference (EWTEC'17)*, Cork, Ireland, 2017, pp. 3707-3712.

Other publications

- F. Wani, X. Wang, D. Lahaye and H. Polinder, "3D FEM computation of axial flux in a brushless doubly-fed Induction Machine," in *2017 IEEE International Magnetics Conference*, DOI:10.1109/INTMAG.2017.8008028, INTERMAG 2017 - Dublin, Ireland .
- Z. Cao, J. Dong, F. Wani, H. Polinder, P. Bauer, F. Peng and Y. Huang, "Sliding Mode Control with Neural Network for Active Magnetic Bearing System," *IECON 2017 - 45th Annual Conference of the IEEE Industrial Electronics Society*, Lisbon, 2019, pp. 744-749.
- U. Shipurkar, F. Wani, Z. Qin, J. Dong, H. Polinder and J. A. Ferreira, "Adaptive Cooling for Improved Power Semiconductor Lifetime in Wind Turbine Converters," submitted to *IEEE Journal of Emerging and Selected Topics in Power Electronics*, under review.
- A. Haseltalab, F. Wani and R. Negenborn, "Multi-Level Model Predictive Control for Power Generation on All-Electric Ships," submitted to *IEEE Transactions on Industrial Electronics*, under review.
- M. Desmedt, J. Dong, F. Wani, P. Bauer and H. Polinder, "Electromechanical Dynamics Analysis of Pole-Piece Rotors in Pseudo Direct-Drive Wind Turbine Generators," *ICEM 2020*, Stockholm, 2020.

- U. Shipurkar, F. Wani, J. Dong, G. Alpogiannis, H. Polinder P. Bauer, and J. A. Ferreira, "Comparison of modular wind turbine generators considering structural aspects," *IECON 2017 - 43rd Annual Conference of the IEEE Industrial Electronics Society*, Beijing, 2017, pp. 3707–3712.

Acknowledgements

To begin with, I would like to express my profound gratitude to my promotor, Henk Polinder. His scientific excellence as well as personal values have inspired me. Henk has always encouraged an independent and innovative attitude towards research. This work would not have been possible without his support and his belief in my capabilities. I would be amiss not to mention Clarisa here. I am grateful to both Henk and Clarisa for all the happy memories and wonderful conversations we have had at their place.

My copromotor, Jianning Dong, has provided valuable support and guidance throughout the duration of this work. I have thoroughly enjoyed and benefited from our stimulating deliberations and conversations on diverse topics—from engineering to politics to poetry.

I would also like to convey my appreciation towards Professors Jean-Frederic Charpentier, Simon Watson, Rudy Negenborn and Bram Ferriera, who invested valuable time and efforts in the evaluation of this thesis. Their constructive feedback has indeed enriched this work. I would also like to thank Gary Connor for showing great interest in my work and providing valuable comments to improve it.

Over the past few years, I have had the opportunity to discuss my research ideas with Professor Hans Hopman. His inputs have been a source of course correction and motivation, for which I remain grateful. I am also thankful for the indispensable support of the secretaries at our department—Dineke, Anouk, Patty, Monique, Pauline and Gracia—who make life so much easier for all the PhD candidates.

This thesis would not have evolved without the support of the partners in the TiPA project, especially Nova Innovation. I sincerely recognize the value of the feedback they provided on this work. I must especially mention: Lisa Ferrero, Gavin Mcpherson, Lindsey Entwistle, Neil Simpson, Seumas Mckenzie and Colin Walker (Nova Innovation), Tobias Duda and Dennis Bosse (RWTH Aachen); Kaswar Mostafa, Miguel Santos-Herran and Professor Markus Mueller (University of Edinburgh). Many thanks to project partners at Siemens and SKF for all the knowledge exchange during the TiPA project.

I would also like to thank my colleagues at the department of Maritime & Transport Technology for rendering these years memorable. My working space came to life with the constant presence of Lode and Harsh, both of whom have been great colleagues and friends. Our discussions and arguments will last long in my memory. My time at the department became all the more enjoyable in the company of people like Pranav, Breno, Jian, Wang Kai, Wenjing, Marc, Ali, Hamid, Lindert, Erik, Roelf, Nikos, Minxing, Zongchen, Johan, Qinqin, Alina, Javad, Peter and Klaas Visser.

I have also had the pleasure of knowing Udai Shipurkar. Udai has been an amazing colleague, is a cherished friend and the collaboration with him has been rewarding. My sincere appreciation

also goes to Antonio Jarquin-Laguna and George Lavidas for collaborating with me, and for all the thoughtful discussions on my work.

Although it eventually culminated at 3mE, my PhD journey started at the faculty of EWI. During the masters and the initial period of my PhD at EWI, I have come across wonderful people whose friendship will always be cherished. Nils, Pavel, Xuezhou, Gautham and Nishant—have been a source of motivation and a joyful company. Soumya must be thanked for all the nice food and updates on current affairs, memes and film recommendations (or not). My deepest thanks to Harrie Olsthoorn, Joris Koeners, Bart Roodenburg and Sharmila Rattansingh for all the support, technical and otherwise, during my time at EWI.

My time in Netherlands would not have been great without the companionship of Mirko, Haris, Jaffer, Yuan, Madeeha and Karishma. I have been lucky to have them around—especially during the pandemic—and will always be grateful for their friendship. For someone passionate about Urdu poetry, it is difficult to find a fellow enthusiast in Delft, but I was lucky to have Siddhartha's company. I have enjoyed our poetry sessions and look forward to more in future. My sincere thanks also goes to my kind and lovely housemates—Yusaf and Sanjay—for their warm and reassuring presence.

I would also like to acknowledge the encouragement from my teachers in my formative years, especially Faisal Khan, Inayat Bhat, Venkata Kirthiga and Raja Pitchaimuthu. Their influence ensured that I enjoyed doing science and electrical engineering in the first place.

Any amount of praise and appreciation for my friends, Omar and Burooj, would be less than they deserve. I can never repay them for all the support, love, kindness, feedback, patience and counsel—even when I did not listen to them. I am also indebted to Farooq uncle and Shahida aunty for their affection and prayers. The friendship and support of Tabish Parray, Umar Rashid, Domenico Lahaye and Melanie, Rizwan, Mohsin, Fahim, Saliha, Farhat, Anha, Talha and Faizan will always be remembered. My heartfelt thanks to Uzma Falak for being a good friend, an inspiration and also for proofreading parts of this thesis. I hold her friendship dear, and her contributions shall never be forgotten.

I have been lucky to have the affection and backing of my lovely siblings, Mehak and Aamir. Despite I being the elder brother, it would not be wrong to say that they have been more caring towards me. To my little cousins, especially Burhaan, thank you for all the endearing ways in which you express your affection, and for creating a happy distraction from the rigours of life.

At the risk of sounding clichéd, I am grateful for the endless love, tireless prayers and selfless support of my wonderful parents, Rehana and Mushtaq Ahmad Wani. The good parts of this thesis are as much theirs as they are mine. I also whole-heartedly acknowledge the efforts of my grandparents, without whose prayers and love I would not be here. I would especially like to remember my grandfather, Mohammad Subhan Dar, who could not live to see this day. His role in my upbringing and education can never be overstated. I was lucky to have him as my grandfather, and hope that I turn out to be as good a man as he was.

Thank you everyone. *May the tides always be in your favour!*

Biography

Faisal Wani was born in Srinagar, Jammu and Kashmir, on August 30, 1990. He graduated with master's degree in Electrical engineering (2016) from Delft University of Technology, Netherlands, and a master's degree in Wind Technology from Norwegian University of Science and Technology (NTNU), Norway. He obtained his bachelor's degree in Electrical and Electronics engineering from National Institute of Technology, Trichy, India in 2012. Since January 2021, he has been working as an Engineering Physicist at Huygens Engineers B.V.

In October 2016, Faisal started as a PhD candidate at Delft University of Technology. His research areas included tidal and wind energy conversion systems, among other applications of electrical machines, with emphasis on electrical machine modeling and reliability of electrical drives. Prior to this, he worked as an Engineer at Power Grid Corporation of India Limited (2012-2014), where he was responsible for remote monitoring and control of substation equipment of various substations from a centralized control center.